Spring 5-15-2022

Particle Formation and Thermal Radiation in Laminar Diffusion Flames with Applications to Energy and Materials

Phillip Irace
Washington University in St. Louis

WASHINGTON UNIVERSITY IN ST. LOUIS

McKelvey School of Engineering
Department of Mechanical Engineering and Materials Science

Dissertation Examination Committee:
Richard L. Axelbaum, Chair
Ramesh Agarwal
Rajan Chakrabarty
Katharine Flores
Patricia Weisensee

Particle Formation and Thermal Radiation in Laminar Diffusion Flames with Applications to Energy and Materials

by

Phillip Harold Irace

A dissertation presented to
The Graduate School
of Washington University in
partial fulfillment of the
requirements for the degree
of Doctor of Philosophy

May 2022
St. Louis, Missouri

Table of Contents

List of Figures

List of Tables

Acknowledgments

I would like to express my gratitude to:

First and foremost, my advisor and mentor, Dr. Richard Axelbaum. Without his guidance, I would not be the researcher, or person, that I am today. I will always value and remember the conversations we have had about research, energy, and life. I hope to continue our work together.

My wife, Sarah, who is the love of my life and my greatest supporter. Without her, I could not have accomplished any of this work. I look forward to sharing the rest of our lives together.

My parents, Joseph Jr., and Cristina Irace, for their unconditional love and support. From my father, I have learned perseverance and work-ethic. From my mother, I have learned patience and compassion.

Dr. Peter Sunderland for his mentorship and support during our microgravity research, and his students Kendyl Waddell, Minhyeng Kim, and Han Ju Lee.

The National Science Foundation for their support via the NSF Graduate Research Fellowship, which made this work possible.

NASA, particularly Dennis Stocker, and the ZIN Technologies Engineering team for their funding, support, and efforts during our Flame Design experiments aboard the ISS.

My colleagues, friends, and mentors in the Laboratory for Advanced Combustion and Energy Research: Jose Madero, Dishant Khatri, George Pires, Tianxiang Li, Zhiwei Yang, Piyush Verma, Ben Kumfer, Akshay Gopan, Jacob Mack, Caleb Martonfi, and Logan Tan.

Finally, all my past mentors and role models, for without whom, I would not be the man I am today: Harold Brandon, Dan Murphy, Adam Sherinski, Bill Lyons, Brian Fox, and Jim Crane.

Phillip Harold Irace

Washington University in St. Louis

May 2022

Dedicated to my wife, Sarah Elizabeth Pryor Irace, and my parents.

ABSTRACT OF THE DISSERTATION

Particle Formation and Thermal Radiation in Laminar Diffusion Flames with Applications to Energy and Materials

by

Phillip Harold Irace

Doctor of Philosophy in Mechanical Engineering

Washington University in St. Louis, 2022

Professor Richard L. Axelbaum, Chair

Fossil fuels supply over 80% of the world's primary energy, and if current policy and technology trends continue, global energy and energy-related carbon dioxide (CO_2) emissions are predicted to increase for at least several decades owing to population and economic growth, leading to serious concerns regarding global warming. Natural gas releases less CO_2 than other fossil fuels (e.g., coal and oil) and can help meet future CO_2 emission targets. Natural gas combustion, however, has poor radiation heat transfer when compared to other fossil fuels owing to its low propensity for soot formation, making it difficult to use as a drop-in replacement in applications requiring rapid heat transfer.

Methane is the primary constituent of natural gas, and in the first part of this dissertation, a method of increasing and controlling soot formation, and subsequently thermal radiation, from methane flames is presented. Oxygen-enriched combustion in a unique tri-coflow flame configuration, coupled with fuel additives, is used to increase soot formation and radiation heat transfer in laminar methane coflow diffusion flames, while ultimately oxidizing the soot particles to ensure complete combustion and no soot emissions. Thermal radiation from the methane flame is increased by 110%, to levels comparable to, or greater than, fuels with a much higher propensity for soot

formation, such as ethylene. In addition to increasing radiation heat transfer, the oxygen-enriched combustion approach employed has the additional benefit of facilitating carbon capture and storage (CCS), an established emissions reduction technology.

In order to efficiently use oxygen-enriched combustion to facilitate CCS, a more thorough fundamental understanding of how oxygen-enrichment affects flame structure, soot formation, and flame extinction is necessary. To this end, in the second part of this dissertation, burner-supported gaseous ethylene microgravity spherical diffusion flames are investigated aboard the International Space Station. Microgravity affords a unique environment where the effects of buoyancy are eliminated, and thus fundamental information about flame structure and its effect on soot formation, flame extinction, and flame stability can be probed. It is found that radiative extinction of these flames at atmospheric pressure occurs at a critical temperature and reactant-based mass flux, regardless of initial conditions. Flame stability in the presence of radiation heat loss is studied, and the limiting conditions for steady-state spherical diffusion flames are identified. Furthermore, the effects of ultra-low strain on the kinetic structure and oxidation pathway of ethylene diffusion flames are elucidated. The results presented have important implications for spacecraft fire safety and terrestrial wildfires.

In the last part of this dissertation, the subject of particle formation in flames was transitioned to identifying a method of producing materials in flames in a way that could lead to a novel approach to additive manufacturing. Specifically, the synthesis and deposition of high-temperature materials without contamination of the synthesis reaction byproduct was investigated. Material properties at high temperature are a common limiting factor for system performance and efficiency in energy technologies, such as plasma-facing materials, engine components and turbine blades. Flame synthesis with gas-phase precursors provides a unique opportunity to synthesize high-temperature

materials (e.g., refractory metals, refractory multi-principal element alloys, and ultra-high temperature ceramics) with no limit on the melting point of the material. In this part of this dissertation, a novel method of manufacturing components through flame synthesis is presented, and preliminary measurements are conducted. A thin layer of titanium is synthesized and deposited on a substrate with minimal contamination of the byproduct of the synthesis reaction This method holds promise for yielding improved high-temperature materials that could lead to significant advancements in additive manufacturing and the potential technologies that could benefit from it.

Chapter 1: Introduction

1.1 An introduction to combustion

From the simple candle flame for light and warmth, to the industrial revolution that led to unprecedented economic and population growth, combustion has been a driving force for the development of our civilization. One of the most important aspects of combustion is particle formation. For example, in hydrocarbon flames, thermal radiation from soot particles is typically considered the dominate mechanism for radiation heat transfer [1]. In fact, the yellow luminescence emitted from a candle flame is thermal radiation emitted from soot particles in the visible region of the wavelength spectrum. Without the formation of these soot particles, the flame would be dim blue and emit considerably less light and radiation. Moreover, using combustion for materials synthesis has led to the bulk production of carbon nanotubes [2-4], lithium-ion battery cathode materials [5], carbon black [6], titania [7], and many nano-powders [8] that have propelled economic and technological growth.

For centuries, combustion has provided us with reliable and dispatchable (i.e., on-demand) energy, transportation, and a plethora of bulk-synthesized materials. However, owing to rising concerns of global warming and the growth of renewable energy sources, combustion of fossil fuels is often perceived negatively by the public. Instead of attempting to do away with our most reliable, dispatchable, and secure energy source, this work advances the scientific understanding of fundamental combustion phenomena that facilitate methods of clean combustion and the combustion synthesis of materials that can lead to improved thermal efficiency in clean energy applications.

1.2 A brief overview of world energy

In an effort to curb global warming, many countries have adopted targets to cut, or achieve net-zero, carbon dioxide (CO_2) emissions by 2050 [9-26]. However, some question the feasibility of these emissions targets [27-34] because they are not trivial and will require significant technology advancements that presently do not exist, and policy changes that will be difficult, if not impossible, to achieve. For example, the 2021 International Energy Outlook [35] found that if current technology and policy trends continue, global energy consumption and energy-related CO_2 emissions will increase through 2050. Figure 1.1 shows that world energy consumption is predicted to increase by nearly 50%, largely to due economic and population growth in developing countries. The future policies in place and the technologies available will determine whether this large increase in energy demand comes to fruition, and if it does, whether an increase in CO_2 emissions will follow.

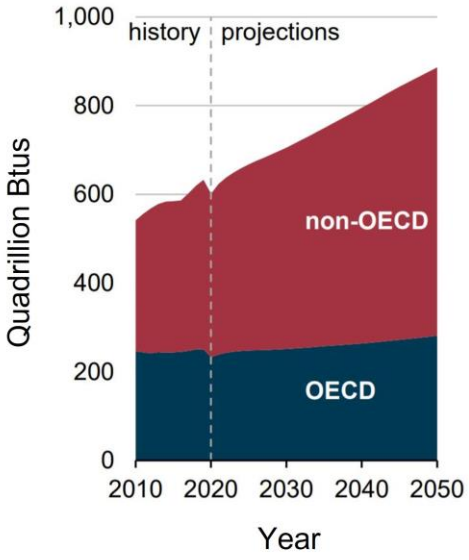

Figure 1.1. World energy consumption by year for Organization for Economic Co-operation and Development (OECD) and non-OECD countries [35].

Figure 1.2 shows a summary of the critical energy sources for electricity generation and their role in the current and predicted future world energy portfolio. Fossil fuels, which produce CO_2, currently account for about 60% of all electricity generation. Renewables account for only about 30% of electricity generation, with 60% of renewable electricity being from hydropower. However, in the future portfolio, intermittent renewable energy sources (solar and wind) are predicted to be the primary source for new electricity generation, while coal, natural gas, and nuclear will still be essential to meet load demand and support grid reliability. The challenges of a grid that relies on intermittent energy are just beginning to be realized, so this rapid growth of wind and solar may be fraught with challenges that could retard this growth. For example, the events in Europe this year (2022) have demonstrated how European reliance on wind, solar, and imported natural gas has exacerbated challenges of geopolitical stability. The sections below give a brief overview of the various energy sources and how they interplay with regards to the electric grid.

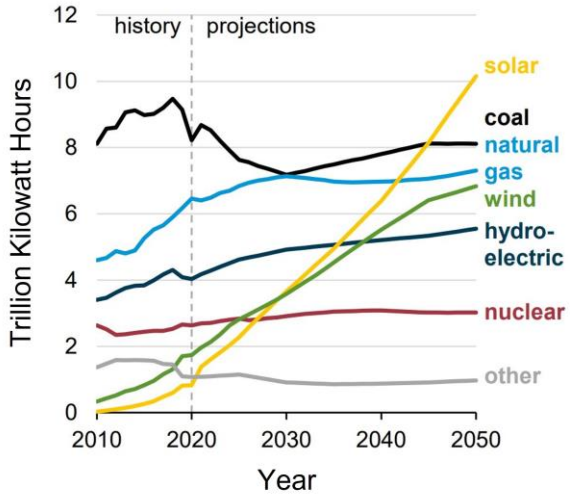

Figure 1.2. World net electricity generation by source as a function of year [35].

1.2.1 Renewable energy sources & the role of fossil fuels

Renewable energy sources (e.g., solar, wind, and hydropower) have received very positive public perception owing to concerns of global warming. They currently account for approximately 15%

of the world's energy consumption and are predicted to make up over 26% of the world's energy consumption by 2050, being the primary source for new energy generation (i.e., increased demand) [35]. In fact, some countries such as Iceland, Costa Rica, Norway, and Paraguay have already achieved greater than 95% renewable energy [36-37].

The question is: How are these countries able to achieve greater than 95% renewable energy when countries like the United States and India only achieve approximately 15% and 18% renewable energy, respectively?

Each of the countries listed above with a high percentage of renewable energy have relatively low energy demand when compared to the U.S. and India, and moreover, get over 75% of their renewable energy from hydropower, owing to their advantageous mountainous terrain and rather large annual rainfall. Unfortunately, much of the United States (e.g., Kansas and Arizona) and India do not have the mountainous terrain or rainfall to enable a significant amount of reliable hydropower. On the other hand, Kansas does have a lot of wind and Arizona has a lot of sun, so don't wind and solar make up for the lack of hydropower? And can't other renewable energy sources that are geographically advantageous make up for the lack of hydropower?

Hydropower is a relatively dispatchable energy source, meaning that provided there is enough rainfall, it can be dispatched and generate energy on demand. The fundamental difficulty with wind and solar energy, on the other hand, is that they are non-dispatchable energy sources, meaning that they cannot provide energy on demand. They are intermittent and only provide energy when the wind is blowing, or the sun is shining, which is not consistent from day to day, season to season or year to year. This makes it much more difficult to maintain grid stability, because there must be

a backup to accommodate the electricity demand when the sun is not shining, and the wind is not blowing.

Denmark is an excellent example. Denmark boasts 42% wind energy, which is the highest wind percentage of any country in the world [19-20]. A close look at their energy portfolio shows that they are able to accomplish this using a thermal baseload of coal (~10%), natural gas (~6%), and biomass (~20%), and then they import and export with their neighbors [19-20]. When they have excess wind, they export it to their neighbors. When the wind is not blowing, they import energy from their neighbors, such as Germany. This works for Denmark because they have small energy demand, consuming only about 30,000 GWh of electricity per year, which is less than 6% of Germany's total yearly consumption. For Germany to provide or absorb excess energy for Denmark is a small perturbation to their grid. Unfortunately for Germany, this tactic of importing and exporting energy to maintain grid stability with a high concentration of intermittent renewable energy sources will not work, because Germany is comparable to, or larger than, all its neighbors, regarding energy consumption. Thus, Germany must accommodate its intermittent renewable energy sources by ramping its thermal baseload (i.e., fossil fuels) up and down, depending on the supply from the intermittent renewables. This method is obviously not scalable or economical, because eventually with higher percentages of wind and solar you will have to shut down fossil fuel plants, as they will be used too infrequently to keep them operating, but that is when you will need to rely on them most. Keeping a large power plant on reserve when it is used infrequently is not economically practical, nor would it be reliable. Not to mention, starting the plant back up cannot be done as quickly as would be needed to take over for decreasing renewables.

In order to achieve 100% renewable energy, there has to be enough dispatchable renewable energy (i.e., hydropower, geothermal, or biomass) to accommodate for times when there is no solar or

wind, and there is no evidence that this is possible on a large scale. Otherwise, there must be enough batteries to store enough energy to last until solar and wind return. The problem with batteries is that they only work if they are charged, and when there are rare weather events, and the batteries have already been drained, they are no longer a source of backup. For example, consider an extreme weather event that occurs once in a century. Is it economically practical to install the batteries (and the excess wind and solar capacity that would be needed to charge the batteries) when they would only be used once a century, if at all? Or is it more practical to develop clean combustion technologies, and rely on a diversified electric grid with the reliable fossil fuels that got the world to where it is today?

1.2.2 An example: The Texas 2021 blackouts

A recent example of the non-scalability of ramping fossil fuel plants to accommodate variable renewable energy sources is the 2021 Texas blackouts. The rest of this section is an excerpt from an article co-authored by Irace and Axelbaum [38].

In mid-February 2021, Texans were plunged into a period of freezing cold and snow, causing an unprecedented demand for electricity [38]. Figure 1.3 shows electricity demand and consumption by source for Texas in February 2021. In the late hours of Valentine's Day, as temperatures plummeted to their lowest, the dispatchable energy sources (coal, natural gas, and nuclear) were operating near maximum capacity. This is a very dangerous condition, like running your car with the pedal smashed to the floor. Eventually, something will give out. And soon, it did. A number of plants went offline, which is not an unusual occurrence for a grid the size of Texas's. However, with no reserve power to make up for the outages, the entire grid became unstable, forcing many more plants to shut down as well. Technically, what happen was the reduction in energy supply,

without any reserve power to make up for it, caused the frequency in the grid to plummet. A rapid drop in frequency is catastrophic for the grid. Texas was only minutes away from a catastrophic failure that could have left millions more in the dark for days, or even weeks. To prevent that, ERCOT, the Texas grid operator, was forced to introduce a series of rolling blackouts.

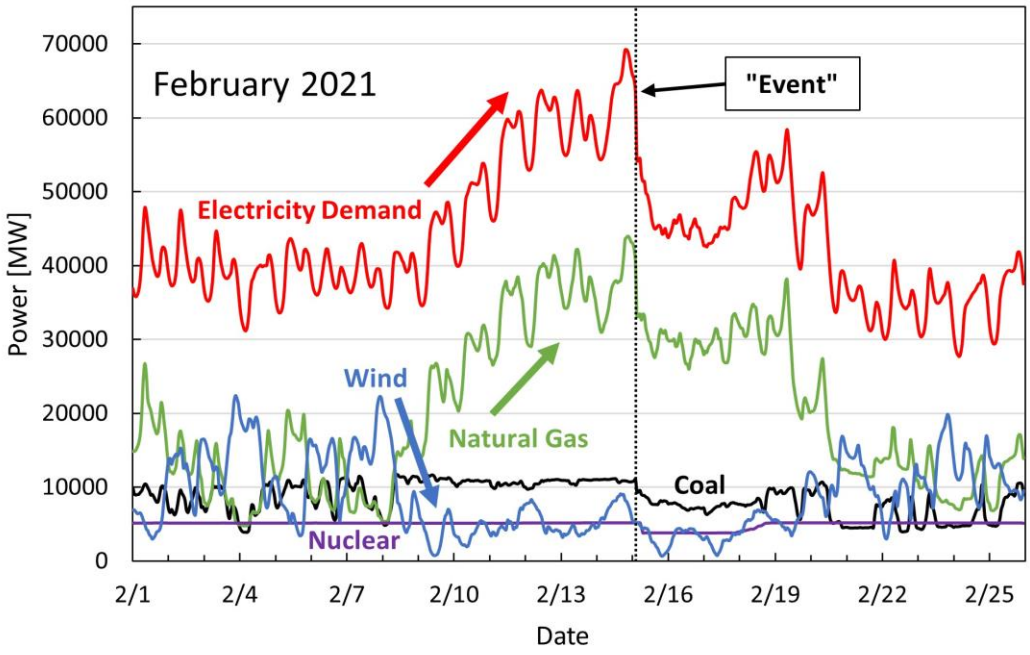

Figure 1.3. Electricity demand and consumption by source for Texas in February 2021 [38].

During a typical winter, Texas has no difficulty meeting electricity demand. February 2021, however, was different. The cold snap was an atypically extreme weather phenomenon, a black swan event, which caused the electricity demand to skyrocket. However, this isn't the first time Texas has experienced such low temperatures. The temperatures were lower in 1989 and 1983. Not to mention, there were 20 nights of below freezing temperatures in Houston in 1978. This year's temperatures were certainly within the expectations of ERCOT. Moreover, in the last three years, Texas has increased its total electric capacity. So why the sudden shortage? Wasn't the real problem wind (if you are conservative), fossil fuels (if you are liberal) or the weather (if you are ERCOT)?

But the problem wasn't wind, per se, nor was it fossil fuels, nor the extreme weather. The problem was ERCOT and its inability to acknowledge, and plan for, the limitations and intermittency of wind and solar amidst extreme weather events. ERCOT certainly had plenty of warning in past years that wind dies down in times of cold weather. Nonetheless, ERCOT continued to build wind energy capacity, but more importantly, in the process, they prematurely decommissioned coal plants that were not past their usable life [38,39]. Figure 1.4 shows that they decommissioned over 5 GW of coal plants from 2017 to 2020, which would have been more than enough energy to get them through this extreme weather event. Instead, they relied on their newly installed wind energy. Unfortunately, the wind was not blowing when they needed it most.

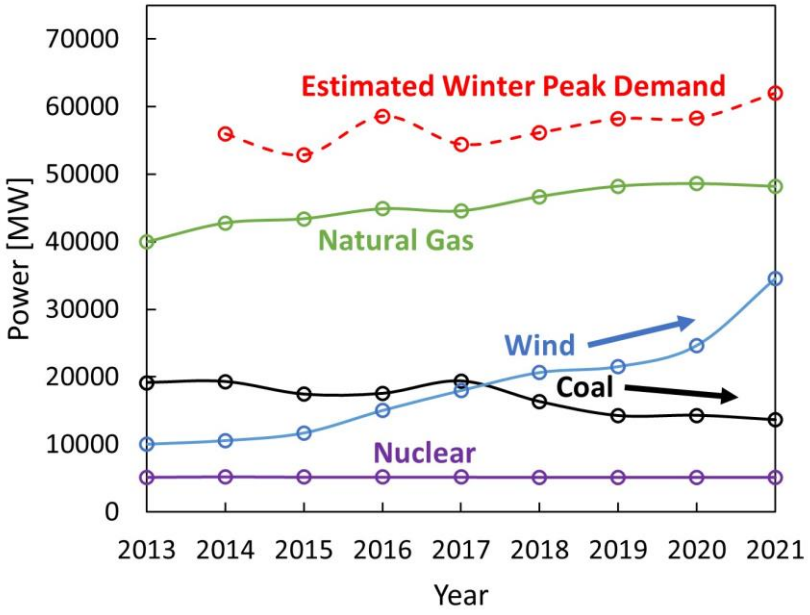

Figure 1.4. Energy capacity by source and peak Winter demand for Texas as a function of year [38].

The greater issue that this catastrophe revealed, however, is this: the utility industry has long known that to have a stable, secure grid at all times requires a diverse mix of reliable energy sources. In the past this meant a healthy mix of coal, gas, nuclear and hydro. Now, as the industry works to reduce its carbon footprint, wind and solar have become part of the mix, and the

challenges of replacing reliable energy sources with intermittent energy sources are becoming apparent. The coal plants that ERCOT decommissioned were built for a reason. They needed them for a secure gird with a sufficient amount of reserve power. But ERCOT replaced them with intermittent wind turbines. When they made the decision to decommission those plants and replace them with wind, they took a significant risk, and that risk did not pay off.

Here is the takeaway: many experts in the utility industry are painfully aware that if we are going to add wind and solar responsibly, we need to invest an enormous amount of money into backup power or batteries because we have to have enough energy in order to accommodate these extreme, once-in-a-lifetime weather events. However, these same experts seem unwilling to speak out for fear of being criticized; they would have to tell their shareholders that it is very expensive to have reliable power from wind and solar, because there must be enough batteries or dispatchable energy sources (i.e., fossil fuels or nuclear, because there is no more available hydropower in Texas) that will often be on standby, or run at low capacity, to accommodate extreme weather events.

1.3 Fossil fuels and geopolitical stability

Because, for the reasons outlined above, fossil fuels still account for about 80% of world energy, they are very important when considering a country's energy security. Thus, their cost, availability, and international trading has many geopolitical ramifications. The current conflict between Russia and Ukraine is the perfect example.

Natural gas is a large part of the Russia-Ukraine conflict. Natural gas is shipped as liquified natural gas (LNG) or traded internationally via pipeline. Russian natural gas exports account for 26% of all international pipeline trade and 8% of all LNG trade. European countries account for about 77% of these natural gas exports and Russian natural gas is about 40% of Europe's total natural

gas consumption. Furthermore, nine countries in East Europe (Bulgaria, Cech Republic, Estonia, Finland, Hungary, Latvia, Romania, Slovakia, and Slovenia) rely on Russia for more than 90% of their natural gas imports [40]. Due to these concerns and market panic, natural gas prices have jumped over 20% to the highest levels since 2014 [41]. If Russia were to restrict its natural gas in response to sanctions imposed by Western countries, it would have global ramifications. The implication of this is that much of Europe is unable to do anything that would cause Russia to turn off their supply. In other words, Europe is beholding to Russia because they have transitioned to an energy mix that is dependent on Russia. Energy is the life blood of any modern economy, and much of Europe is now dependent on Russia for its very existence.

Clearly there is an urgent need for sources of energy from a broader range of fuels, but these sources of energy must have low emissions. One such technology that can deliver reliable, low carbon energy from fossil fuels is carbon capture and storage (CCS), and one of the most promising methods to facilitate CCS is oxygen-enriched combustion.

1.4 Oxygen-enriched combustion

Rising CO_2 emissions has led to the development of a number of new combustion technologies for carbon capture and storage [42-46]. Oxygen-enriched combustion is at the center of most of these technologies.

For carbon capture and storage, nitrogen must be absent from the system before the CO_2 can be sequestered. For existing fuel/air systems, this must be done via the removal of nitrogen from the flue gases. In oxy-combustion applications, the nitrogen is removed from the air before combustion to obtain a gas stream ready for sequestration. In other words, in lieu of air, the fuel is combusted in pure oxygen and recycled flue gas, to control temperature. Additional advantages of oxygen-

enriched combustion include reduced NO_x and SO_x emissions and improved thermal efficiency [47-48].

Another promising oxy-combustion application to facilitate carbon capture and storage is the Allam Cycle, which employs supercritical CO_2 (sCO_2) in a high efficiency process that yields full carbon capture [49].

Owing to the high cost of cryogenic air separation, oxygen-enriched combustion technologies must introduce oxygen into the system in the most efficient way possible. In order to efficiently use oxygen-enriched combustion to facilitate CCS, a comprehensive fundamental understanding of how altering flame structure using oxygen-enrichment affects thermal radiation, soot formation, flame extinction, and flame stability is necessary. Flame extinction and flame stability limits are of fundamental importance because loss of power can be catastrophic to the grid and lead to increased pollutant emissions that negatively impact human health.

1.5 Flame extinction and stability

Most flame extinction can be attribute to kinetic extinction, where the flow time relative to the chemical reaction time is high (i.e., a high Damköhler number). This type of flame extinction has been studied extensively in diffusion flames owing to its many practical applications.

Radiative extinction, where the flow time relative to the chemical reaction time is low (i.e., a low Damköhler number), and the flame extinguishes due to excessive radiation heat loss, on the other hand, is not well-studied. Radiative extinction is impractical to replicate on a laboratory scale, owing to buoyancy enhanced mixing, which accelerates the flow field, decreasing the residence time and straining the flame. To avoid buoyancy and facilitate the long residence times that can

lead to radiative extinction, radiative extinction is studied in microgravity, which also provides unique insights for spacecraft fire safety. Radiative extinction also has applications for wildfires, which emit large amounts of CO_2 and particulate matter.

Past microgravity experiments (i.e., drop towers) have been limited to 2-5 s of experimental duration. During these short times, the flame either continues to grow, or extinguishes. No experimental evidence has been shown to prove or disprove the existence of a steady-state spherical diffusion flame. Thus, the existence of a stable, steady-state spherical diffusion flame is a question of fundamental importance for spacecraft fire safety.

Until recently, long duration microgravity was not attainable to answer these fundamental questions. The existence of the ISS (discussed in Chapters 4-7) has changed that.

1.6 High temperature material

The topic of particle formation in flames and gas-phase combustion can be easily transitioned to materials synthesis. Flame synthesis with gaseous precursors allows for the unique opportunity to synthesize high temperature materials (e.g., refractory metals, refractory multi-principal element alloys, and ultra-high temperature ceramics) with no limit on the melting point of the material.

Material properties at high temperature are often a limiting factor for system efficiency in energy and other applications alike. Plasma-facing materials in fusion reactors [50] and high temperature engine components [51] are excellent examples of energy applications that require high temperature components. Other applications where system performance could be limited by material properties at high temperature include solar probes, wing-leading edge systems, Nuclear Thermal Propulsion, turbine components, and rocket nozzles. In addition to the properties of these

high-temperature materials limiting system performance, these same properties can make them difficult to manufacture, particularly when considering complex geometries, using current state of the art manufacturing methods.

Chapter 8 introduces a novel method of additive manufacturing (AM) enabled by flame synthesis that has the potential overcome the fundamental challenges associated with current state-of-the-art (SOA) AM methods and to fabricate components of existing materials with improved high-temperature properties, entirely new materials with improved high-temperature properties, and functionally graded materials (FGMs) with locally tailored properties.

1.7 Research objectives and outline

This research is motivated to advance the scientific understanding of fundamental combustion phenomena related to particle formation and thermal radiation in laminar diffusion flames that can lead to improved methods for reducing pollutant emissions, facilitating carbon capture and storage, and increasing thermal efficiency through improved radiant heat transfer, or the combustion synthesis and deposition of improved ultra-high temperature materials. To that goal, it focuses on three fundamental and unique research projects:

1) The use of natural gas in oxygen-enriched combustion applications will be critical for reducing future CO_2 emissions. Unfortunately, natural gas combustion has poor radiation heat transfer characteristics relative to other fossil fuels (i.e., coal and oil), making it difficult to use as a drop-in replacement. A fundamental understanding of the radiative characteristics of methane (i.e., the primary constituent of natural gas) flames is critical for the effective use of natural gas. Chapter 2 involves a systematic investigation of the effects of central oxygen enrichment on thermal radiation in laminar methane and ethylene tri-coflow diffusion flames, with the goal of increasing (i.e.,

controlling), and elucidating a fundamental understanding of, thermal radiation in natural gas combustion processes through higher local temperatures and soot concentrations. In Chapter 3, toluene (C_7H_8) is added to the tri-coflow methane flames of Chapter 2 in an effort to further understand and increase the radiative performance of methane.

2) Microgravity spherical diffusion flames allow for a unique opportunity to unambiguously demonstrate the effects of flow direction on soot formation while altering flame structure, and to study radiative extinction and flame stability for applications for the optimization of oxygen-enriched combustion to facilitate carbon capture and storage. This experiment is called Flame Design and is part of the NASA project Advanced Combustion via Microgravity Experiments (ACME). Chapter 4 gives some historical context and motivation for the experiment, and then shows the first experimental observations of long duration microgravity spherical diffusion flames. Experiments are compared to a transient numerical model. Chapter 5 elucidates a critical point (temperature and mass flux) at which microgravity spherical diffusion flames at 1 bar radiatively extinguish. Chapter 6 answers the fundamental question as to whether a steady state microgravity spherical diffusion flame exists in the presence of radiation heat loss. Chapter 7 elucidates the effect of ultra-low strain on the structure and oxidation path of ethylene diffusion flames.

3) Metals with improved high temperature properties are often highly desired to increase system performance and efficiency. Additive manufacturing (AM) provides a method to rapidly produce near-net shaped complex parts of these high temperature metals. However, current state-of-the-art metal AM methods require a pre-made feedstock material (i.e., a powder or wire) and use a laser to create a melt pool and fuse new material to the part. For high temperature materials (e.g., refractory metals) the thermal gradients at the melt pool result in residual stresses and microcracking. Furthermore, in order to create an alloy, a feedstock powder of that alloy must be

available, or powders of different metals must be introduced *in-situ*, which results in incomplete mixing, owing to the vastly different materials of the constituent elements, and a non-homogenous microstructure. In Chapter 8, a new AM method, Flame-Assisted Additive Manufacturing (FLAMe) in which the desired material is synthesized *in-situ* prior to deposition, and overcomes many of these fundamental difficulties, is introduced and shows proof-of-concept data for materials synthesis and deposition with minimal contamination of the synthesis reaction byproduct. FLAMe also provides a unique opportunity for rapid materials characterization that can accelerate the investigation of the widely unexplored regions of multicomponent alloy phase space.

1.8 Statement of authorship

Chapters 2 and 3 are manuscripts submitted for publication and authored by me, Phillip H. Irace, with Dr. Richard L. Axelbaum as a co-author and Dr. Akshay Gopan as a third author on Chapter 2 [52,53]. Chapter 4 sections 4.2 – 4.6 is a published work authored by me, Phillip H. Irace, and co-authored by Dr. Richard L. Axelbaum, NASA project scientist Dennis Stocker, Dr. Peter B. Sunderland, Kendyl Waddell, Logan Tan, and Han Ju Lee [54]. Chapter 5 is a manuscript submitted for publication and authored by me, Phillip H. Irace, with Kendyl Waddell, Dr. Denis Constales, Dr. Peter B. Sunderland, and Dr. Richard L. Axelbaum as co-authors [55]. Chapter 6 is a manuscript submitted for publication and authored by me, Phillip H. Irace, with Kendyl Waddell, Dr. Denis Constales, Minhyeng Kim, Dr. Gregory Yablonsky, Dr. Peter B. Sunderland, and Dr. Richard L. Axelbaum as co-authors [56]. The numerical model used in Chapters 3-6 is operated by Dr. Peter B. Sunderland, Kendyl Waddell, and Han Ju Lee at the University of Maryland, College Park.

Chapter 2: An investigation of thermal radiation from laminar diffusion flames in a tri-coflow burner with central oxygen

2.1 Introduction

If current policy and technology trends continue, global energy and energy-related CO_2 emissions are predicted to increase for at least several decades owing to population and economic growth [36]. While an increase in renewable energy sources will play a major role for new electricity demand, fossil fuels are still essential to help meet energy demand, to support grid reliability, and for industrial processes [36]. Furthermore, fossil fuel production is predicted to continue growing, primarily to support increasing energy consumption in developing countries. As the use of fossil fuels continues to grow, so will CO_2 emissions. Because natural gas is less polluting than other fossil fuels (e.g., coal and oil) and can help meet future CO_2 emission targets, it is estimated to account for much of the future growth in fossil fuel use [36]. Moreover, fracking has revolutionized the power industry by supplying abundant natural gas. Natural gas combustion, however, has poor radiation heat transfer when compared to other fossil fuels [57]. Because of this, the radiative properties of natural gas combustion have become a matter of increasing interest. In order to effectively replace sootier fossil fuels (e.g., coal and oil) with natural gas, a fundamental understanding of the combustion and radiative characteristics of natural gas flames is needed.

Natural gas is composed of more than 87% methane (CH_4), and methane is intrinsically less sooty than other hydrocarbon fuels, largely due to its lack of a carbon-carbon (C-C) bond and low carbon-to-hydrogen ratio. In aliphatic hydrocarbons, fuel pyrolysis results in the formation of acetylene (C_2H_2), which leads to the formation of polycyclic aromatic hydrocarbons (PAHs), both of which play an important role in soot formation [58]. During methane combustion, methyl radicals (CH_3) must first react with either another methyl radical, or methylene (CH_2), in order to form the C_2 species that can lead to the formation of acetylene, and eventually soot [58]. The energy barrier of these methyl radical reactions significantly inhibits soot formation in methane

flames. Soot, however, is a strong emitter of thermal radiation in the visible and infrared regions, making it essential to ensure significant radiation heat transfer in many combustion processes [1]. The low concentration of soot formed during methane combustion is what leads to poor radiation heat transfer from natural gas flames. Improving our ability to control the combustion and radiative characteristics of methane is critical to optimizing the use of natural gas as a replacement for more polluting fossil fuels.

One promising method for increasing thermal radiation in natural gas combustion is oxygen-enriched combustion, a common technique for improving heat transfer and thermal efficiency in industrial applications, such as steel making and glass melting [59.60]. The increased thermal radiation associated with oxygen-enriched combustion typically results from higher flame temperatures, more soot, and a higher product gas emissivity [61,62]. Oxygen-enriched combustion is also advantageous for increased efficiency, improved flame stability, and facilitating carbon capture and storage [44,59].

Because the adiabatic flame temperature of methane combustion with oxygen is 3050 K, as compared to only 2230 K with air, the use of oxygen-enriched combustion is often justified by the argument that radiation goes like temperature to the fourth power [63-65]. However, understanding radiation in flames is complicated by the fact that temperature also has a significant effect on product gas emissivity. Furthermore, oxygen enrichment affects the product gas composition, residence time, and soot burnout, so it is very difficult to say apriori what effect oxygen enrichment will have on thermal radiation from a flame.

Considering the relatively low concentration of soot in methane flames, it is instructive to first isolate the fundamental effects of oxygen-enhanced combustion on the emissive power of the product gases. The emissive properties of combustion product gases (primarily CO_2 and H_2O) are

historically well-studied, and it is well-known that gas emissivity has a strong dependence on temperature, pressure, and path length [66-70]. The classic Hottel charts show that the emissivities of CO_2 and H_2O increase with path length and pressure but decrease significantly with temperature at combustion temperatures (i.e., greater than 1200 K) [71].

Figure 2.1 shows radiation heat flux as a function of temperature for a parcel of product gas from both methane/air combustion ($CO_2/H_2O/N_2$) and methane/oxygen combustion (CO_2/H_2O), assuming complete combustion. Gas emissivity is calculated using the Edwards exponential wide-band model [72-74], and the path length is held constant. The higher radiant emission from the methane/oxygen flame at a given temperature is due to the removal of nitrogen, and the subsequent higher partial pressure of CO_2 and H_2O, which increases the product gas emissivity. Figure 2.1 shows that, while also dependent upon path length, the temperature dependence of the emissive power from product gases is actually much less than temperature to the fourth power, owing to the significant temperature dependence of the emissivities of the product gases. Moreover, from Fig. 2.1, when comparing gas radiation at a flame temperature of 2200 K for methane/air combustion to 3000 K for methane/oxygen combustion (an 800 K temperature difference), approximately 60% of the increase in radiation from the product gases from the methane/oxygen flame is due to the removal of nitrogen and increased partial pressure of CO_2 and H_2O (i.e., the higher emissivity), and only 40% of the increase is due to the increased temperature. This rather modest effect of temperature is due to the fact that the temperature dependence of gas emissivity reduces the expected increase in radiation with temperature.

Radiation from soot is also strongly dependent upon emissivity (i.e., soot volume fraction), and not just temperature. Therefore, when considering radiation in flames, particularly methane flames,

which have low soot concentrations, the effect of emissivity can be comparable to or greater than that of temperature on its own.

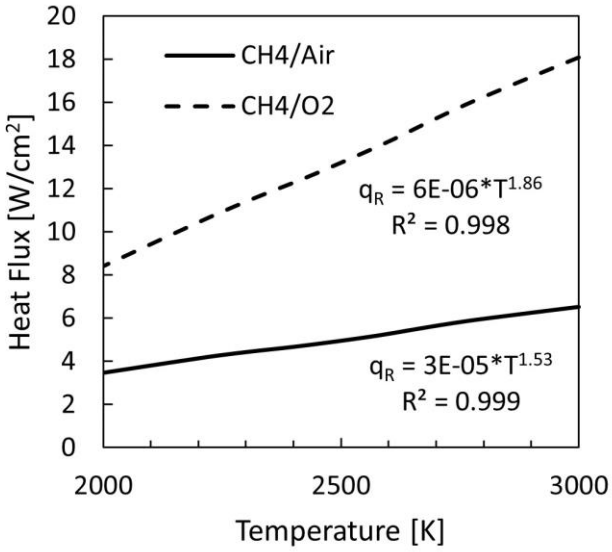

Fig. 2.1. Radiative heat flux calculated using the Edwards exponential wide-band model [72-74] as a function of temperature for product gas mixtures assuming complete combustion for methane/air ($CO_2/H_2O/N_2$) and methane/oxygen (CO_2/H_2O) flames.

In most oxygen-enriched combustion applications, oxygen is added to the outer coflow of a normal diffusion flame [75]. However, this can lead to a significant reduction in flame height and an enhancement in soot oxidation rates [75]. As much of the increase in radiation with oxygen is due to the increase in emissivity from higher soot concentrations, adding oxygen to the outer coflow could have a detrimental effect on radiation from these flames. Furthermore, a large amount of oxygen is necessary to affect any significant change in the oxygen concentration in the outer coflow, making this an expensive proposition due to the high cost of cryogenic air separation [62]. Instead, in this study, a tri-coflow (i.e., triple-port) burner is employed. In this configuration, oxidizer is supplied to the central tube, fuel to the inner annulus, and oxidizer to the outer annulus. The concept of tri-coflow flames has been used for many practical applications such as oxygen lances [76], pressurized oxy-combustion to facilitate carbon capture and storage [46], and

tribrachial flame edges for applications to direct-injection spark ignition engines [77]. The goal of this effort is to evaluate whether the radiation intensity of methane can be significantly enhanced and controlled by introducing a modest amount of oxygen to the system, in this case by introducing it into the center of a normal coflow diffusion flame. Adding a modest amount of oxygen to the center of the flame, in lieu of the outer coflow, can lead to a second, high temperature reaction zone (i.e., in addition to the outer flame, an inner inverse diffusion flame exists, where oxidizer flows into fuel [78,79]). This yields a new inner zone that is at high temperature and conducive to soot inception and growth. By creating a large concentration of high temperature soot in the center of the flame without significantly reducing residence time (i.e., flame height), the radiation intensity of the flame could be significantly increased. This is in contrast to adding the oxygen to the outer coflow air, which requires considerable oxygen (high cost), but also yields a significant reduction in residence time owing to reduced flame height, and an enhancement in soot oxidation rates.

Soot, thermal radiation, and oxygen-enriched combustion have been studied in triple-port methane flames. Li et al. examined the effects of oxygen enrichment on flame shape and carbon monoxide production for various velocity ratios. They found that increasing the oxygen concentration in the central tube results in the presence of a second flame anchored on the central tube, a decrease in flame height, and enhanced soot oxidation [80]. Yamamoto et al. measured soot and PAHs in a triple port burner, where both of the oxidizers were air, and found that introducing air into the inner nozzle reduces soot and PAHs [81].

Radiation for laminar methane-air flames has also been investigated. Sivanthanu et al. examined the effect of gas-band radiation on soot kinetics in laminar coflow methane flames and found that gas radiation (CO_2 and H_2O) dominates soot radiation by an order of magnitude, and that radiation

heat loss or gain can significantly affect soot formation and oxidation rates [82]. Datta et al. performed a numerical study to understand the contributions of self-absorption and soot radiation in a laminar methane-air coflow diffusion flame. They found that the contribution of soot radiation in methane combustion is non-negligible, but less significant than the contribution of the gaseous products [83].

In contrast to methane, ethylene (C_2H_4) contains a C-C double bond, which provides a relatively rapid pathway to the formation of soot. It is also a commonly studied sooty fuel, making it a relevant base-case fuel for comparison with methane to study the relative importance of central oxygen enrichment [65,84].

This work involves a systematic investigation of the effects of central oxygen on thermal radiation in laminar methane and ethylene tri-coflow diffusion flames, with the goal of increasing (i.e., controlling), and elucidating a fundamental understanding of, thermal radiation in natural gas combustion processes through higher local temperatures and soot concentrations.

2.2 Methods

2.2.1 Experimental configuration

The triple port burner employed is shown schematically in Fig. 2.2. The burner consists of three concentric tubes, with tube dimensions (ID/OD) of 2.16/3.18, 11.07/12.7, and 121.5/126.5 mm for the central, middle, and outer tubes, respectively. Air is supplied through the outer tube, fuel through the middle tube, and oxygen through the central tube. The inner tube is at least twice the length necessary for fully developed laminar flow. A uniform flow field is maintained in the outer and middle tubes using honeycomb flow straighteners. The oxygen and fuel flow rates are

controlled with rotameters (Matheson Model FM-1050 Series), and the outer air flow rate is controlled using a sonic nozzle.

The fuel flow rate is held constant for both fuels (200 sccm for CH_4 and 120 sccm for C_2H_4) to

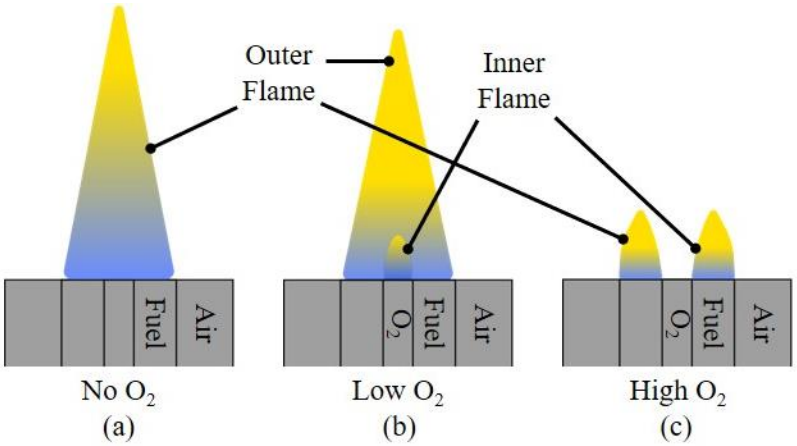

Fig. 2.2. Experimental configuration with a representative diagram of the three flame shapes observed herein. The outer flame is always over-ventilated. **(a)** No central O_2 flow. **(b)** Low central O_2 flow (under-ventilated inner flame). **(c)** High central O_2 flow (over-ventilated inner flame).

maintain a constant chemical heat release rate of 110 W, assuming complete combustion. The outer air flow rate is held constant at approximately 60 slpm to maintain an over-ventilated outer fuel/air flame. In this investigation, the central stoichiometric ratio (CSR) with respect to the fuel is varied from 0 to 0.5. The CSR is defined as,

$$CSR = (Q_{O2})_{central}/(\nu_{O2,Fuel}*Q_{Fuel}) \, , \tag{2.1}$$

where Q is the volumetric flow rate and ν_{O2} is the stoichiometric coefficient for oxygen of the fuel under consideration (e.g., 2 for methane and 3 for ethylene).

2.2.2 Radiation Loss Fraction

Total radiant emission is measured using a wide-angle radiometer. The radiometer detector is a xenon-encapsulated thin-film thermopile (Dexter 2M DX-0927) with a calcium fluoride (CaF_2) window. The detector has a flat spectral response from 0.1 to 100 μm and the CaF_2 window has a transmission bandwidth of 0.13 to 11 μm. The radiometer is calibrated using a LumaSense M335 Blackbody Calibration Source, and is positioned 14 cm from the flame, resulting in a field of view of approximately 100 mm. The solid angle of the radiometer is 0.34 sr. Radiation measurements are reproduceable within 4%.

The radiation loss fraction provides a useful way to quantify the total radiant power emitted from the flame as a function of the total rate of heat release (i.e., the amount of radiation emitted per mass of fuel input). The radiative loss fraction is calculated from,

$$X_R = Q_R/Q_C \,, \tag{2.2}$$

where Q_R is the total radiant loss and Q_C is the theoretical heat release assuming complete combustion [85,86]. Assuming spherically isotropic emission, the total radiation loss can be obtained from,

$$Q_R = 4\pi R^2 q_r \,, \tag{2.3}$$

where R is the distance from the radiometer detector to the flame centerline and q_r is the measured heat flux [85,86]. For complete combustion, Q_C is given by

$$Q_C = \dot{m}_{Fuel}\, LHV \,, \tag{2.4}$$

where $\dot{m}_F$ is the fuel mass flow rate and LHV is the lower heating value of the fuel, which is calculated using enthalpies of formation obtained from the NIST/JANAF database [87].

2.2.3 Two-color ratio pyrometry

Soot temperature measurements are taken using two-color ratio pyrometry with a Nikon D610 digital single-lens reflex (DSLR) camera. The D610 contains a full frame (36 mm x 24 mm) 24.3 MP FX format complementary metal-oxide-semiconductor (CMOS) sensor with a Bayer color filter array (CFA). Incandescence from the soot particles is imaged at the three wavelength bands of the camera's CFA: red, green, and blue (R, G, and B).

Planck's Law is employed to calculate the theoretical emitted intensity at any wavelength for a given temperature. Planck's law is given by,

$$I(\lambda,T) = \varepsilon(\lambda)2\pi hc^2/\lambda^5[\exp(hc/\lambda kT)-1] \,, \tag{2.5}$$

where I is the emitted radiance, λ is wavelength, T is temperature, ε is emissivity, h is Planck's constant, c is the speed of light, and k is the Boltzmann constant. The signal, S_i, detected by a pixel over a time interval τ is the intensity of spectral radiation integrated over the detection wavelengths,

$$S_i = (2\pi hc^2)\tau \int \varepsilon(\lambda)\eta(\lambda)/\lambda^5[\exp(hc/\lambda kT)-1]\, d\lambda \,, \tag{2.6}$$

where the term $\eta(\lambda)$ is the spectral efficiency of the detection system, which accounts for the spectral efficiencies of the detector, lens, and filter, as well as a geometric factor [88]. The subscript i denotes one of the three wavelength bands of the CFA (R, G, or B). The upper and lower bounds of the integral, λ_1 and λ_2, are the low and high limits of the detector bandwidths, which are approximately 400 and 700 nm (i.e., the visible region). Because the CFA detectors detect in a relatively broad range of wavelengths, the assumption of narrowband detection is not valid [88]. The effect of the variation in the Planck function over a broad region of wavelengths can be overcome using the signal ratio approach shown in Eq. 2.7,

$$S_i/S_j = \int \eta_{Fi}(\lambda)\varepsilon(\lambda)/\lambda^5[exp(hc/\lambda kT)-1]\, d\lambda \,/ \int \eta_{Fj}(\lambda)\varepsilon(\lambda)/\lambda^5[exp(hc/\lambda kT)-1]\, d\lambda \,, \quad (2.7)$$

where $\eta_F(\lambda)$ accounts for the respective transmission efficiency of each wavelength band as a function of wavelength [88].

Ratio pyrometry relies on the fact that Planck's Law predicts that the ratio of the intensities for any two wavelength bands is a unique function of temperature. By numerically evaluating the integrals in Eq. 2.7 over a range of temperatures, a temperature and signal ratio lookup table can be generated, as in [33].

If the grey body assumption is used, the emissivities in Eq. 2.7 cancel out. However, the emissivity of soot has a relatively strong spectral dependence and, thus, soot cannot be accurately approximated as grey. As seen in Eq. 2.8, the wavelength dependence of the spectral emissivity of soot, $\varepsilon_{S\lambda}$, is described by the dispersion exponent, α [89].

$$\varepsilon_{s\lambda} = 1/\lambda^{\alpha} \,, \quad (2.8)$$

The dispersion exponent is very important in color-ratio pyrometry. It has a wavelength dependence that has been shown to vary by location, from 2.2 for young soot (where the H/C ratio varies from 0.5 to 0.6), to 1.2 for mature soot (where the H/C ratio is about 0.2) in diffusion flames [89]. Ma et al. obtained a spatially resolved two-dimensional α map in nitrogen-diluted ethylene flames and found that α can vary from 0.9 to 2.2, and this variation in α can result in a difference of up to 50 K in calculated temperature [90]. For simplicity, most investigators assume a constant value for the dispersion exponent [84,88,91-94]. Additionally, it has been shown that the dispersion exponent is close to 1 in the near-infrared region, but in the visible region, it is closer

to a value of 1.38 [95,96]. In order to better match previous work, the emissivity of soot is assumed to vary with a constant dispersion exponent of 1.38 [88,91,92].

A Schott BG62 filter is used to provide better balance between the R, G, and B signals, because the red intensity is dominant at high temperature. To quantify the spectral efficiency $\eta_F(\lambda)$ for each color channel, the spectral response of the optical system (i.e., the D610 camera and the BG62 filter) is measured. The spectral response, shown in Fig. 2.3, is found by imaging a 2800 K tungsten lamp through a monochromator in 5 nm wavelength increments from 400 to 700 nm. The measured spectral intensity for R, G, and B is then normalized by the total power at each wavelength to obtain the spectral efficiency factor. The theoretical light intensity for each wavelength band is calculated for a grey body, and for soot, by integrating Eq. 2.6 from 400 to 700 nm for a temperature range of 1000 to 3000 K in 1 K increments. Using the theoretical intensities, a

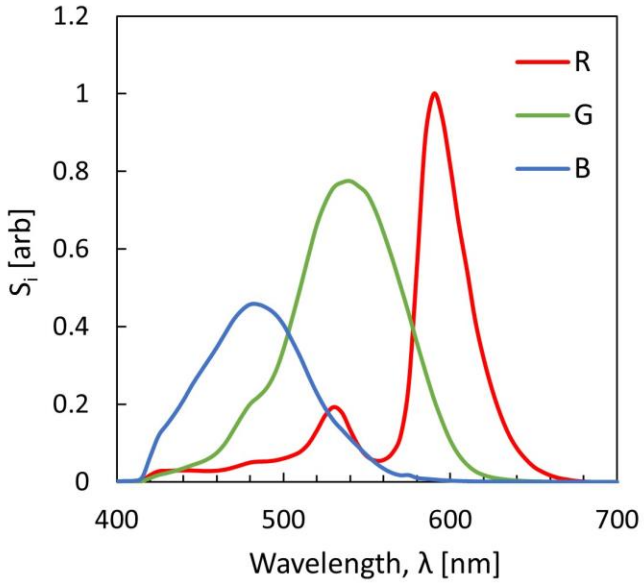

Fig. 2.3. Measured spectral response of the D610 camera and BG62 filter.

temperature lookup table, shown in Fig. 2.4, is generated for a grey body, and for soot, for the three two-color ratios: blue/green, blue/red, and green/red. The grey body temperature lookup

curves are verified using a blackbody calibration source (LumaSense M335). The linearity of the camera signal with exposure time is also verified.

All images are taken in raw mode to avoid the camera's built-in processing algorithms, and the

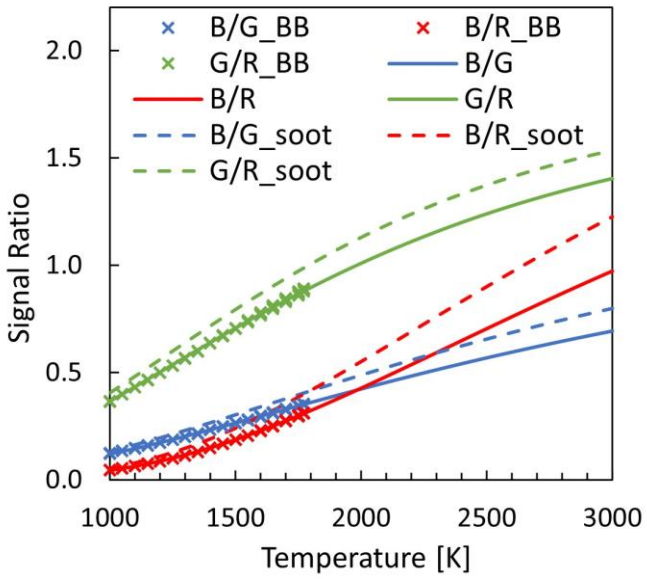

Fig. 2.4. Theoretical gray body (solid lines) and soot (dashed lines) temperature lookup table with blackbody calibration points (symbols).

white balance is set to direct sunlight. Raw NEF images are converted to TIFF files using the opensource software, dcraw [97]. All post-processing is done using MATLAB [98]. The data is 2 x 2 binned to reduce random error and high noise sensitivity in the deconvolution. The flame centerline at each row is then found using the RGB intensities. The flame is smoothed radially using the Savitsky-Golay method, and deconvoluted using the Abel inversion method, assuming the flame is axisymmetric [84]. The three two-color ratios are then calculated and plugged into a curve fit from the soot temperature lookup table to calculate the soot temperature, which typically differs by less than 30 K between the three two-color ratios. The three soot temperatures are averaged to obtain the final soot temperature, and the experimental uncertainty is estimated to be

+/- 50K [84]. The flame is assumed to be optically thin, and self-absorption is considered negligible [88]. This could impact the results of the most highly soot laden flames, but this investigation is primarily concerned with qualitative trends; a self-absorption calculation is beyond the scope of this work.

Once the soot temperature is known, soot volume fraction can be calculated using Eq. 2.9 with the absolute intensity calibration of the optical system [91]:

$$f_v = -(l_{abs}/L)\ln(1-\varepsilon_L(\lambda,T_L)(\tau_S(\lambda)/\tau_L(\lambda))(S_S(\lambda)/S_L(\lambda))\exp[-hc/k\lambda_S(1/T_L-1/T_S)]) \,, \quad (2.9)$$

In Eqn. 2.9, f_v is the soot volume fraction, λ_S is the effective wavelength of the optical system, l_{abs} is the natural length for absorption at the effective wavelength of the optical system, and L is the absorption length. The subscripts L and S denote the calibrated light source and soot, respectively. The soot volume fraction at each pixel is calculated using the effective wavelength of the optical system [88]. The soot index of refraction is calculated using the relationship given in ref. [99]. A blackbody source (LumaSense M335) is used as the calibrated light source for the absolute intensity calibration. Calibration and flame images are taken at the same distance in order to maintain a constant absorption length. The soot volume fraction is calculated directly from the flame images using MATLAB.

The characteristic total concentration of soot in a flame can be obtained by calculating the radially integrated soot volume fraction, F_v, and then the integral soot volume, V_s, which are calculated from

$$F_v(\theta) = 2\pi \int f_v(r,\theta) r dr \,, \quad (2.10)$$

$$V_S(\theta) = z_0 \int F_v(\theta) d\theta \,, \quad (2.11)$$

where r is the radial coordinate, z is the axial coordinate, and $\theta = z/z_0$ is the relative height, or nondimensional axial coordinate [100].

2.3 Results & Discussion

2.3.1 Radiation measurements

Figure 2.5 shows radiation loss fraction as a function of central stoichiometric ratio (CSR) for the methane and ethylene flames. For very low flow rates of oxygen (a CSR of 0.03 or less for ethylene and a CSR of 0.12 or less for methane), hysteresis is apparent for both fuels as a flame is not initially established on the central tube but can be ignited by ramping up the central O_2 flow and then slowly ramping it back down. When there is no flame on the central tube, a partial premixture is created. For ethylene, the partial premixture significantly increases thermal radiation with increasing CSR, presumably due to enhanced soot formation, as seen in [101]. Thermal radiation from the methane flames also increases, but the effect is much less significant likely due to its already low soot concentration and thermal radiation.

Once an inner flame is established on the central tube, the radiation loss fraction increases for both fuels, until it reaches a peak at a CSR of 0.18 for methane and 0.14 for ethylene. After the peak, the loss fraction continuously decreases for ethylene. For methane, it decreases slightly at first, but begins to increase again until a second peak is reached at a CSR of 0.46. Overall, when an inner flame is present, low flow rates of oxygen in the central tube can increase the radiation emission from the methane flame by 20% at a CSR of 0.18 and from the ethylene flame by 26% at a CSR of 0.14. Larger flows of oxygen in the central tube monotonically decrease the radiant emission from the ethylene flames but can increase emission from the methane flames by up to 31% (at a

CSR of 0.46). The difference in radiant behavior for the two fuels at high CSR values will be discussed further below.

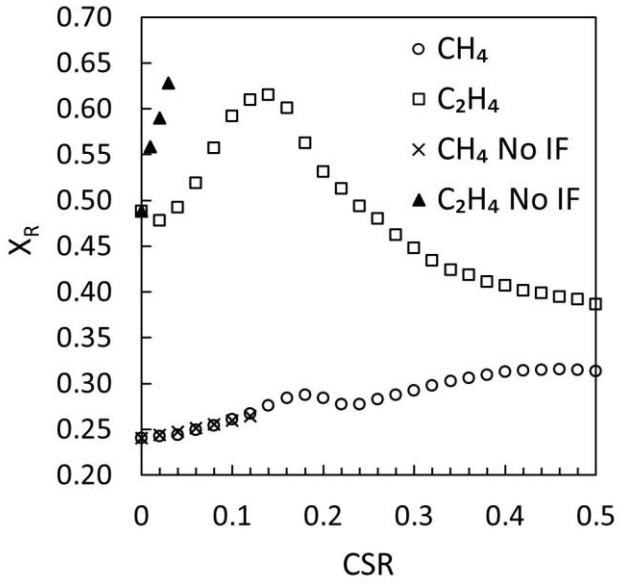

Fig. 2.5. Radiation loss fraction as a function of CSR. Open circles (methane) and open squares (ethylene) denote radiation measurements when a flame is apparent on the central tube. X's (methane) and closed triangles (ethylene) denote radiation measurements when no flame is apparent on the central tube, creating a partial premixture.

2.3.2 Experimental conditions & flame shape

Based on Fig. 2.5, five flames for each fuel are examined in detail to elucidate the effect of the inner flame on thermal radiation. The experimental conditions for these flames are outlined in Table 2.1.

Table 2.1: Experimental conditions.

CSR	Q_{O2} central [sccm]	V_{O2} central [cm/s]	Re_{O2} central
CH_4			
0.00	0.0	0.0	0.0
0.14	55.8	25	36
0.18	71.7	33	46
0.22	87.7	40	56
0.46	183.4	83	117
C_2H_4			
0.00	0.0	0.0	0.0
0.10	36.2	16	23
0.14	50.7	23	32
0.18	65.2	30	42
0.50	181.2	82	116

Figure 2.6 shows an image of each flame in Table 2.1. The images contain a slight blue/green hue, owing to the BG62 filter. The camera settings for each image are adjusted such that the maximum camera signal is just below the saturation limit. The ethylene flames are significantly more luminous than the methane flames, due to the higher soot concentrations and flame temperatures

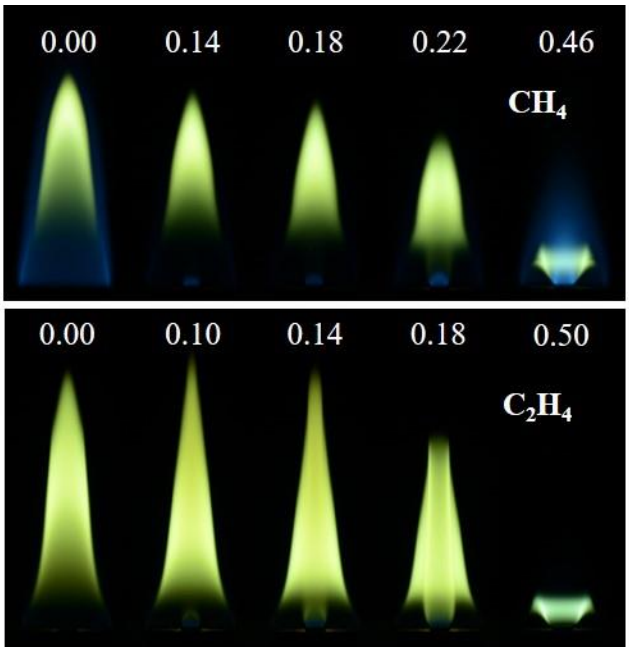

Fig. 2.6. Image of each flame in Table 2.1. The CSR is denoted above each image.

in the ethylene flames. As the CSR increases, the height of luminous soot typically decreases due to increased fuel consumption at the inner reaction zone. The soot height of the ethylene flame initially increases likely due to a change in flame structure, but then decreases.

Based on the theoretical analysis of tri-axial Burke-Schumann flames by Chao et al. [102], we define two regimes of flame shape for the tri-coflow flame, shown schematically in Fig. 2.2: *over-ventilated flames* that have more than enough oxidizer to completely consume the fuel, resulting in the flame sheet curving toward the fuel side, and *under-ventilated flames* that do not contain enough oxidizer to completely consume the fuel, resulting in the flame sheet curving towards the oxidizer side. In this investigation, the outer flame (fuel/air) is always over-ventilated, and the inner flame (fuel/oxygen) transitions from under- to over-ventilated. The transition from under- to over-ventilated begins when the central oxygen stream breaks through the tip of the outer flame (after a CSR of 0.18 for methane and 0.14 for ethylene, shown in Fig. 2.6).

2.3.3 Soot temperature and soot volume fraction

Figures 2.7 and 2.8 show 2D contour plots of soot volume fraction and soot temperature, respectively, for each flame in Fig. 2.6. The soot volume fraction for each fuel in Fig. 2.7 is on its own respective log scale. As the CSR is increased, the height where soot inception first occurs decreases as the inner flame produces soot and provides energy in the center of the flame to enhance pyrolysis. For the high CSR flames, the temperature at the height of soot inception gets very high due the high temperature inner oxygen/fuel flame. The height of soot burnout (i.e., the height of luminous soot) typically decreases likely due to enhanced fuel consumption at the inner flame and enhanced soot oxidation rates [80].

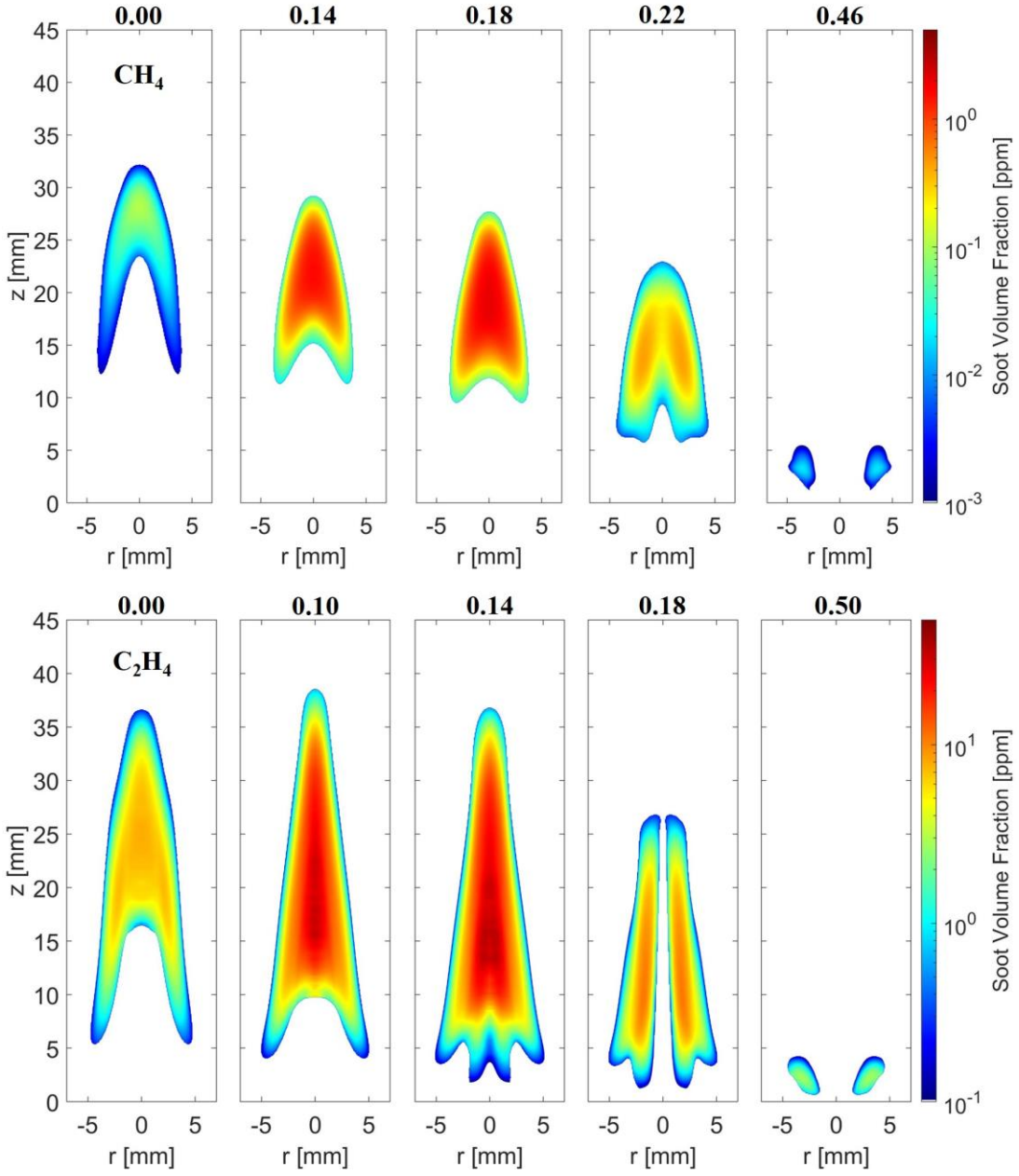

Fig. 2.7. Two-color ratio pyrometry measurements of soot volume fraction for each flame in Table 2.1. The soot volume fraction for each fuel is on its own respective log scale.

In Fig. 2.7, the peak soot volume fraction increases with CSR until the inner flame begins to transition to over-ventilated (after a CSR of 0.18 for methane and 0.14 for ethylene). In these flames, the soot concentration is significantly increased, changing the structure of the flame. This

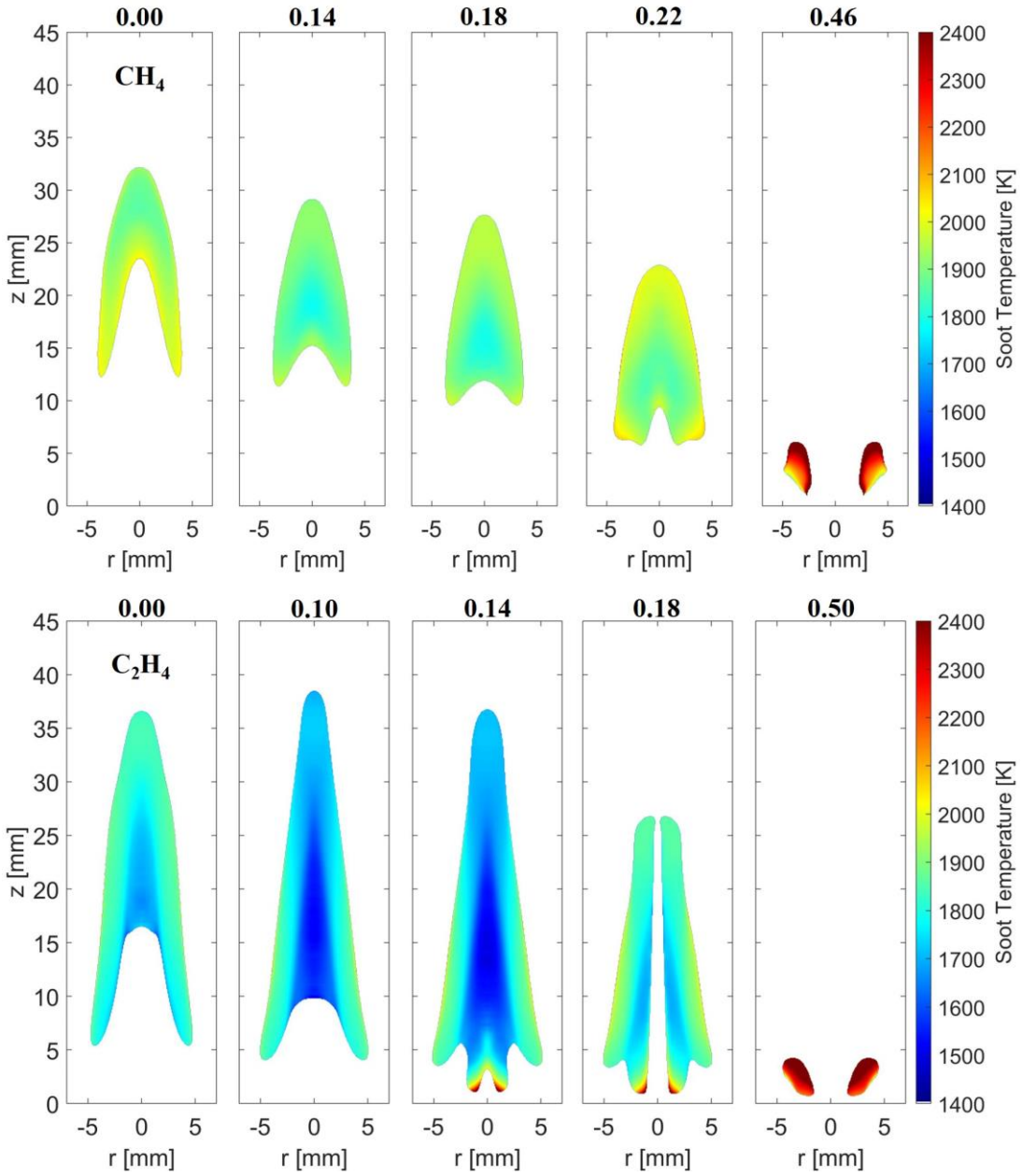

Fig. 2.8. Two-color ratio pyrometry measurements of soot temperature for each flame in Table 2.1.

increase in soot is likely a result of the additional area for soot formation at the inner flame, energy from the inner flame enhancing pyrolysis in the fuel rich region, and enhanced soot growth by producing soot in a fuel rich region. It is noteworthy that the heat release from the inner oxygen/fuel flame at a CSR of 0.11 for methane and 0.08 for ethylene provides enough energy to

heat the entire flow of fuel to 1600 K, indicating that the inner flame may be acting primarily as an energy source to heat the fuel. Furthermore, in these tri-coflow flames with under-ventilated inner flames, the soot residence time is not significantly changed, as the location of soot inception is decreased.

Figure 2.8 shows that the soot temperature in the soot laden region decreases for the ethylene flames, and remains relatively unchanged in the methane flames, with increasing CSR for under-ventilated inner flames. For both fuels, when the inner flame is under-ventilated, the soot produced by the inner flame, and the subsequent higher radiation emitted from this soot, suppresses the high temperatures that might be expected from oxy-fuel combustion. Once the inner flame begins to transition to over-ventilated, the peak soot volume fraction in these flames decreases with CSR for both fuels, owing to reduced soot residence time and enhanced soot oxidation rates [80]. The soot temperature increases significantly in these flames due to the high temperature oxygen/fuel flame and reduced concentration of soot.

Radiation from soot at every location in each flame of Table 2.1 can be estimated using the measured soot temperatures and soot volume fractions in Figs. 2.7 and 2.8. The soot emissivity at each location is calculated using the exact non-gray closed form expression of refs. [103,104], given as

$$\varepsilon_s = 1-(15/\pi^4)\psi^{(3)}(1+x)\,, \tag{2.12}$$

$$x = CLT/c_2\,, \tag{2.13}$$

$$C = 36\pi f_v(n^2k/([n^2-(nk)^2+2]^2+4n^2k^2))\,, \tag{2.14}$$

where $\psi^{(3)}$ is the pentagamma function, c_2 the second radiation constant of Planck's law, and n and k the real and imaginary components of the index of refraction of soot, respectively, calculated as in section 2.2.3 [99]. Using the calculated local soot emissivities and measured local soot temperatures, the local soot radiation, q_r'', is calculated using

$$q_r'' = \sigma\varepsilon_s(T_s^4 - T_\infty^4) \,, \tag{2.15}$$

where σ is the Stefan-Boltzmann constant and T∞ is the ambient temperature (295 K). The total soot radiation from each flame is then calculated by integrating the local soot radiation values.

Figures 2.9a and 2.9b show the experimentally measured total flame radiation (cf. Fig. 2.5) and the calculated total soot radiation from the methane and ethylene flames, respectively, in Table 2.1 as a function of CSR. Figure 2.9a shows that product gases are always the dominate radiant emitter in these methane flames. However, the increase in total radiant emission that occurs at low CSR values when the inner flame is under-ventilated (up to a CSR of 0.18) is largely due to an increase in soot radiation. Once the inner flame transitions to over-ventilated, and the radiation begins to increase further, this increase in radiant emission is due to increasing radiation from product gases, as the soot radiation decreases.

Figure 2.9b shows that soot is the dominant radiant emitter in these low CSR (up to a CSR of 0.14) ethylene flames. Similar to the low CSR methane flames, the increase in total radiant emission from ethylene flames with under-ventilated inner flames in Fig. 2.9b is due to increased soot radiation. Once the inner flame transitions to over-ventilated, both the total and soot radiation decrease monotonically, and eventually, at high CSR values, product gases become the dominant radiant emitter in these ethylene flames.

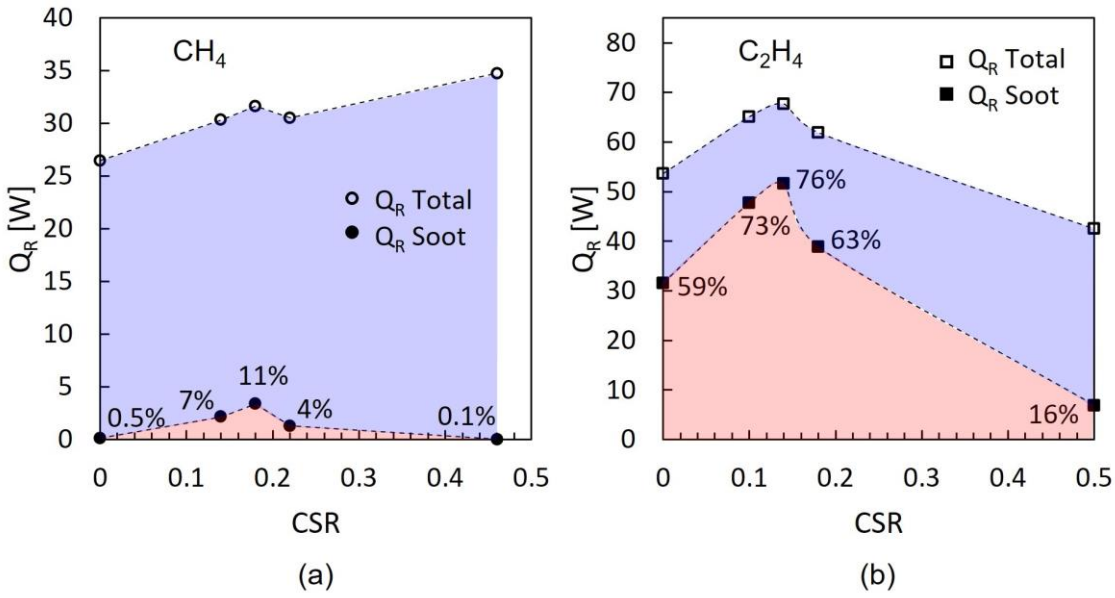

Fig. 2.9. Total flame and soot radiation heat loss rate as a function of CSR for the **(a)** methane and **(b)** ethylene flames in Table 2.1. The red shaded areas denote radiation from soot and the blue shaded areas denote the balance of the total radiation (attributed to radiation from product gases.) The percentages near the soot radiation for each flame indicate the percent of the total radiation attributed to soot radiation.

Using the data in Figs. 2.7 and 2.8, the integral soot volume and the average soot temperature in the soot laden region (i.e., the average soot temperature where the soot volume fraction is greater than 75% of the peak soot volume fraction) are calculated and plotted in Fig. 2.10 as a function of CSR. The integral soot volume is seen to increase with increasing CSR for both fuels until a CSR of 0.18 for methane and 0.14 for ethylene, just before the inner flame begins to transition to over-ventilated. This also coincides with the initial peak in total radiation and soot radiation for each fuel (cf., Fig. 2.9), indicating that the increase in thermal radiation with increasing CSR for flames with under-ventilated inner flames is a result of the increased concentration of soot.

Fig. 2.10 also shows that the soot temperature in the soot laden region decreases in these low CSR ethylene flames and remains relatively unchanged in the methane flames. This is somewhat counterintuitive. If the radiation is higher, one might expect the temperature to be higher,

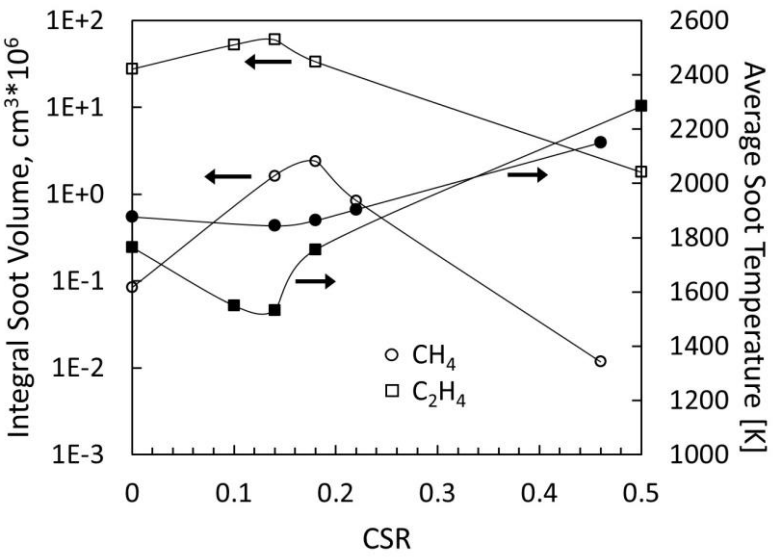

Fig. 2.10. Integral soot volume and average soot temperature in the soot laden region (where the soot volume fraction is greater than 75% of the peak soot volume fraction) as a function of CSR for each flame in Table 2.1.

particularly considering the high flame temperatures that result from an oxygen/fuel flame. However, the increased soot concentration significantly enhances the overall soot emissivity, thus increasing soot radiation, and decreasing the temperature of the flame. The decreasing or constant soot temperature in the soot laden region of these flames is a consequence of the increased soot concentration and subsequently increased radiation heat transfer. Thus, the increased thermal radiation due to the under-ventilated inner oxy-fuel flames is a result of increased soot concentration, and subsequently, soot emissivity, not hotter soot particles or product gases.

In Fig. 2.10, it is also interesting to note that in the methane flames, the integral soot volume increases by a factor of 29 from a CSR of 0 to 0.18 and yields a 20% increase in total radiation. In contrast, the integral soot volume in the ethylene flames increases by a factor of only 2.2 from a CSR of 0 to 0.14 and yields a 26% increase in total radiation. This result illustrates the intrinsically low propensity for soot formation in methane flames, and the importance of soot for radiation heat transfer in hydrocarbon flames. Additionally, the relatively large increase in soot concentration in

the methane flames suggests that the high local temperatures near the inner reaction zone and energy provided by the inner flame help overcome the initiation barrier to soot formation in methane combustion. Furthermore, when the inner flame is under-ventilated, the soot that is formed at the inner reaction zone is driven into a fuel rich region, which is beneficial for soot growth. Investigations in normal coflow methane diffusion flame have shown that oxygen enrichment of the outer coflow typically leads to an increase in soot volume fraction, but also an increase in soot oxidation rates and a significant decrease in flame height [75]. These prevent the soot volume fraction from increasing to the levels of the methane flames seen herein.

Once the inner flame begins to transition to over-ventilated, Fig. 2.10 shows that the integral soot volume decreases and the average soot temperature in the soot laden region increases with CSR for both fuels. Despite the increasing soot temperature in these high CSR ethylene flames, the decreasing soot concentration results in decreasing total flame radiation and soot radiation (cf. Fig. 2.9) because soot is the dominant radiant emitter until high CSR values when the soot concentration is low and the temperature high, such that product gases become the dominant radiant emitter. For the high CSR methane flames, because product gases are always the dominant emitter, the effect of decreasing soot concentration is second order, and the increasing temperature results in increased total radiation owing to radiation from high temperature product gases.

2.4 Conclusions

A fundamental study of the effect of oxygen enrichment on thermal radiation when oxygen is introduced into the center of methane and ethylene coflow diffusion flames was conducted. The effect of systematically increasing the oxygen flow rate in the central tube was investigated. The following results were obtained:

(1) When adding small amounts of oxygen to the center of a normal coflow diffusion flame and an inner flame is present, the inner flame sheet remains under-ventilated and the total thermal radiation emitted from the flame increases owing to increased soot radiation that results from increased soot concentration (i.e., soot emissivity). The soot temperature in the soot laden region of these low CSR flames decreases, or remains relatively constant, with increasing CSR. The high temperatures that would typically result from the inner oxygen/fuel flame are suppressed by the large concentration of soot particles radiating heat from the flame.

(2) For high flow rates of central oxygen, the inner flame sheet begins to transition to over-ventilated and the flame height significantly decreases. In these flames, the soot concentration decreases due to decreased residence times and enhanced oxidation rates, and the soot temperature in the soot laden region increases, with increasing CSR. For these methane flames, radiation increases with increasing CSR, owing to the increasing temperature, and product gases being the dominant radiant emitter. For these ethylene flames, radiation decreases with increasing CSR, owing to decreasing soot concentration, despite the increasing temperature.

(3) Product gases (e.g., CO_2 and H_2O) are the dominant radiant emitter in the methane flames studied. Soot is the dominant radiant emitter in the ethylene flames studied until high CSR values when the soot concentration is significantly reduced, and high temperature product gases take over as the dominant radiant emitter.

(4) The radiant emission from the normal coflow methane flame is less than half that of the normal coflow ethylene flame. Large amounts of central oxygen can increase the radiation from the coflow methane flame by 31% through higher gas temperatures, but this is likely not economically practical. Small amounts of central oxygen can increase the radiation from the methane flame by

20% through higher soot concentration, but these flames still emit 41% less radiation than that of the coflow ethylene flame.

This study on the impact of central oxygen on thermal radiation in laminar methane and ethylene coflow diffusion flames has elucidated the fundamental radiation characteristics of these flames. While these results show that soot, and subsequently, radiation in methane flames can be enhanced by adding a central oxygen stream, further research must be conducted in order to increase radiant emissions from methane flames to the point that natural gas can be an effective drop-in replacement for fuels with a higher propensity for soot formation.

Chapter 3: Effect of toluene dopant on thermal radiation from laminar tri-coflow methane diffusion flames with central oxygen

3.1 Introduction

Natural gas combustion is widely used in industrial processes and for energy generation, owing to its low cost and modest emissions. Natural gas is composed of primarily methane (CH_4) (>87%), which has a low propensity for soot formation relative to other hydrocarbon fuels due to its low carbon-to-hydrogen ratio and lack of a carbon-carbon bond. The limited soot formation in natural gas flames results in poor radiation heat transfer when compared with other fossil fuels, such as coal or oil. Because of this, the radiative properties of natural gas have become a matter of increasing interest. In order for natural gas to be effectively used as a replacement for more polluting fossil fuels, the fundamental combustion and radiative characteristics of methane and natural gas flames must be elucidated.

Oxygen-enriched combustion is a promising method for increasing radiation heat transfer from natural gas flames, and it has been successfully applied to a variety of applications such as boilers, glass kilns, and incinerators [59,60]. The increase in thermal radiation occurs due to increases in: 1) flame temperature, 2) product gas emissivities, and 3) soot concentration [61,62]. Furthermore, oxygen-enriched combustion has been shown to improve flame stability and thermal efficiency, and to facilitate carbon capture and storage [59,105].

In a normal coflow diffusion flame configuration, the oxidizer in the outer coflow is typically air. In oxygen-enriched combustion, oxygen is added to, or replaces, the air in the outer coflow. However, adding oxygen to the outer coflow can be expensive due to the high cost of cryogenic air separation and the large amount of oxygen needed to have a significant influence on flame temperature [62].

Using a triple port burner, Irace et al. [52] recently investigated the effect of introducing a small amount of oxygen into the central tube of a tri-coflow diffusion flame on thermal radiation, while maintaining an outer coflow of air. They found that low flow rates of oxygen in the central tube can increase thermal radiation from methane/air flames by 20%. This increase was due to higher soot concentrations, not higher temperatures [52]. The high temperatures associated with oxygen-enriched combustion were suppressed as the larger concentration of soot radiated more energy from the flame. Furthermore, they found that in these methane flames, the soot concentration was increased by more than 28 times, indicating that the inner oxygen/fuel flame helped to overcome the methyl radical reaction barrier to soot formation (i.e., increased the formation of precursors that lead to the formation of the first aromatic ring). Unfortunately, these methane flames still emitted much less radiation than that of a sootier fuel such as ethylene. That study, however, demonstrated the ability to significantly increase soot formation with a small amount of oxygen when appropriately placed, and illustrated the importance of soot concentration and emissivity on the thermal radiation from flames.

Fuel additives are a promising, practical method of controlling soot formation and, subsequently, thermal radiation. McEnally et al. [106,107] investigated methane/air diffusion flames doped with C3 and C4 hydrocarbons and found that the dopants increase soot formation because they undergo reaction sequences that raise the concentrations of the benzene and phenyl radical precursors (e.g., C_3H_3, C_4H_3, and C_4H_5). Consalvi et al. [108] investigated soot formation in methane/air diffusion flames doped with n-heptane/toluene and iso-octane/toluene and found that soot production is enhanced monotonically with increasing toluene content. Furthermore, they found that soot inception is enhanced and occurs at a lower height above the burner [108]. Daca et al. [109] and Gu et al. [110] investigated methane/air diffusion flames doped with n-heptane and toluene at

elevated pressures and found that soot formation increases with toluene addition and that the attack of toluene with the H radical is a significant pathway to the formation of benzene. Zelepouga et al. [100] found that the addition of acetylene to a methane/air flame has much less effect on soot formation than the addition of PAHs due to the rate limiting step of PAH formation. Furthermore, they found that the effect of PAH addition on soot formation becomes substantially stronger with oxygen-enrichment, while the relative impact of acetylene is the same with and without oxygen enrichment [100].

In an effort to increase thermal radiation from methane flames, this work investigates the effect of toluene (C_7H_8) addition on thermal radiation from laminar methane diffusion flames in a tri-coflow burner with central oxygen enrichment. The substantial increase in soot concentration that results from the introduction of central oxygen, coupled with the addition of toluene, could lead to a synergistic relationship that significantly increases soot concentration and, subsequently, thermal radiation in methane flames.

The ability to control soot formation and thermal radiation in methane flames is of fundamental importance to improving the use of natural gas in practical combustion applications.

3.2 Experimental methods

3.2.1 Experimental configuration

The triple port burner employed is described in detail in Irace et al. [52]. The burner consists of three concentric tubes, supplying air in the outermost tube, fuel (CH_4 or C_7H_8-doped CH_4) in the middle tube, and oxygen in the central tube. Figure 3.1 shows a schematic diagram of the burner. A stable, uniform flow field is established in the fuel and air tubes using stainless steel honeycomb

flow straighteners. The central oxygen tube is at least twice the length necessary for fully-developed laminar flow.

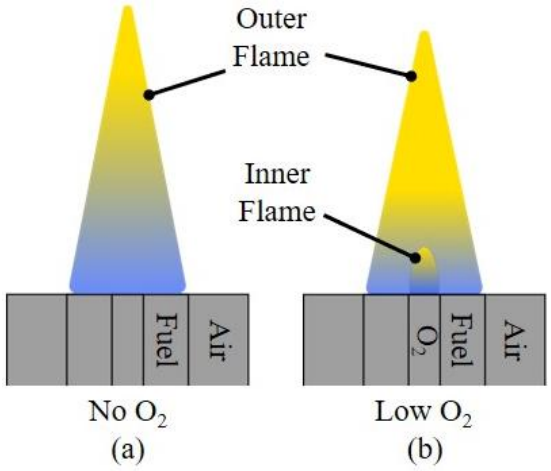

Fig. 3.1. Experimental configuration with an illustration of the key flame shapes observed. The outer flame is always over-ventilated. **(a)** No central O_2 flow. **(b)** Low central O_2 flow (under-ventilated inner flame).

The flow rates of oxygen and methane are controlled with rotameters (Matheson Model FM-1050 Series), and the outer air flow rate is controlled using a sonic nozzle. Because toluene is a liquid at room temperature, toluene is supplied via a bubbler with methane as the carrier gas. The concentration of toluene in the gas phase is obtained by measuring the liquid temperature and assuming saturation. The rate of toluene delivery was verified by weight loss measurements in calibration runs.

A constant flow rate of air at 60 slpm is maintained in the outermost tube to ensure an over-ventilated outer fuel/air flame. The normal coflow methane flame with no toluene or oxygen addition is used as a reference flame. As in ref. [52], the flow rate of central oxygen is systematically increased and is quantified using the central stoichiometric ratio (CSR) given by,

$$CSR = Q_{O2,central}/(\nu_{O2,CH4}Q_{CH4} + \nu_{O2,C7H8}Q_{C7H8}) , \quad (3.1)$$

where v_{O2} is the stoichiometric coefficient for oxygen for a given fuel and Q is the volumetric flow rate.

Table 3.1 outlines the experimental conditions for the toluene-doped flames investigated, where Y is mass fraction, $\dot{m}$ the mass flow rate, and Q_C the chemical heat release rate. In these experiments, the methane flame is doped with 0.5, 1, 1.5, or 2 vol% toluene, which results in an increase in the adiabatic flame temperature of 10 K or less. The oxygen consumption rate is held constant, which results in a nearly constant (within 0.4%) theoretical chemical heat release rate. Because the oxygen consumption rate is held constant, the oxygen flow rate for a given CSR and amount of dopant is also constant (i.e., the denominator of Eq. 3.1 is constant).

Table 3.1
Experimental conditions for toluene dopant.

vol% C_7H_8	Y_{CH4}	Y_{C7H8}	$\dot{m}_{Total}$ [mg/s]	$Q_{C,Total}$ [W]
0.0	1.00	0.00	2.20	110
0.5	0.972	0.028	2.21	110
1.0	0.945	0.055	2.23	110
1.5	0.920	0.080	2.24	110
2.0	0.895	0.105	2.25	110

3.2.2 Radiation Loss Fraction

The radiation loss fraction, X_R, is given by

$$X_R = Q_R/Q_C \,, \tag{3.2}$$

and is used to quantify the total rate of radiant emission, Q_R, from the flame relative to the heat release rate, Q_C [85]. To obtain Q_R, the total radiant heat flux, q_r, is measured using a wide-angle radiometer composed of stackable lens tubing and a xenon-encapsulated thin-film thermopile with a calcium fluoride (CaF_2) window. The radiometer has a transmission bandwidth of 0.13 to 11 μm

and was calibrated using a blackbody calibration source (LumaSense M335). The detector is placed 14 cm from the flame and has a field of view of 10 cm [52]. Radiation measurements are reproduceable within 4%. Assuming spherically isotropic emission, the total radiant loss is given by,

$$Q_R = 4\pi R^2 q_r \,, \tag{3.3}$$

where R is the distance from the flame centerline to the detector. The heat release, Q_C is given by

$$Q_C = \dot{m}_{Fuel} LHV \,, \tag{3.4}$$

where LHV is the lower heating value.

3.2.3 Soot temperature

Soot temperature is measured via two-color ratio pyrometry using a digital camera. The measurement technique and optical system are described in detail in [52]. Imaging is performed using a Nikon D610 digital single-lens reflex (DSLR) camera, which has a full frame (36 mm x 24 mm) 24.3 MP FX format complementary metal-oxide-semiconductor (CMOS) sensor with a Bayer color filter array (CFA).

A Schott BG62 filter is used to reduce the intensity of the red color channel. The spectral response of the optical system (i.e., BG62 filter and D610 camera) was calibrated by imaging a 2800 K tungsten lamp through a monochromator, as in [52]. The dispersion exponent is assumed to be a constant value of 1.38 to match previous work [88,91]. A grey body/soot temperature lookup table for three two-color ratios (B/G, G/R. B/R), seen in Fig. 3.2., is generated by integrating Plank's

Law over the visible region, while accounting for the spectral efficiency of each color channel over a temperature range of 1000 to 3000 K [52,88].

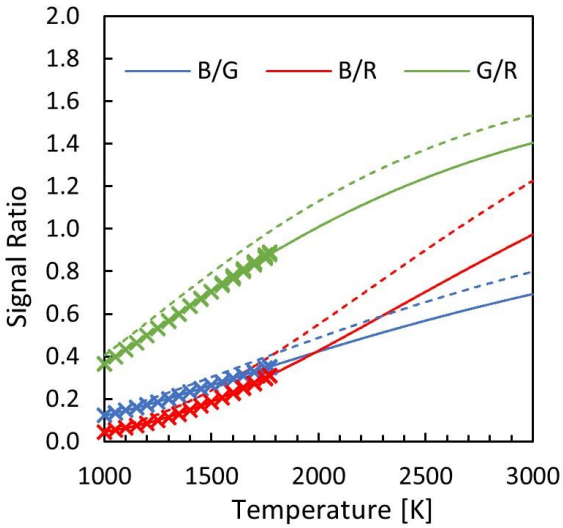

Fig. 3.2. Theoretical gray body (solid lines) and soot (dashed lines) temperature lookup table with blackbody calibration points (symbols).

All images are taken in RAW mode and converted to 16-bit tiff images using the opensource software, dcraw [97]. All post processing is done in MATLAB using the methods of [52]. The final soot temperature is taken as the average of the three two-color ratio soot temperatures, which typically differ by less than 30 K. The experimental uncertainty is estimated to be ± 50 K [84]. The emission is assumed to be optically thin, and self-absorption is considered negligible [83]. This could impact the results of the most highly soot laden flames, but this investigation is primarily concerned with qualitative trends and a self-absorption calculation is beyond the scope of this work.

3.2.4 Soot volume fraction

The soot volume fraction is calculated as in refs. [52,88,91], using the measured soot temperature at each pixel and an absolute intensity calibration with a blackbody furnace. The integral soot volume is used to characterize the total concentration of soot in each flame. The radially integrated soot volume fraction, F_v, and the integral soot volume, V_s, are calculated using,

$$F_v(\theta)=2\pi\int f_v(r,\theta)r dr\,, \tag{3.5}$$

$$V_s=z_0\int F_v(\theta)d\theta\,, \tag{3.6}$$

where r is the radial coordinate, z is the axial coordinate, and $\theta=z/z_0$ is the relative height, or nondimensional axial coordinate [100].

3.3 Results & Discussion

Figure 3.3 shows the radiation loss fraction as a function of CSR for each of the conditions in Table 3.1. As in ref. [52], upon addition of oxygen to the central tube there is a region of hysteresis in which an inner flame is not initially established, creating a partial premixture. An inner flame can be ignited by ramping the oxygen flow up, and then slowly ramping it back down. When an inner flame is not established, the pure methane flame is relatively unaffected, presumably due to its already low radiant emission and small concentration of soot [52]. In contrast, upon addition of toluene, the radiation initially decreases relatively significantly with partial premixing, but then begins to level off or slightly increase. This behavior is attributed to the partial premixture initially decreasing the soot concentration due to dilution and suppressive chemical effects of oxygen, and then increasing the soot concentration upon further addition of oxygen due to increased

temperature and enhanced pyrolysis/ring formation, as observed in the partially premixed methane flames in [111-113]. This effect of the addition of small quantities of oxygen on soot formation has also been observed in other fuels such as propane [101,114].

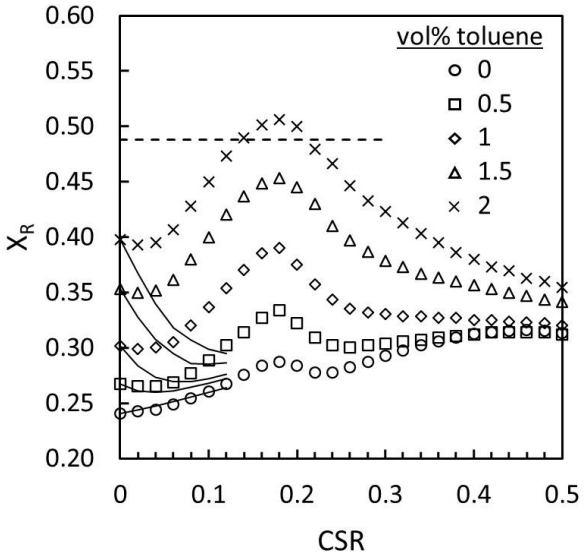

Fig. 3.3. Radiation loss fraction as a function of CSR for for various volume percents of toluene dopant. Symbols denote measurements when an inner flame is established. Solid lines denote measurements when an inner flame is not established, creating a partial premixture. The amount of dopant for each solid line can be determined by the corresponding symbol at a CSR of 0.The horizontal dashed line is the radiation loss fraction of the normal coflow ethylene flame in [52].

When an inner flame is established, the radiation loss fraction increases for each amount of dopant to a peak at a CSR of 0.18. Similar to the methane tri-coflow flames of [52], after a CSR of 0.18, the inner flame begins to transition to over-ventilated (i.e., the inner oxygen/fuel flame sheet breaks through the tip of the outer flame), resulting in a significant change in flame shape. In these high CSR flames with an over-ventilated inner flame, further increase in the CSR for 0 and 0.5 vol% toluene flames leads to an initial decrease in the radiation loss fraction, but it then increases again to a second peak. For the 1, 1.5, and 2 vol% toluene flames, after a CSR of 0.18, further addition of oxygen leads to a monotonic decrease in the radiation loss fraction.

It should be noted that the radiation loss fraction for the 2 vol% toluene flames with relatively low flow rates of oxygen (i.e., CSR values of 0.14 to 0.20) have a higher radiation loss fraction than that of the ethylene/air flame in ref. [52], indicating that the combination of modest central oxygen enrichment and fuel dopant can lead to a substantial increase in the radiant emission from methane flames.

Based on Fig. 3.3, the CSR 0 and CSR 0.18 flames are analyzed in detail. A CSR of 0 provides a relevant base case of a methane/air diffusion flame, while a CSR of 0.18 represents the condition where a small amount of oxygen results in a peak in radiation loss fraction for each amount of dopant in Fig. 3.3.

Figure 3.4 shows a photograph of each flame. The photographs have a slight blue/green hue, owing to the BG62 filter. For both CSR values, the height of luminous soot increases with toluene addition, which is attributed to increased soot formation. For a given amount of dopant, the visible soot height of the CSR 0 flame is greater than the CSR 0.18 flame due to fuel consumption at the inner reaction zone.

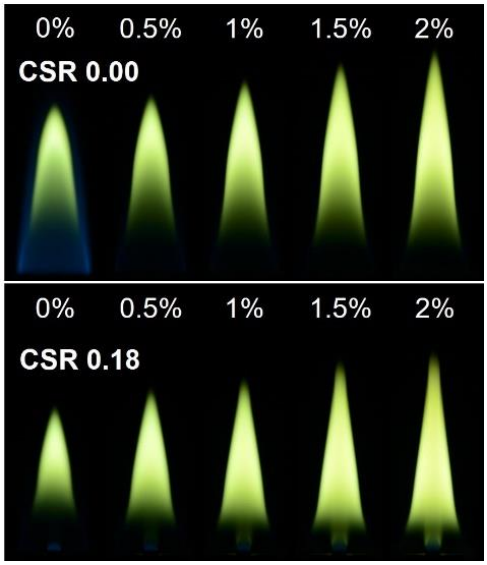

Fig. 3.4. Images of the flames examined. The volume percent of toluene dopant is denoted above each image.

To elucidate the effect of toluene addition on thermal radiation, Figure 3.5 shows the radiation loss fraction as a function of the amount of toluene dopant. The radiation loss fraction increases with increasing dopant for both CSR values. However, the linear fit for the CSR 0.18 flames has a steeper slope, indicating that the inner oxygen/fuel flame and the toluene dopant may have a synergistic relationship, as suggested in [100]. Overall, the radiation loss fraction increases by 65% when 2 vol% toluene is added to methane (CSR = 0) and by 110% when 2 vol% toluene is added, and the CSR is 0.18.

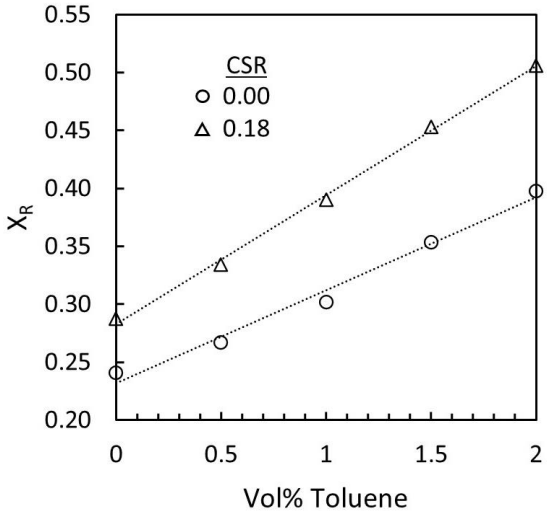

Fig. 3.5. Radiation loss fraction as a function of volume percent of toluene dopant for CSR values of 0 and 0.18.

Figure 3.6 shows 2D contour plots of the soot volume fraction for each flame in Fig. 3.4. For both CSR values, soot formation occurs sooner (i.e., at a lower height above the burner) with toluene addition, like the flames in [108]. The luminous soot height and peak soot volume fraction also increase with toluene addition. The increased soot volume fraction when adding toluene is owing to the addition of PAHs [100]. The increase in soot volume fraction when going from a CSR of 0 to 0.18 is attributed to a combination of: 1) the increased region for soot inception from the inner

flame, 2) energy from the inner flame heating the fuel and enhancing pyrolysis, 3) enhanced soot growth by driving incipient soot particles into the fuel-rich region, and 4) a longer soot residence time, owing to soot forming at a lower height above the burner [52].

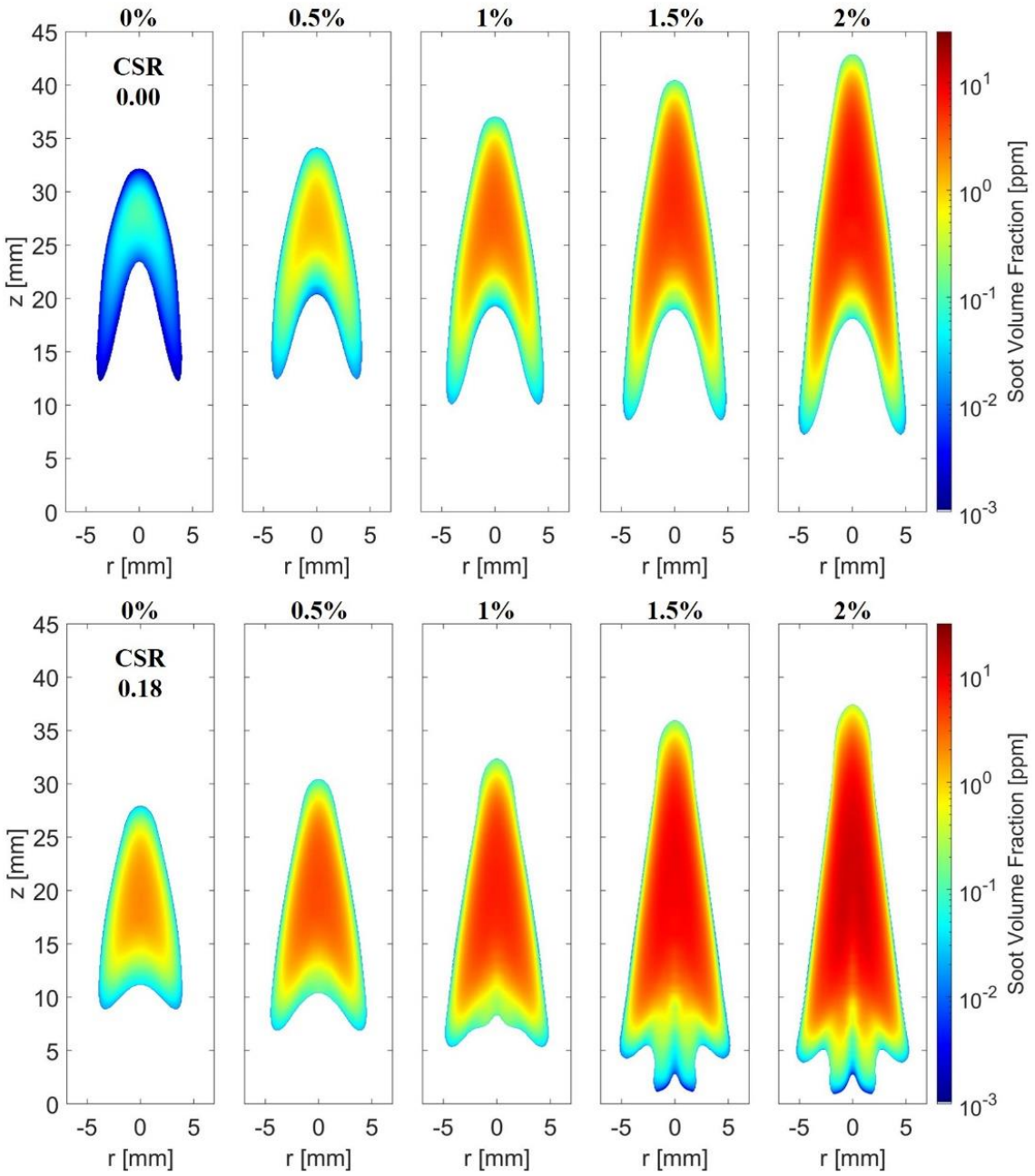

Fig. 3.6. 2D contour plots of soot volume fraction. The soot volume fraction is on a log scale.

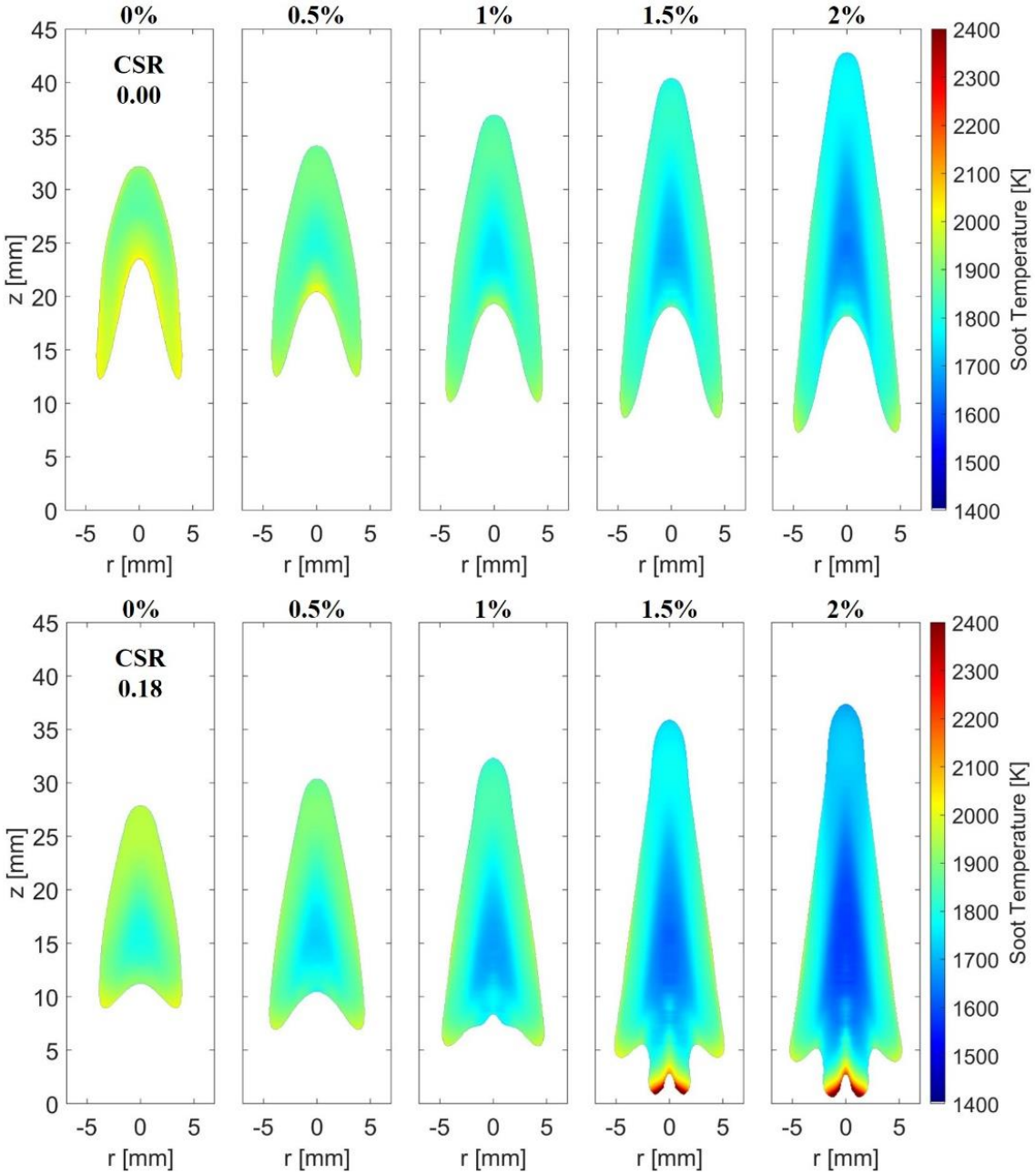

Fig. 3.7. 2D contour plots of soot temperature.

Figure 3.7 shows 2D contour plots of soot temperature. For both the CSR 0 and 0.18 flames, the soot temperature in the soot laden region decreases with toluene addition. The CSR 0.18 flames with high concentration of toluene dopant, however, have a very high soot temperature upstream near the inner flame due to the presence of the high temperature oxygen/fuel flame. Downstream

of the inner flame, the high temperatures associated with oxygen-enriched combustion are suppressed by the large amount of radiation emitted from the high concentration of soot (cf. Fig. 3.5). Thus, the increasing height of luminous soot with toluene addition is attributed to the higher concentration of soot and decreased oxidation rates at lower temperatures resulting in longer times for soot burnout. The trend of decreasing soot temperature with increasing soot concentration and radiation loss fraction was also seen in ref. [52] when small amounts of oxygen were injected into the center of an ethylene/air flame.

To further elucidate the relationship between soot concentration, temperature, and thermal radiation, Fig. 3.8 shows the integral soot volume (primary axis) and average soot temperature in the soot laden region (the region where the soot volume fraction is greater than 75% of the peak soot volume fraction) (secondary axis) as a function of radiation loss fraction. As Fig. 3.8 reveals, the radiation loss fraction increases as the soot concentration increases, even though the average soot temperature in the soot laden region decreases. As noted in [52], this might appear counterintuitive, as one would expect temperature to control radiation. However, the increase in soot concentration (i.e., higher flame emissivity) results in more radiant heat from the flame, resulting in a lower temperature.

In a normal coflow methane flame, the concentration of soot is so low that product gases are the dominant radiant emitter [52,62,83]. When the concentration of soot increases substantially, as seen herein, the effective emissivity of soot increases and radiation from soot dominates over radiation from product gases. The increase in soot emissivity increases the radiation loss fraction, causing the flame temperature to drop. Thus, in these flames, the increase in radiation loss fraction is a result of the increase in soot concentration, and the decrease in soot temperature is a consequence of the increased radiation.

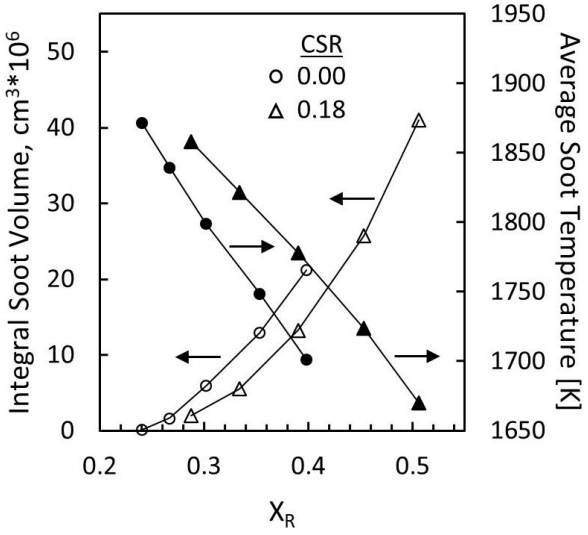

Fig. 3.8. Integral soot volume (open symbols) and average soot temperature (closed symbols) in the soot laden region (where the soot volume fraction is greater than 75% of the peak soot volume fraction) as a function of loss fraction for each flame in Fig. 3.4.

As noted in [52], in a methane tri-coflow flame with central oxygen enrichment, the inner flame helps to overcome the methyl radical reaction barrier to soot formation. When adding toluene dopant, the combination of the high-temperature inner flame - to produce species such as acetylene - and the intrinsic aromatic rings in toluene, lead to a significant increase in soot growth, allowing one to control soot formation, and subsequently, thermal radiation.

3.4 Conclusions

The effect of toluene addition on thermal radiation from laminar methane tri-coflow diffusion flames with central oxygen enrichment was investigated. The following conclusions have been made:

1) The addition of modest amounts of toluene (i.e., an aromatic fuel) to a normal methane flame can significantly increase the radiation loss fraction (e.g., by 65% for 2 vol% toluene addition) due to an increase in the soot concentration.
2) The presence of an inner oxygen/fuel flame and doping with an aromatic fuel may have a synergistic relationship that enhances soot formation, and subsequently, thermal radiation. The addition of modest amounts of toluene when an under-ventilated inner oxygen flame is present can increase thermal radiation from a normal methane flame by 110% (for 2 vol% toluene and a CSR of 0.18). The radiation loss fraction of these flames is comparable to that of sootier fuels such as ethylene and suggests that the combination of central oxygen enrichment and doping with an aromatic fuel is a promising method to control soot formation and thermal radiation in natural gas flames. The substantial increase in radiation could bring natural gas closer to being drop-in replacement for sootier fossil fuels such as coal or oil.
3) The substantial increase in radiation from these flames results in a decrease in soot temperature in the soot laden region, owing to the much larger concentration of soot radiating away more energy. The soot concentration and resulting soot emissivity control radiation in these flames.

This fundamental study has elucidated the effects of doping laminar methane tri-coflow diffusion flames with toluene. The triple port burner with central oxygen enrichment and fuel additives has been shown to be effective at significantly increasing the thermal radiation in methane flames. Further research must be conducted to apply these results to industrial scale combustion systems.

Chapter 4: Flame Design: an investigation of microgravity spherical diffusion flames for applications to oxygen-enriched combustion, carbon capture, and flame extinction – first experimental observations

4.1 Background

4.1.1 The motivation for microgravity

Stoichiometric mixture fraction, Z_{st} (i.e., the mixture fraction where the fuel and oxidizer are in stoichiometric proportions), has been shown to have a significant effect on soot formation in non-premixed counterflow flames [115-118] and co-flow flames [78,119-123]. Zst is given as

$$Z_{st} = (1+Y_{F,0}W_O\nu_O/Y_{O,0}W_F\nu_F)^{-1}, \quad (4.1)$$

where $Y_{F,0}$ and $Y_{O,0}$ represent the fuel and oxidizer mass fractions at their inlets, W_F and W_O are the fuel and oxidizer species molecular weights, and ν_F and ν_O are the fuel and oxygen stoichiometric coefficients, respectively [78]. At low Z_{st} (i.e., fuel/air flame), flames tend to be relatively sooty. At high Z_{st} (i.e., diluted fuel/enriched oxygen flame), soot formation is suppressed, and the result is a *permanently blue* flame, a term coined by Lin and Faeth [117]. The fuel, oxygen, and nitrogen mixture (i.e., Z_{st}) at which soot cannot form in a non-premixed flame, regardless of strain rate or residence time, defines the sooting limit.

Past studies have attributed permanently blue conditions to either flame structure [78,115,116,119,121,124-126], or hydrodynamics [117,118,122,123], but typically note the importance of both factors. Flame structure refers to the variation in temperature and species concentration profiles in mixture fraction space as a direct result of changes in Z_{st}. The hydrodynamic effect refers to the direction in which soot particles and precursors are convected (either into the oxidizer or into the fuel) [124].

In normal gravity, the effects of structure and hydrodynamics with changing Z_{st} cannot be independently investigated. In co-flow flames, the influence of buoyancy enhanced mixing makes it difficult to distinguish the structure of the flame. In counterflow flames, as seen in Fig. 4.1, as Z_{st} is increased, the flame sheet transitions from the oxidizer side of the stagnation point to the fuel side, changing the direction of soot particle convection and the influence of hydrodynamics. For example, at low Z_{st} (< 0.5) the flame sheet is located on the oxidizer side of the stagnation point (soot particles convect into the fuel, favoring growth) and at high Z_{st} (> 0.5) the flame sheet is located on the fuel side of the stagnation point (soot particles convect into the oxidizer, favoring oxidation) [124].

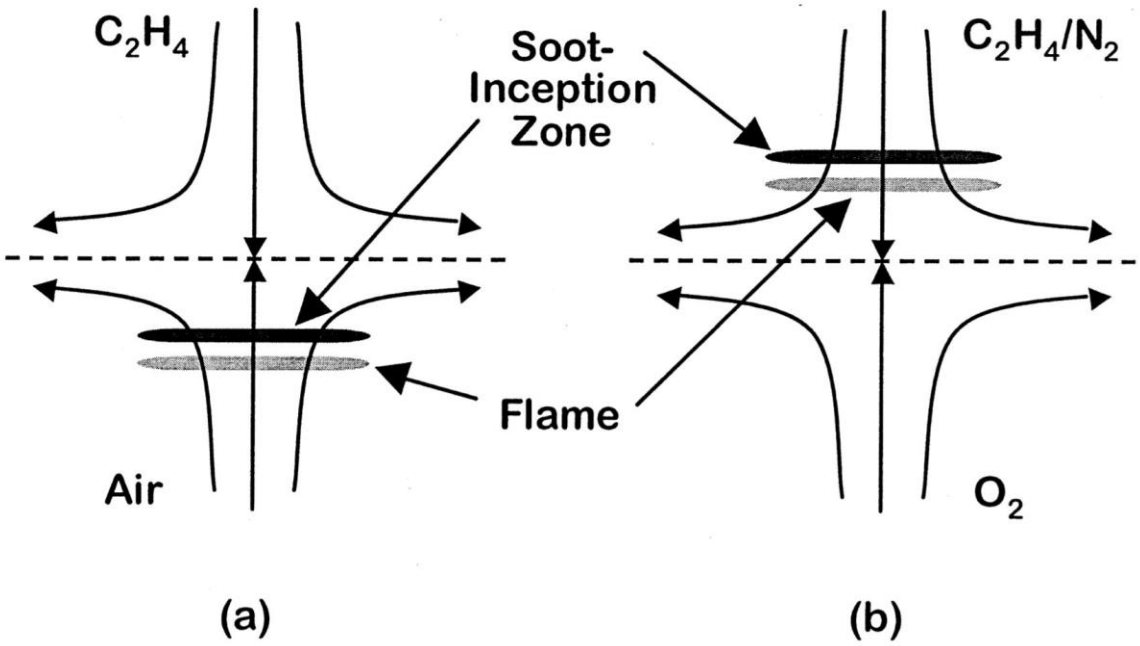

Fig. 4.1. Representation of **(a)** a counterflow flame with Z_{st} < 0.5 where the flame is on the oxidizer side of the stagnation plane and **(b)** a counterflow flame with Z_{st} > 0.5 where the flame is on the fuel side of the stagnation plane. Recreated from ref. [124].

The structural effect of changing Z_{st} is shown in Fig. 4.2 [78]. The fuel, oxygen, C/O, and temperature distributions are shown in mixture fraction space for an ethylene/air flame (Z_{st} = 0.064), and for a diluted ethylene/enriched oxygen flame (Z_{st} = 0.60) in Fig. 4.2a and b,

respectively. The dashed lines indicate the region of high temperature, where soot inception reactions are favorable. The figure shows that flames with low Z_{st} (Fig. 4.2a) have high concentrations of fuel in the high temperature region, creating ideal conditions for soot formation. In contrast, in flames with high Z_{st} (Fig. 4.2b), the region of high temperature shifts to an area of low fuel concentration and high oxidizer concentration. Skeen and coworkers [121] suggest that at low Z_{st}, there is significant propargyl and propyne (precursors of soot inception) formation on the fuel side of the radical pool at temperatures greater than approximately 1600K. Near the radical pool, at higher local temperatures where the concentration of H is significant, the reverse reaction dominates, and propargyl and propyne are destroyed. As Z_{st} is increased these two regions merge until only net propargyl consumption is observed. Kumfer and coworkers [78] reached a similar conclusion, that increasing Z_{st} closes the low temperature (temperature below which soot cannot

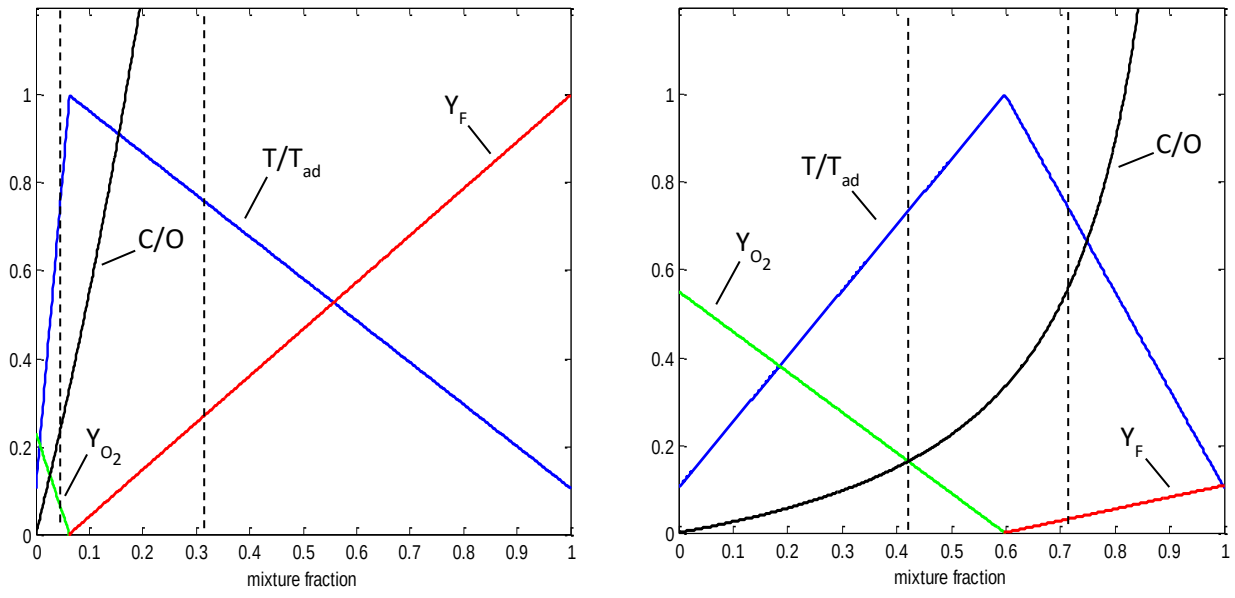

Fig. 4.2. Plots of normalized temperature, C/O ratio, and fuel and oxidizer mass fractions as a function of mixture fraction for diffusion flames with **(a)** Z_{st} = 0.064 and **(b)** Z_{st} = 0.60. The dashed lines indicate the high temperature region. Reproduced from [78].

form) and high temperature (corresponding to a location of critical C/O ratio) boundaries until they are infinitely thin, and soot has no mechanism to form.

A fundamental understanding of how altering flame structure (i.e., Z_{st}) effects sooting limits and flame dynamics is critical for optimization techniques such as pressurized oxy combustion, which is one of the leading technologies to facilitate carbon capture and storage [45,46,48,105].

In order to unambiguously demonstrate the effects of flow direction and improve the scientific understanding of soot inception and control, sooting limits are studied in microgravity spherical diffusion flames [124,125]. Microgravity spherical diffusion flames are a strain free, one-dimensional system that is ideal for modeling, but cannot be studied on Earth due to buoyancy. Droplets and porous spheres are the most common methods of producing a spherical diffusion flame in microgravity. Droplets, however, have a limited fuel supply and the fuel is always convected into the oxidizer. On the other hand, spherical diffusion flames generated from a porous spherical burner allow for a constant flow rate and a choice of the direction of convection (fuel issuing into oxidizer or oxidizer issuing into fuel). This study uses a porous sphere to generate a burner-stabilized spherical diffusion flame in microgravity. Experiments are conducted on the International Space Station (ISS) and is conducted under the experiment Flame Design, which is one of six experiments under the NASA project, Advanced Combustion via Microgravity Experiments (ACME).

4.1.2 Additional opportunities provided by microgravity research

Spherical diffusion flames in microgravity also provide a unique opportunity to study other fundamental combustion phenomena that is difficult to or un-attainable on Earth. For example, radiative extinction, which occurs at long residence times when excess radiation leads to flame

extinction, is of fundamental importance for spacecraft fire safety and large-scale wildfires. However, wildfires are unattainable on a laboratory scale because buoyancy enhanced mixing accelerates the flow field, reducing residence time. Thus, this phenomenon must be studied in microgravity. The fundamentals of radiative extinction of ethylene microgravity spherical diffusion flames at 1 bar will be elucidated in Chapter 5.

The existence of a steady-state microgravity spherical diffusion flame is also of fundamental importance for spacecraft fire safety. Steady-state microgravity spherical diffusion flames are often theorized, but they have never been observed experimentally, owing to the historic time constraints of microgravity research (i.e., 2-5 s in drop towers) in which spherical flames have either continued to grow for the duration of the experiment, or extinguished. This has led some experimentalists to doubt their existence. Exact solutions exist for steady-state spherical diffusion flames without radiation heat loss and constant transport properties, but these assumptions are non-physical, and their conclusions must be validated. In Chapter 6, the question of whether a steady-state microgravity spherical diffusion flame exists is answered.

Chapter 7 elucidates the effect of ultra-low strain on the kinetic structure and oxidation path of ethylene diffusion flames.

4.2 Introduction

Diffusion flames in microgravity have important implications for spacecraft fire safety and also offer a unique opportunity to study fundamental combustion phenomena in a buoyancy free environment. Gaseous burner-supported spherical diffusion flames in microgravity are particularly interesting, owing to their intrinsic one-dimensional structure, controllable reactant flow rate, and diffusion dominated transport. To date, owing to limitations on the duration of microgravity

attainable, no experiments have been conducted to investigate burner-supported spherical diffusion flames in long-duration microgravity.

Several spherical flame configurations have been studied in microgravity, including droplet flames [127-131], candle flames [132], and gaseous burner-supported spherical flames [124,125,133-139]. Droplet flames, however, have a fuel supply that is uncontrollable, as the vaporization rate (i.e., the fuel flow rate) is an eigenvalue of the one-dimensional problem. Additionally, the fuel concentration and the direction of convection relative to the flame cannot be varied (it is always from the fuel to the oxidizer). Candle flames suffer from similar limitations. Additionally, candle flames only have a spherically symmetric flow field at the tip of the wick. A steady solution does not exist for cylindrical flow (as induced over the length of the wick), thus the resulting flame is a hemispherical cap, which can behave quite differently from a sphere. Gaseous burner-supported spherical diffusion flames, on the other hand, offer a controllable reactant flow rate, the ability to control the concentration of the fuel supply, and the ability to operate such that the direction of convection across the flame can be from the fuel to the oxidizer or the oxidizer to the fuel, making them ideal for fundamental studies of microgravity spherical diffusion flames.

The absence of buoyancy in microgravity, coupled with the inverse-square dependence of reactant velocity on radius in a spherical configuration, results in substantially longer time scales for microgravity spherical diffusion flames to fully develop. To observe and investigate the development of a microgravity spherical diffusion flame, an adequate duration of microgravity must be available.

Previous gaseous microgravity spherical diffusion flame investigations have been limited by experimental conditions in terrestrial drop towers, which allow for only 2-5 seconds of

microgravity [124,125,133,135-137,139]. During these short times, the flame either continues to grow, or extinguishes. Owing to this intrinsic time limitation, studies of gaseous spherical diffusion flames have largely focused on extinction. In NASA's 2.2 Second Drop Tower, Chernovsky et al. [135,139] measured transient temperature and radiation intensity in ethylene spherical diffusion flames for varying diluents on both the fuel and oxidizer side of the flame. They numerically predicted flame extinction, but never achieved it experimentally. Tse et al. [133] also used the 2.2 Second Drop Tower to study the transient response of spherical flames in microgravity but did not observe extinction experimentally. Santa et al. [136,137] used the 2.2 Second Drop Tower and examined radiative extinction in ethylene spherical diffusion flames. Extinction was only observed in flames with a heavily diluted ambient.

The above referenced drop tower studies have found that spherical flames in microgravity continue to grow until either extinction, or the end the experimental duration [133,135-137,139]. Tse et al. [133] attributed this growth to fuel vapor accumulation. Many researchers suggest that as the flame grows, radiative losses increase until they become comparable to the chemical heat release and the flame extinguishes (i.e., radiative extinction) [136,137,140-144].

Figure 4.3 illustrates the theoretical temporal behavior of flame radius for a spherical diffusion flame in microgravity. These curves are solutions of gaseous spherical diffusion flames without radiation for three burner reactant flow rates [145]. Similar to drop tower observations, Fig. 4.3 shows that spherical diffusion flames in microgravity grow monotonically. The relative size of a spherical diffusion flame increases with increasing burner reactant flow rate, or with decreasing ambient reactant concentration. The location of extinction in Fig. 4.3 is arbitrary and is included to illustrate the radiative extinction seen in drop towers, where flames have grown such that radiative losses approach the chemical heat release of the flame, causing the flame to extinguish.

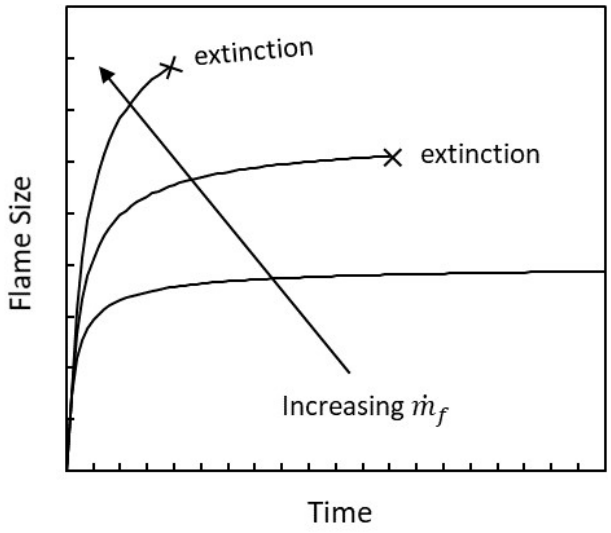

Fig. 4.3. Representation of the growth process of a spherical diffusion flame in microgravity. $\dot{m}_f$ denotes the flow rate of the burner reactant.

This study aims to investigate the dynamics of a spherical diffusion flame in long duration microgravity. By conducting experiments on the International Space Station (ISS), we have ample time in microgravity to observe fully developed spherical diffusion flames. Experimental results are compared with a numerical simulation. This investigation was conducted under the experiment Flame Design, which is one of six experiments in the NASA project, Advanced Combustion via Microgravity Experiments (ACME).

4.3 Experimental methods

4.3.1 Experimental hardware

Experiments are performed in microgravity aboard the International Space Station (ISS) in the Combustion Integrated Rack (CIR). Only normal flames (i.e., fuel issuing from the porous spherical burner into an ambient oxidizer) have been investigated thus far. The fuel is ethylene (C_2H_4), the diluent is nitrogen (N_2), and the oxidizer is an oxygen (O_2)/N_2 mixture. The ambient oxidizer is limited to 40% O_2 owing to safety concerns. Quiescent ambient conditions, with the

oxidizer at 295K, are established in a 105 L chamber with a free volume of 83.4 L. Pressure can be varied from approximately 0.5 to 1.5 bar but is 1 bar in this work.

Figure 4.4 illustrates the experimental configuration and a spherical diffusion flame. The burner is a 6.4 mm diameter porous stainless-steel sphere. Fuel is supplied to the burner via a 1.17/1.5 mm (inside/outside diameter) tube. Because this tube was found to be physically weak, it was encased in a larger 1.6/1.83 mm (inside/outside diameter) support tube to avoid damage to the fuel supply tube during assembly. The reactant supplied to the burner is either ethylene or ethylene diluted with nitrogen. Reactant flow rates are controlled with mass flow controllers with an estimated uncertainty of ± 5%. Ignition is achieved using a hot wire igniter that retracts after ignition.

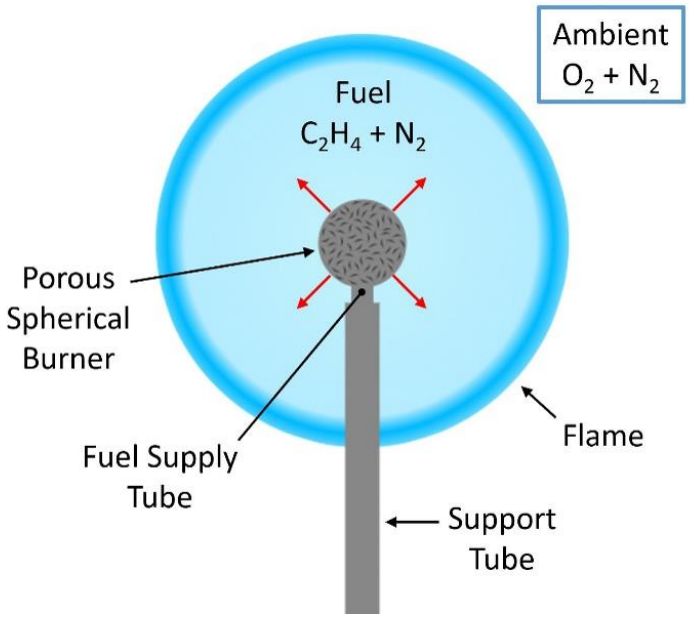

Fig. 4.4. Illustration of the experimental configuration and a microgravity spherical diffusion flame.

At the beginning of each test day, the chamber is filled to the desired pressure and oxidizer concentration. The oxygen concentration decreases marginally during the test day as the oxygen is consumed by combustion. In between experiments, a mixing fan is used to ensure a homogenous chamber environment for the next test. Combustion products (e.g., CO_2 and H_2O) are occasionally

scrubbed from the chamber to remove excess radiators and to prevent condensation on the chamber walls and optical windows.

Color images of the flames are obtained using the ACME data camera, a 1.4-megapixel color camera with a charge-coupled device (CCD) sensor. The lens on the ACME data camera is motorized and allows control over zoom, focus, and iris. The camera gain is also variable. Its framing rate is generally slow owing to exposure optimization and data limits on the ISS. The tests are also recorded at 30 frames per second (fps) using the ACME operations camera, a 0.44-megapixel CCD color video camera. Images of CH* emission are captured at 23 fps using a monochrome intensified camera. The magnifications of all three cameras were determined prior to launch and were confirmed from the porous sphere images during each ISS test.

The flame radius as a function of time is measured using the ACME operations camera video. Still images are extracted from the video and an ellipse is fit where the intensities are approximately midway between the peak blue and the ambient intensities (i.e., approximately the region of stoichiometry [146]). The flame radius is taken as the radius of the ellipse perpendicular to the fuel supply tube because the flame is quenched at the burner support tube, making it difficult to determine the location of the flame sheet parallel to the burner tube. Additionally, the flame is shifted somewhat towards the burner support tube (i.e., the flame is spherical, but no longer concentric with the porous sphere). This is likely owing to either reactant leakage where the fuel supply tube connects to the porous sphere, or to the lower temperature (and subsequently lower diffusivity) in the quenched region. Uncertainties in the flame radii are estimated at ± 0.3 mm.

Spectral irradiance is measured with three photomultiplier tubes (PMTs). One is unfiltered and detects 230 – 700 nm. The other two have bandpass filters at wavelengths corresponding to CH* (431 nm) and OH* (310 nm).

Burner temperature is measured using a sheathed 0.25 mm diameter type-K thermocouple attached to the burner surface.

4.3.2 Thin-filament pyrometry

Thin-filament pyrometry [94,147], or TFP, is performed using 14 μm SiC fibers [148] to determine the peak gas-phase temperature as a function of time. The fibers are initially straight and in the image plane of the camera, but they can expand slightly upon heating. Temperatures are determined using intensities from the three colors (i.e., wavelength bands) of the camera's color filter array (CFA): red (R), green (G), and blue (B).

The ACME data camera has a linear response with exposure time [148,149]. The camera was calibrated using a blackbody calibration source. Blackbody images were captured from 1073 to 1473 K in 50 K increments. Camera settings are adjusted at each blackbody temperature such that the images are just below saturation. The blackbody images were recorded in RAW format and converted to 16-bit TIFF files using ImageJ. The images are demosaiced in MATLAB.

For each blackbody image, the mean intensity for the R, G, and B colors is found for a 10 × 10 pixel region at the center of the area of signal. The intensity is normalized to account for different camera settings using:

$$NI = If^2/t\,, \tag{4.2}$$

where NI is normalized intensity, I is signal intensity of the pixel, f is f-number, and t is exposure time. The camera gain is constant, at its lowest setting, for all TFP and blackbody images and is therefore not included in Eq. (4.2). Owing to the linear response of the camera, NI equals the incident spectral power times a fitting constant, C_3, that accounts for the camera sensitivity and the lens. For the blackbody, this can be expressed as:

$$NI = \varepsilon_{bb} C_1 C_3 / \lambda^5 [\exp(C_2/\lambda T) - 1] , \tag{4.3}$$

where ε_{bb} is the blackbody emissivity (0.99), C_1 and C_2 are the Planck's law constants (3.742×10^8 W-μm^4/m^2 and 1.439×10^4 μm-K), λ is the effective wavelength of the color band under consideration (630 nm for R and 570 nm for G), and T is temperature.

The results of the blackbody calibration are shown in Fig. 4.5. The R pixel intensities are used to obtain the data presented herein because R has the highest signal-to-noise ratio. Nearly identical results are obtained using G. The B pixel intensities are too low to be used. An attempt was made to use two-color ratio TFP pyrometry [88], but the color ratio curves obtained from the blackbody calibration for this camera are multi-valued in this temperature range and thus cannot be used.

For TFP aboard the ISS, the exposure time is 0.4 s and there is a delay of 75 ms between images. The f-number is between 3.8 and 10.2. The diagonal field of view varies between 69 and 80 mm.

The blackbody furnace used for the camera calibration is large enough that the signal intensity is spread over a large number of pixels. the SiC fiber diameter, however, is smaller than the camera resolution and the camera is intentionally defocused to illuminate a sufficient number of pixels. To account for the fiber width in the image plane, a fill factor is introduced, defined as the unheated

fiber's width in the image divided by the width of a pixel. The fill factors here are between 0.3 and 0.35, depending on the zoom.

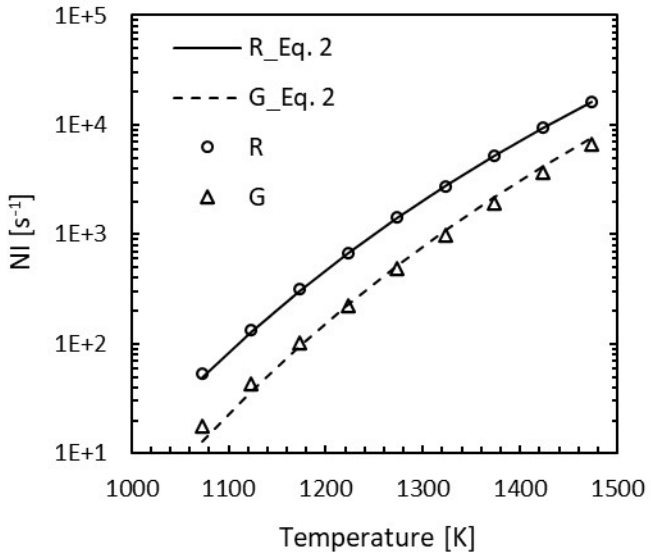

Fig. 4.5. Normalized intensity as a function of temperature. Curves denote the results from Eq. (4.3) and symbols denote blackbody measurements. The fitting constant, C_3, is 23.8 and 34.1 m^2-μm/W-s for R and G, respectively.

Fiber images are recorded in HOBJ format and converted to 16-bit color TIFF files using OMA2 [150]. For each column of pixels (i.e., the radial direction of the fiber), pixel intensities from just above and below the fiber's luminescence are identified as the local background. These are averaged and subtracted from the intensity of each pixel in the column. The R pixel intensities for each column are then averaged. Each average is divided by the fiber fill factor. This process is repeated for each column crossing the glowing fiber. This identifies two local TFP maxima, corresponding to the two locations where the fiber crosses the flame. These two are averaged for each image and converted to *NI* using Eq. (4.2).

The ACME data camera and lens were calibrated prior to launch. Since then, they have been on the ISS for several years and used for many tests. It is believed that both the transmittance of the optical path and the camera sensitivity have been reduced significantly since the calibration was

performed. To account for this, the determined *NI* is divided by a transmissivity factor of 0.36, chosen to approximately match the simulated temperatures below. The quantity *NI* is converted to fiber temperature using Eq. (4.3), where blackbody emissivity is replaced with fiber emissivity (0.88).

Fiber temperature is corrected to gas temperature by accounting for radiative losses following ref. [147],

$$T_{gas}-T_s = \sigma\varepsilon d/k_{gas}(T_s^4-T_\infty^4)[0.8237-0.5\ln(ud/a)] \,, \tag{4.4}$$

where σ is the Stefan–Boltzmann constant, ε is the fiber emissivity (0.88), d is fiber diameter (14 μm), T_s is fiber temperature, T_∞ is ambient temperature (25 °C), and T_{gas}, u, a, and k_{gas} are the local gas temperature, velocity, thermal diffusivity, and thermal conductivity, respectively. This equation is derived from an energy balance on a cylinder assuming laminar flow. In applying Eq. 4.4, α and k_{gas} were those of N_2 at the mean of T_s and T_{gas} and the local gas velocity is obtained from the numerical simulations. The uncertainty of an individual TFP measurement reported here is estimated at ± 100 K, owing to the inability to recalibrate the camera, the radiation correction, and uncertainties associated with testing in space. However, the difference in peak temperature for two times during a given test has an estimated uncertainty of ± 10 K.

Microgravity experiments, particularly on the ISS, have been proven to be challenging. Once the experimental apparatuses are launched, they generally cannot be altered or repaired, and the effects of space (e.g., cosmic rays) on the diagnostics are unknown. Additionally, diagnostic calibrations must be done on Earth prior to launch, and they cannot be recalibrated. Nonetheless, while it is difficult to acquire quantitative data on the ISS, the available diagnostics do provide valuable semi-quantitative data under conditions unattainable on earth.

4.4 Numerical model

Numerical simulations were performed using the SphDiff program used in refs. [136,137,151,152], which is a modification of Sandia PREMIX [153]. The governing equations are discretized using finite differencing methods and the model uses a modified Newton method to solve the discretized equations. Radiation losses are calculated using a detailed absorption/emission statistical narrow band model with wavenumbers ranging from 150 – 9300 cm^{-1}, coupled with a discrete-ordinates method with 20 ordinates. A detailed description of both methods is found in ref. [154]. Radiation from and reabsorption by CO, CO_2 and H_2O are included.

Conservation of species and energy are the same as ref. [154]. To improve numerical stability, conservation of mass was replaced by this version of the ideal-gas equation [14]:

$$\frac{\partial \rho}{\partial t} = -\frac{\rho}{T}\frac{\partial T}{\partial t} - \rho\overline{MW}\sum_{1}^{KK}\frac{1}{MW_k}\frac{\partial Y_k}{\partial t} \quad , \tag{4.5}$$

where ρ is density, t is time, T is temperature, MW is the mixture molar mass, MW_k is the molar mass of species k, Y is mass fraction, and KK is the total number of species. Pressure does not appear in Eq. (4.5) because it is assumed constant.

The computational domain extends from 0.32 cm at the burner surface to 100 cm at the outer boundary. The detailed boundary conditions for each equation are shown in ref. [154] unless noted otherwise. Burner heating has a second order effect on the results, but is non-negligible; thus, the inner boundary temperature was set to the experimentally measured burner temperature. There was no detectable change in species or temperature at the outer boundary, indicating that the size of the domain is sufficiently large.

The grid algorithm has been slightly modified. At the beginning of each time step, the center of the reaction zone was identified as the location of maximum temperature. The mesh was then adapted to assign the smallest grid spacing there. The gridding algorithm is such that the domain is divided into three zones: an inner zone, a reaction zone, and an outer zone. The inner zone follows the same algorithm as Ref. [154]. The reaction zone has 200 nodes with 0.001 cm grid spacing. The grid spacing in the outer zone increases by 5% for each grid cell moving outward. A total of 400 grid points was used, which was found to satisfy grid independence.

For this paper, a UCSD mechanism with 57 species and 259 reaction steps was used to simulate the flames [155]. Unlike previous studies [136-138,154], which simulate flames for 2.2 seconds (i.e., drop tower studies), flames in this investigation are simulated for up to 336 second. The UCSD mechanism keeps the number of species and reactions small for numerical tractability and uncertainty reduction introduced by reaction rates.

4.5 Results & Discussion

Based on experimental observations (e.g., drop tower and ISS tests) and Fig. 4.3, microgravity spherical diffusion flames grow monotonically with time. The increasing flame diameter and accumulation of product gases (primarily CO_2 and H_2O) result in an increase in radiative heat losses and decreased peak temperatures. Simultaneously, as the flame diameter increases, the rate of chemical heat release at the flame may decrease, owing to the decreasing diffusion rate to the flame. Eventually the flame may grow until radiative heat losses are comparable to the chemical heat release, resulting in radiative extinction [136]. The relative radius of a normal spherical diffusion flame in microgravity generally increases with increasing fuel flow rate, and with decreasing oxygen concentration in the ambient. These observations suggest that the key to

achieving long duration spherical diffusion flames in microgravity is to minimize radiative heat loss by using low fuel flow rates and/or relatively high ambient oxygen concentrations to yield small flames.

Table 4.1 summarizes the experimental conditions of the four long duration spherical flames examined herein. Each test has a unique reactant flow rate, stoichiometric mixture fraction (Z_{st}), and adiabatic flame temperature. Z_{st} is described in detail in refs. [124,125]. The quantity, X_{O2}, is the ambient oxygen concentration, whose uncertainty is estimated to be ±0.004. Each flame has a relatively low fuel flow rate to facilitate long experimental duration.

Table 4.1
Flame Design test points examined.

Flame	X_{O2} Ambient	X_{C2H4} Burner	$\dot{m}_{C2H4}$ [mg/s]	$\dot{m}_{N2}$ [mg/s]	T_{ad} [K]	Z_{st}
1	0.190	1.00	0.33	0.00	2270	0.058
2	0.391	0.288	0.52	1.30	2638	0.300
3	0.284	0.132	0.59	3.90	2183	0.409
4	0.377	0.132	0.78	5.20	2349	0.475

Figure 4.6 shows a representative image of each flame. All flames reported here contained no luminosity from soot after the ignition transient. Thus, radiation from soot is not considered in the numerical simulations. The flames are reasonably spherical, but not concentric with the porous sphere, and local flame quenching is apparent near the fuel supply tube. The image for flame 2 is from the ACME data camera, while those for flames 1, 3, and 4 are from the monochrome

intensified camera with a CH* filter, owing to the weak flame luminosity. The CH* images were false colored to simulate the color of the flame.

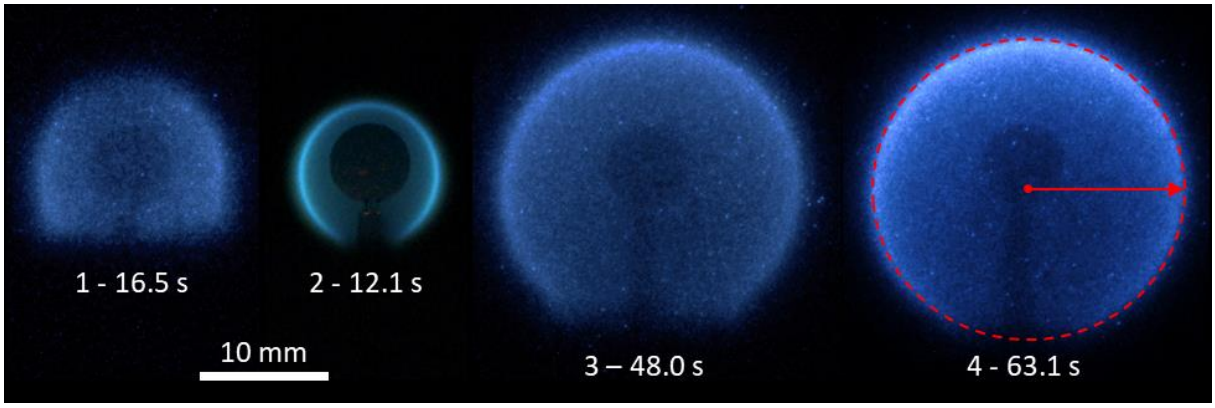

Fig. 4.6. Representative images of the flames in Table 4.1. The elapsed times are shown below the flames. The dashed red curve shown with flame 4 is the ellipse fit to measure flame radius.

Figure 4.7 shows experimental measurements and numerical predictions of flame radius. Measured burner temperatures are also shown. Owing to the low fuel flow rates and subsequently small flames, burner heating is significant. Fig. 4.7 shows that the rate of increase of the burner temperature is coupled to the size of the flame (i.e., smaller flames cause the burner to heat up more rapidly). However, burner heating is also a function of the fuel concentration (i.e., Z_{st}), inlet gas temperature, and burner material properties. While burner heating is significant, it has been shown that flame size is primarily a function of the reactant flow rate and the properties of the oxidizer side [139,144]. Because the effect of burner temperature on flame size is second order, the experimental burner temperature is used as a boundary condition in the numerical model. To illustrate the effect of burner heating, the dotted curve for flame 2 (the flame with the most significant burner heating) in Fig. 4.7 denotes the numerical prediction when the burner temperature is held constant at 300 K. When the burner temperature is held constant at 300 K, the flame size changes by less than 5%.

Owing to material limitations, the burner temperature was not allowed to exceed 773K (500 °C), a limit that was only met for flame 2. Flames 1 and 4 extinguished when the flow was terminated, and flame 3 extinguished radiatively. The burner temperature for flames 3 and 4 reached a peak and then decreased slowly, indicating that the flame is moving farther from the burner and/or cooling. The burner temperature for flames 1 and 2 is still increasing at the end of the test.

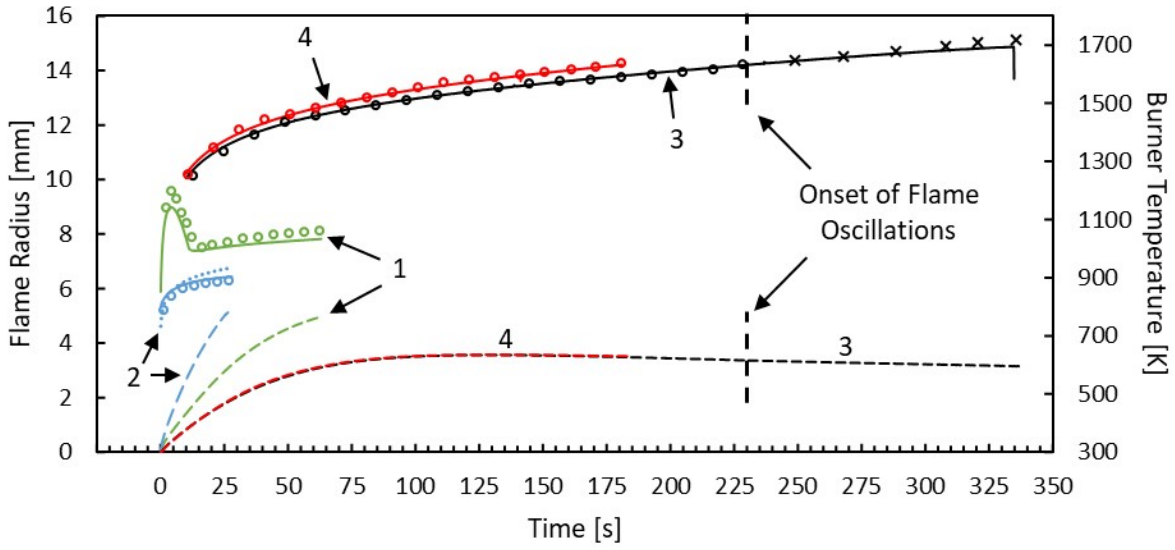

Fig. 4.7. Flame radius and burner temperature as functions of time. Open circles denote measured radii and solid lines denote predictions. Flame radii measured after the onset of the oscillations are denoted with the symbol, x. Dashed lines denote measured burner temperatures. The dotted line of flame 2 is the numerical prediction when the burner temperature is held constant at 300 K.

The numerical predictions of flame radius in Fig. 4.7 show excellent agreement with the experimental measurements. The first 10 s for flames 3 and 4 is excluded to better depict the behavior of the other flames. Flame 1 shows a peak flame radius at approximately 5 s. This flame was ignited at a fuel flow rate slightly higher than the test condition to facilitate ignition. The fuel flow rate was then ramped down to the test condition. The numerical model accounted for this and was able to accurately capture the behavior. The vertical dashed line shown for flame 3 indicates the onset of flame oscillations in which a portion of the flame continuously extinguishes and reforms, growing in magnitude with time until complete extinction. Flame radii measured after the

onset of the flame oscillations, between oscillations when the flame is whole, are indicated with an X.

Similar to microgravity droplet combustion [127-131,156], microgravity spherical diffusion flames exhibit quasi-steady behavior. A simple model for the steady flame size of a spherical diffusion flame in microgravity can be obtained by modifying the results of droplet combustion theory. The solution of steady-state flame radius from droplet theory is given in several textbooks, such as ref. [156], as

$$r_f/r_s = ln(1+B)/ln(1+f\,Y_{ox,\infty}/Y_{F,0}) \,, \tag{4.6}$$

where r_f and r_s are the flame and droplet radius, B is the Spalding B number, f is the stoichiometric mass fuel per mass oxidizer, $Y_{ox,\infty}$ is the oxidizer mass fraction in the ambient, and $Y_{F,0}$ is the fuel mass fraction inside the droplet. The burning rate, m_F, is

$$m_f/A_s = \rho D/r_s ln(1+B) \,, \tag{4.7}$$

where A_s is the droplet surface area, and ρ and D are the gas density and mass diffusivity.

This solution can be extended to the case of a gas-fed porous sphere. The fuel is defined as a hydrocarbon/N_2 mixture and the oxidizer is defined as an O_2/N_2 mixture such that $Y_{F,0} = Y_{ox,\infty} = 1$.

For a normal flame, f is redefined here as the stoichiometric mass of burner gas per mass of ambient gas. The quantity f is then replaced with the stoichiometric mixture fraction, Z_{st} , yielding

$$f = Z_{st}/(1-Z_{st}) \,. \tag{4.8}$$

Combining Eqs. (4.6-4.8) yields

$$d = m/2\pi\rho D\ln(1/(1-Z_{st})) \,, \tag{4.9}$$

where d is flame diameter and m is the burner mass flow rate.

This solution assumes constant ρD throughout the gas phase. For changes in pressure and temperature (not species), ρD follows from

$$\rho D = \rho_0 D_0 (T_{ch}/298\ K)^{1/2} \,, \tag{4.10}$$

where ρ_0 and D_0 are the gas density and diffusivity at 298 K and 1.01 bar and T_{ch} is the characteristic temperature for transport in the gas phase. Here it is assumed that ρ_0 is that of N_2 (1146 g/m^3) and D_0 is that of O_2 diffusing into N_2 (20.4 mm^2/s). It is further assumed that T_{ch} is the mean of 298 K and T_{ad}, the adiabatic flame temperature.

Table 4.2 shows the calculated quasi-steady flame radii for the flames in Table 4.1. The calculated flame radii accurately capture the trends observed in Fig. 4.7.

Table 4.2
Theoretical quasi-steady flame size.

Flame	Flame Radius [mm]
1	9.0
2	7.7
3	14.3
4	14.9

As observed in previous investigations, these spherical diffusion flames in microgravity grow monotonically with time, even in long duration. However, they do exhibit an asymptotic trend, with the rate of growth decreasing with time. Flame 3 asymptotes to conditions that lead to extinction. It is unclear if flames 1, 2, and 4 would asymptote to flammable conditions. The burner

temperature of flame 4 is decreasing, which could be due to the increasing flame radius and/or decreasing flame temperature, either of which may lead to extinction.

Figure 4.8 shows the experimentally measured OH* and unfiltered (230-700 nm) irradiance. All three PMTs (OH*, CH*, and unfiltered) show similar trends of flame irradiance with time, thus CH* emission is not included. If the flame is approaching extinction, the intensity measured by the PMT will decrease and go to zero when the flame extinguishes. The discontinuity in the unfiltered emission for flames 1, 3, and 4 is due to luminosity from the TFP fibers entering the flames. The fiber insertion in flame 1 is less apparent owing to the simultaneous flowrate change. The irradiance from flame 3 gradually decreases until it enters the oscillatory mode. The oscillations grow in magnitude with time until the flame extinguishes, and the irradiance then goes to zero. The emissions for flame 4 show an asymptotic trend, and for flames 1 and 2 appear steady,

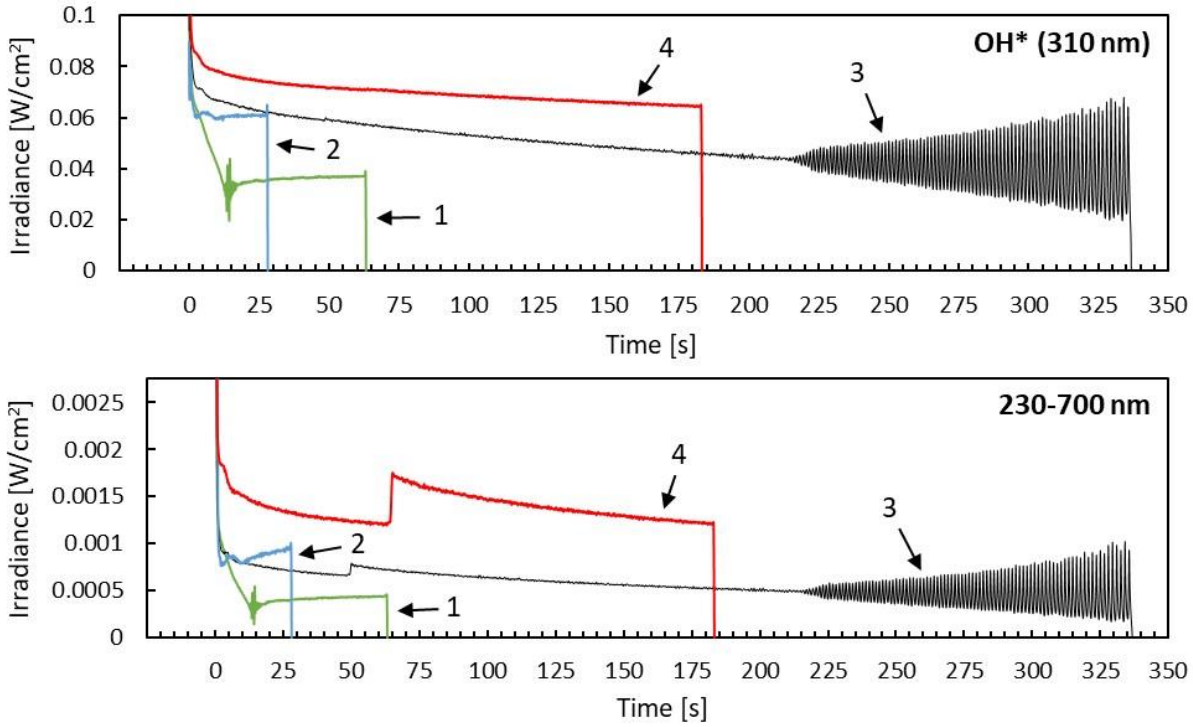

Fig. 4.8. Experimental measurements of irradiance at 310 nm (**top**) and 230-700 nm (**bottom**) as a function of time.

or slightly increasing. The slight increase in irradiance is likely due to the increasing flame radius, increasing flame temperature, and/or the rapidly increasing burner temperature.

The oscillatory mode of flame 3 is illustrated in Fig. 4.9. Figure 4.9a show the progression of one full oscillation as a portion of the flame extinguishes and then reforms. The oscillations continue to grow until complete extinction, as seen in Fig. 4.9b. The OH* irradiance in Fig. 4.9b is magnified in Fig. 4.9c to better illustrate the dynamics of one full oscillation. The exact time interval for the photos of Fig. 4.9a is denoted with red vertical dashed lines in Fig. 4.9c. A similar oscillatory phenomenon has been observed in microgravity candle flames [132] and droplet flames [127,128,157]. The oscillations seen herein begin near the fuel supply tube (i.e., region where the

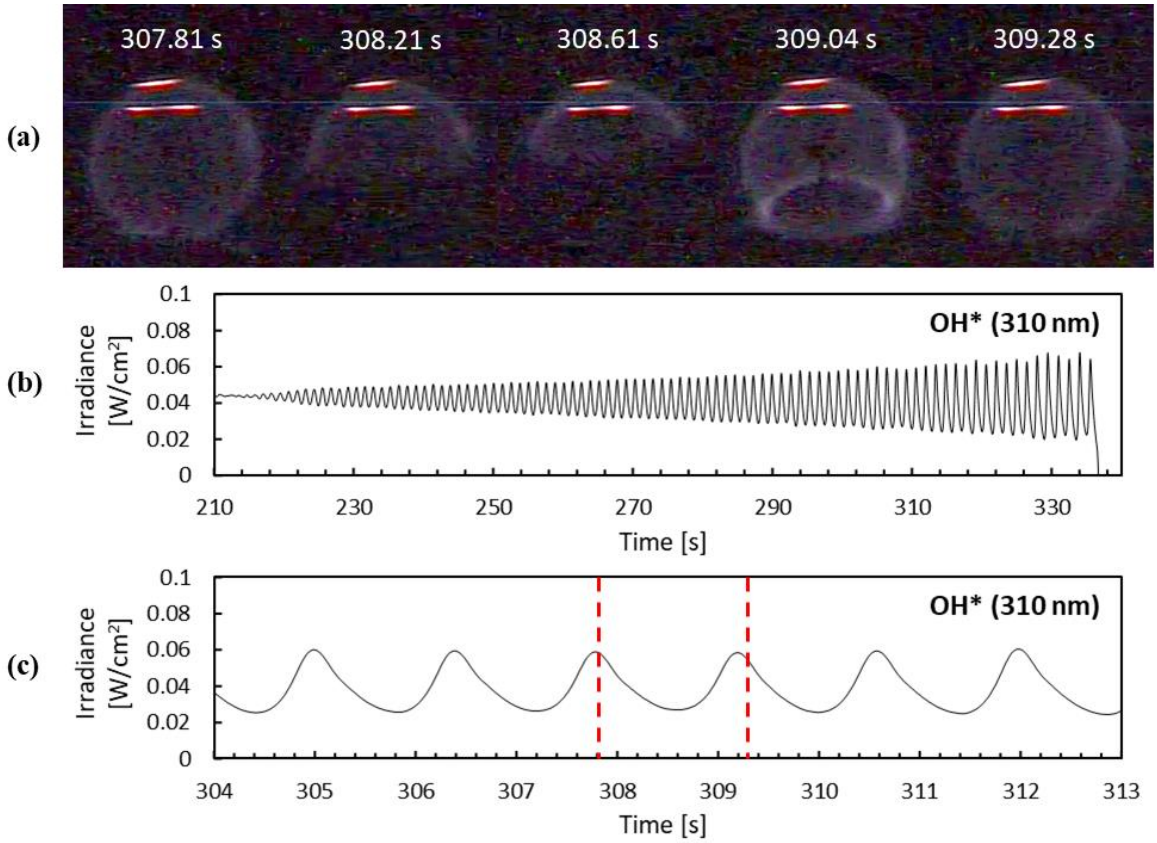

Fig. 4.9. A progression of photos from the operations video for flame 3 showing the oscillatory mode in which a portion of the flame extinguishes and reforms (**a**), and PMT measurements of OH* irradiance (**b** and **c**). The elapsed time for each image is labeled above the respective image. The magnitude of the flame oscillations grows continuously until total extinction.

flame is quenched) and progress towards the opposite side of the porous sphere (i.e., the region of highest reactivity and temperature). The region opposite of the fuel supply tube is also the thinnest and brightest part of the flame (see Fig. 4.6), suggesting that this region has the lowest radiative losses. The oscillatory mode is likely induced by the quenched region at the burner tube, and the growth in the oscillations, and ultimately extinction, is due to the decreasing flame temperature as the flame grows and radiation heat loss increases. The oscillatory mode referenced herein will be further addressed in a future manuscript.

Figure 4.10 shows the simulated and experimentally measured peak gas temperatures (i.e., flame temperatures) as functions of time. There is no TFP data for flame 2. The experimental peak temperatures show good agreement with the simulated peak temperatures, particularly the trends with time. For flame 1, the experimental flame temperature measurements are roughly 150 K lower than the numerical predictions. The cause of this is under investigation. Uncertainty could be associated with the change in flow rate during this test. It should be noted that this discrepancy

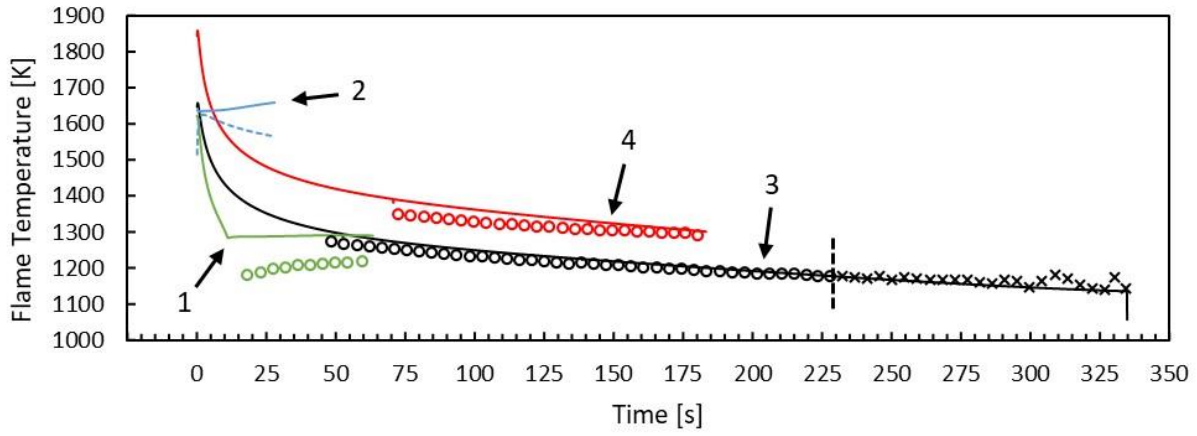

Fig. 4.10. Numerically predicted flame temperature (solid lines) and measured flame temperature obtained from TFP (symbols) as functions of time. Open circles denote stable flames, and the x symbols denote oscillating flames (the fiber is not in the region of flame instability, see Fig. 4.9). The dashed line for flame 2 is the numerically predicted flame temperature when the burner temperature is held constant at 300 K.

would not have a large effect on flame size, because flame size is primarily a function of reactant flow rate and the properties of the oxidizer side [139, 144,158].

Experimental flame temperature measurements are taken for flame 3, even during the oscillatory phenomenon, due to the thin-filament fiber always being in a location where the flame exists, as seen in Fig. 4.9a. The measured and simulated flame temperatures show that the flame temperature asymptotes until the flame extinguishes at a measured temperature of 1140 K after 337 s, and a simulated temperature of 1135 K after 335 s. These extinction temperatures are similar to the extinction temperature of ethylene seen in other spherical flame investigations (approximately 1150 K) [136]. The flame temperature of flame 4 is also temporally asymptotic, but it is unclear if the flame would extinguish at long times. The flame temperatures for flames 1 and 2 are relatively constant, or increasing slightly, after the ignition transient. This increase is due to the rapidly increasing temperature of the burner and the convection of heat to the flame. This assumption has been verified by running the numerical simulation assuming a constant burner temperature of 300 K. The result is denoted by the dashed line for flame 2 in Fig. 4.10. When the surface of the burner is maintained at 300 K, the flame temperature for flames 1 and 2 decreases asymptotically with time, similar to flames 3 and 4.

4.6 Conclusions

Long duration gaseous spherical microgravity diffusion flames aboard the International Space Station (ISS) were examined. Experimental results were compared with simulations from a transient numerical model. The following observations were made:

1) Long duration burner-supported microgravity spherical diffusion flames grow monotonically with time. The rate of growth decreases with time as the flames asymptotically approach a condition that may never be reached, owing to extinction.
2) Burner heating is intrinsically coupled to flame radius for small flames near the burner but has a second order effect on flame size. Significant burner heating in very small flames can cause the flame temperature to increase with time by convection of heat to the flame, but the flame continues to grow with time. After reaching a peak, the burner temperature may decrease with time owing to the flame moving farther from the burner and/or decreasing flame temperature.
3) As flames approach extinction, they may enter an unstable oscillatory mode in which they partially extinguish and reform. The oscillations grow in magnitude with time until complete flame extinction. The oscillations begin at the region the quenched flame near the fuel supply tube and progress towards the region of highest temperature (i.e., the region opposite the fuel supply tube).
4) For modest fuel flow rates (modest flame radii), the flame temperature typically decreases with time due to increasing flame radius and the subsequent increase in radiative heat loss. In such flames, the flame temperature asymptotically approaches a temperature that may or may not lead to extinction. For low fuel flow rates (small flames) the flame temperature remains relatively constant, or increases, due to heat convected to the flame from the burner.
5) Measurements of radiant emissions in the visible and UV show that flames with decreasing peak gas temperature exhibit asymptotically decreasing irradiance. Flames with increasing or nearly constant peak gas temperature exhibit increasing or constant irradiance.

This effort to study burner stabilized spherical diffusion flames on the ISS has revealed the basic characteristic of these flames. Based on the results herein, the general question whether there is a steady-state condition for burner-supported spherical diffusion flames remains unanswered. Future studies are being conducted to further understand the fundamental characteristics of long-duration microgravity spherical diffusion flames (e.g., radiative extinction, the existence of a steady-state spherical diffusion flame, soot formation, and the impact of stoichiometric mixture fraction). An investigation of inverse microgravity spherical flames (i.e., where oxidizer issues from the burner into an environment of fuel) will also be conducted aboard the ISS.

Chapter 5: Critical temperature and reactant mass flux for radiative extinction of ethylene spherical diffusion flames at 1 bar

5.1 Introduction

Flame extinction is of fundamental importance in topics such as fire safety (terrestrial and extra-terrestrial), large-scale wildfires, and quenching near solid boundaries. Extinction can also have negative impacts, such as loss of power in engines and the formation of pollutants that negatively affect human health. Because of its fundamental and practical importance, flame extinction has been studied extensively in diffusion flames, owing to the many practical combustion systems that they are used in.

The two primary modes of extinction are kinetic extinction and radiative extinction. Kinetic extinction occurs at small Damköhler number, Da, when residence time (i.e., the time for the reactant to pass through the reaction zone) is small compared to the reaction time. Kinetic extinction can easily be observed experimentally in counter-flow diffusion flames when the strain rate is increased to the point of extinction [136].

Radiative extinction, which is particularly important for spacecraft fire safety, was first suggested by T'ien [159] from his numerical investigation, and later theoretically predicted by Chao [140]. Radiative extinction occurs at large Da, for example, at very low strain rate and large flame size. Due to its size and low strain rate, the flame experiences excessive radiative heat loss relative to heat release, which decreases the flame temperature until the flame extinguishes.

Radiative extinction is difficult to observe experimentally in normal gravity because buoyancy accelerates the flow field (i.e., increases strain), decreasing residence time [136]. To avoid buoyancy, radiative extinction has been studied in microgravity using spherical diffusion flames. The two most common spherical diffusion flames are droplet flames [160-163], and burner-

stabilized gaseous spherical diffusion flames [54,133,135-139,141-144,151,158]. The spherical geometry of both flames provides a near one-dimensional system that is ideal for modeling.

For droplet flames, however, the rate of fuel supply cannot be specified, as the vaporization rate (i.e., the fuel flow rate) is an eigenvalue of the droplet evaporation problem. Additionally, the fuel concentration cannot be easily controlled, and the direction of convection relative to the flame cannot be varied (it is always from the fuel to the oxidizer). Gaseous burner-supported spherical diffusion flames, on the other hand, offer a controllable reactant flow rate, the ability to control the concentration of the fuel supply, and the ability to operate such that the direction of convection across the flame can be either from fuel to oxidizer or oxidizer to fuel, making them ideal for fundamental studies of microgravity spherical diffusion flames.

Radiative extinction of gaseous burner-supported microgravity spherical diffusion flames has been well studied theoretically [54,133,136-139,141-144,151,15], and to a lesser extent, experimentally [54,133,135-137]. Historically, experiments have been limited by experimental conditions in terrestrial drop towers, which allow for only 2-5 seconds of microgravity. During this short time, the ignition event can still have a significant influence on the flame. Chernovsky et al. [135] and Tse et al. [133] were able to predict radiative extinction numerically but could not achieve it experimentally. Santa et al. [136] were able to achieve radiative extinction experimentally, but only with a heavily diluted ambient, and they concluded that radiative extinction occurs at a nearly constant radiative loss fraction of about 0.7.

Tang et al. developed a numerical model to study the experimental results of ref. [135]. They concluded that extinction occurs at a constant temperature of approximately 1130 K, that the local flame radiation controls flame temperature, not the total volumetric radiation, and that the

properties of the oxidizer have a large effect on flame size [138,139]. Mills et al. [144,158] developed a steady-state analytical model and identified a maximum flow rate, above which a spherical diffusion flame cannot exist due to radiative losses, and a minimum flow rate, below which a spherical diffusion flame cannot exist due to short residence times. Mills et al. [8] also concluded that the Lewis number of the oxidizer has a large effect on flame location in a normal flame configuration. Rodenhurst et al. [141] studied spherical diffusion flames using multi-scale activation energy asymptotics and found that flames with the same fuel consumption rate extinguish at the same Da. Nayagam et al. [143] provided a simple scaling analysis of radiative extinction in spherical diffusion flames, assuming a constant loss fraction at extinction, that agreed well with the experimental results in ref. [136].

Overall, these studies have shown that microgravity spherical diffusion flames grow until they extinguish, or until the experiment ends (i.e., the flow is stopped). Product gases (primarily CO_2 and H_2O) radiate heat from the flame, reducing the flame temperature. If there is sufficient time in the microgravity experiment, the flame may grow large enough that radiation losses are sufficiently large that the flame temperature drops to the critical temperature for extinction [54,136,137]. The flame then extinguishes via radiative extinction.

Unfortunately, due to the experimental time constraints of terrestrial microgravity research, the radiative extinction of spherical diffusion flames is still not well understood. This study aims to investigate radiative extinction of normal and inverse ethylene microgravity spherical diffusion flames at atmospheric pressure by conducting experiments aboard the International Space Station (ISS). Experimentation aboard the ISS allows for ample time to achieve radiative extinction for a wide range of flame conditions. Experiments are simulated with a transient numerical model. This investigation was conducted under Flame Design, which is one of six

experiments under the NASA project titled Advanced Combustion via Microgravity Experiments (ACME).

5.2 Methods

5.2.1 Experimental

Experiments are conducted aboard the ISS in the Combustion Integrated Rack (CIR). Figure 5.1 illustrates the experimental configuration and the resulting spherical diffusion flame. The burner is a 6.4 mm diameter stainless steel porous sphere. Reactant gas is supplied via a 1.17/1.5 mm (inside/outside diameter) tube, which is inside a larger 1.6/1.83 mm (inside/outside diameter) support tube. Quiescent conditions at an ambient temperature of 295 K are maintained in a 105 L chamber with a free volume of 83.4 L. The pressure is 1 bar ± 5%.

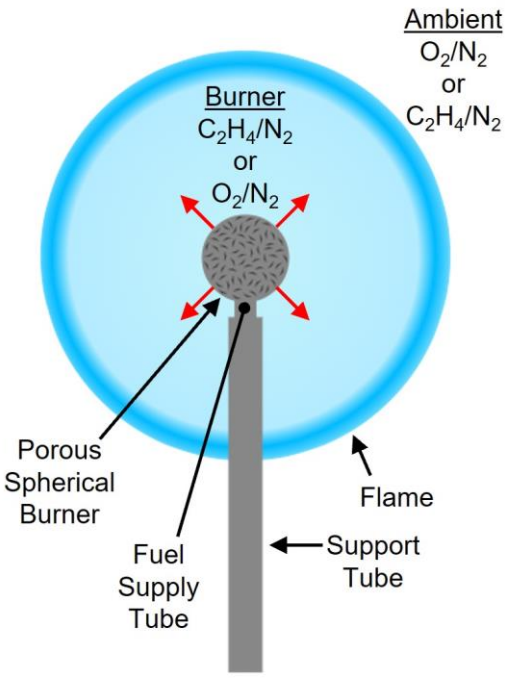

Fig. 5.1. Illustration of the experimental configuration and a microgravity spherical diffusion flame.

The fuel is ethylene (C_2H_4), the oxidizer is oxygen (O_2), and the diluent for both is nitrogen (N_2). For normal flames, pure or diluted ethylene can be introduced into the sphere and the ambient oxygen concentration is limited to 40% or less, owing to safety concerns aboard the ISS. For inverse flames, 85% O_2 or less can be supplied to the burner and the ambient fuel concentration is limited to 27% C_2H_4 at atmospheric pressure, owing to fuel bottle size. Figure 5.2 shows photographs of representative normal and inverse spherical flames observed aboard the ISS.

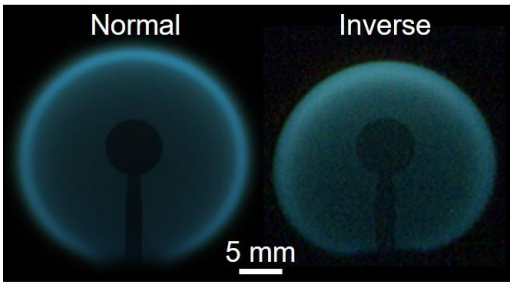

Fig. 5.2. Representative photographs of a normal (X_{O2}=0.3 and X_{C2H4}=0.17) and inverse (X_{O2}=0.29 and X_{C2H4}=0.17) spherical flame at a fuel consumption rate of about 0.8 mg/s taken aboard the ISS.

The burner gases are supplied using mass flow controllers with an estimated uncertainty of ± 5%. Ignition is achieved using a hot wire igniter that retracts after ignition.

At the beginning of each test period, the chamber is filled to the desired ambient reactant concentration and pressure. The concentration of the ambient reactant decreases marginally over the test day, as the flames consume the reactants. A mixing fan is used between experiments to ensure a homogenous and quiescent environment for the next test.

Flame radius as a function of time is measured using still frames from the ACME operations camera, a 0.44-megapixel CCD color video camera that records at 30 fps. For each flame image, an ellipse is fit at the location where the intensity of the blue color channel is midway between its peak and ambient intensity (i.e., approximately the region of stoichiometry [146]), as in [54]. The flame diameter is taken as the axis of the ellipse perpendicular to the fuel support tube. The flame

is typically quenched in the vicinity of the burner support tube, making it difficult to interpret the location of the flame sheet in that region. Uncertainty in measured flame size is estimated to be ± 4%.

Burner surface temperature is measured using a sheathed 0.25 mm diameter type-K thermocouple embedded in the burner surface.

5.2.2 Numerical model

The numerical simulations are performed using the SphDiff code of refs. [54,136,137,151,152], which is a modification of Sandia PREMIX [153]. Finite differencing is used to discretize the governing equations, and the subsequent equations are solved using a modified Newtonian method. The equations for conservation of species, energy, and mass are the same as in ref. [54]. Radiation heat loss from CO, CO_2, and H_2O is calculated using a detailed absorption/emission statistical narrow band model with wavenumbers ranging from 150 to 9300 cm^{-1}, coupled with a discrete-ordinates method with 20 ordinates [154]. Radiation from soot is not considered in these simulations, as luminous soot does not form in these flames after the ignition transient, owing to the large radiative loss fraction from radiating product gases and resulting rapid decrease in flame temperature.

The computational domain spans from the burner surface (0.32 cm) to 100 cm. The boundary conditions are described in detail in ref. [154]. As shown in ref. [54], the effect of burner heating is second order, but non-negligible, thus the temperature at the inner boundary is set to the experimentally measured burner temperature, as in [54]. The size of the domain is sufficiently large that there is no change in species or temperature at the outer boundary. An adaptive grid algorithm is used, as in [54].

The UCSD mechanism with 57 species and 270 reactions is used to simulate the chemical kinetics of the flames [155].

5.3 Results & Discussion

During each test, the burner reactant flow rate is held constant, and the chamber pressure is 1 bar ± 5%. The numerical model is able to simulate flame size within 5% of the measured values. The model is also on average able to simulate burn time within 20% of the experiments. Uncertainty in the burn time is likely due to i) experimental flame oscillations prior to extinction, which are not captured with the 1D model [54], ii) the flame being slightly offset from the burner (i.e., the flame is not perfectly concentric), and iii) uncertainties in the kinetics.

After ignition, the flames grow monotonically. The simulated radiation heat loss rate, Q_R, increases with time due to the production of radiating product gases and the growth of the flame. The total volumetric heat release rate, Q_C, remains relatively constant. The simulated peak temperature (i.e., flame temperature) decreases with time due to radiation. Numerically, it is observed that each of the 56 flames extinguishes at an extinction temperature of 1130 K ± 4 K, consistent with [54,136,139].

5.3.1 Normal flames

From the experiments conducted aboard the ISS, 49 normal spherical flames that radiatively extinguished are investigated. The operating conditions for these flames span the following ranges:

1. Ambient oxygen concentration, X_{O2}: 0.20 – 0.38
2. Burner fuel concentration, X_{C2H4}: 0.13 – 1.0

3. Total mass flow rate, $\dot{m}_{total}$: 0.6 – 12.2 mg/s
4. Adiabatic flame temperature, T_{ad}: 2000 – 2800 K

Figure 5.3 shows simulated radiative loss fraction, X_R (i.e., Q_R divided by Q_C), as a function of time for 20 flames that are representative of the wide range of experimental conditions considered. The quantities Q_R and Q_C are defined in detail in [136,139]. Experimental radiation measurements are not available, owing to the signal of the radiometer aboard the ISS being saturated.

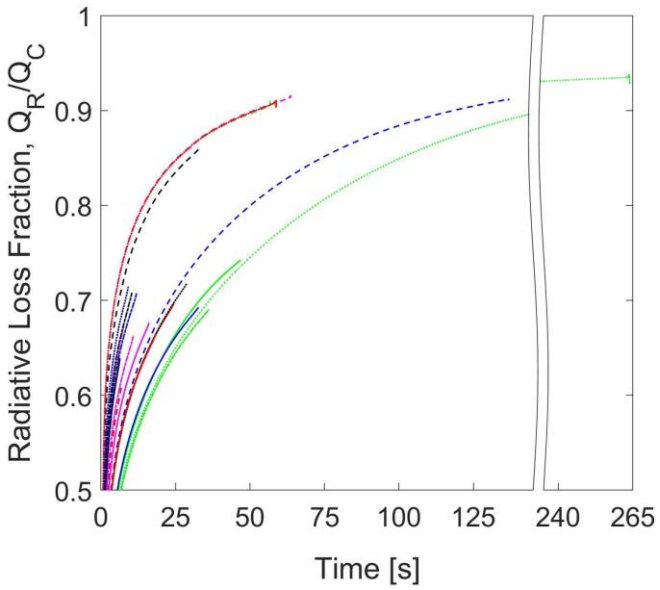

Fig. 5.3. Simulated radiative loss fraction (total volumetric rate of radiation heat loss/chemical heat release rate) as a function of time.

Figure 5.3 shows that the radiative loss fraction increases with time. This monotonic increase in radiative loss fraction is a result of the increasing Q_R since Q_C is nearly constant. The radiation heat loss rate increases, despite the decreasing temperature, because as the flame grows and continues to produce radiating product gases, the flame emissivity increases due to the increasing path length and partial pressure of radiating products.

The 49 normal spherical flames investigated herein extinguished at radiative loss fractions ranging from 0.61 to 0.93. Historically, some researchers have assumed that the flame temperature

correlates well with total volumetric radiation, thus a critical radiative loss fraction (circa 0.7) has been used as an indicator of radiative extinction [136,143]. Figure 5.3 shows that this may be true for flames that extinguish in short times (i.e., drop tower timescales) when the total amount of radiation is low, but the flames that last for longer durations can extinguish at much larger radiative loss fractions. For these long duration flames, the radiating volume extends far from the flame, such that the total volumetric radiation is no longer a good indicator of flame temperature. The flame temperature is instead dictated by radiation from a thinner zone near the flame, as suggested by Tang et al. [139], as opposed to radiation from products that are far away from the flame.

To obtain a more comprehensive indicator of extinction, it is recognized that, for normal flames, for a given mass flow rate of fuel, when the flame expands, the flux of the fuel-based mass (i.e., H and C) across the flame decreases. This fuel-based mass flux, J_F, can be defined as

$$J_F = \dot{m}_F / A_{flame} \,, \tag{5.1}$$

where $\dot{m}_F$ is the mass flow rate of fuel (i.e., ethylene) out of the burner and A_{flame} is the flame surface area at the location of peak (flame) temperature. Figure 5.4 shows, for the same 20 flames seen in Fig. 5.3, the simulated results for flame temperature as a function of the fuel-based mass flux, J_{C2H4}. Despite the broad range of initial conditions, and considering each of the 49 flames that radiatively extinguished aboard the ISS, the numerical model shows that in addition to a constant extinction temperature, all normal ethylene spherical diffusion flames extinguish at a constant J_{C2H4} of 0.2 ± 0.01 g/m^2-s.

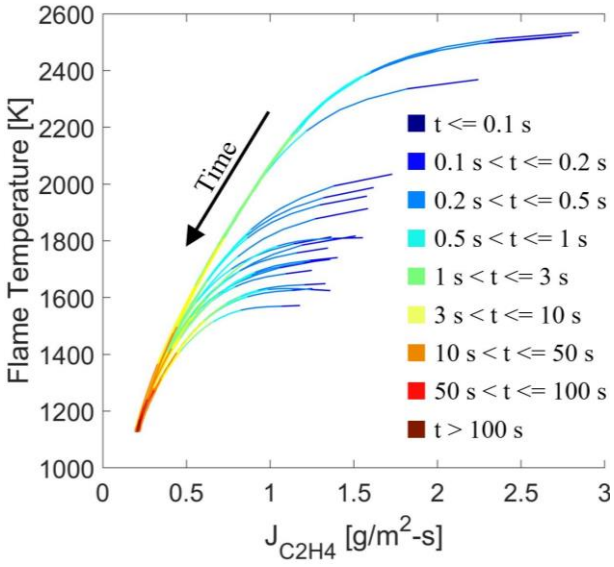

Fig. 5.4. Simulated flame temperature as a function of fuel-based mass flux at the location of peak temperature.

With J_{C2H4} being constant at extinction, one can rearrange Eq. 5.1 and solve for the flame size at extinction for normal ethylene spherical flames as a function of fuel mass flow rate,

$$r_{ext} = sqrt(\dot{m}_{C2H4}/4\pi J_{C2H4}) \,, \tag{5.2}$$

where r_{ext} is the flame radius at extinction for normal flames.

The fuel-based mass flux, J_F, represents the rate of transport of reactant across the flame, which is indicative of the scalar dissipation rate, or flow time. This can also be related to Da (i.e., decreasing mass flux indicates increasing Da.) However, the hydrocarbon-based mass flux provides a global parameter that allows one to calculate the flame size at extinction directly from the initial conditions.

Figure 5.5 shows the calculated r_{ext} as a function of $\dot{m}_{C2H4}$ calculated from Eq. 5.2 where J_{C2H4} is 0.2 g/m^2-s. Figure 5.5 also shows the measured extinction radii for each the 49 flames considered.

The experimental extinction radius is measured for each experiment using the last camera frame when the flame is whole, as in [54]. Flames near extinction experience an oscillatory mode, starting at the support tube, where large portions of the flame extinguish and then reform, but these oscillations do not appear to significantly affect the size of the flame. Also shown in Fig. 5.5 are the predicted extinction radii calculated using the theory of Nayagam et al. [143] with an empirical constant (i.e., radiative loss fraction) of 0.8.

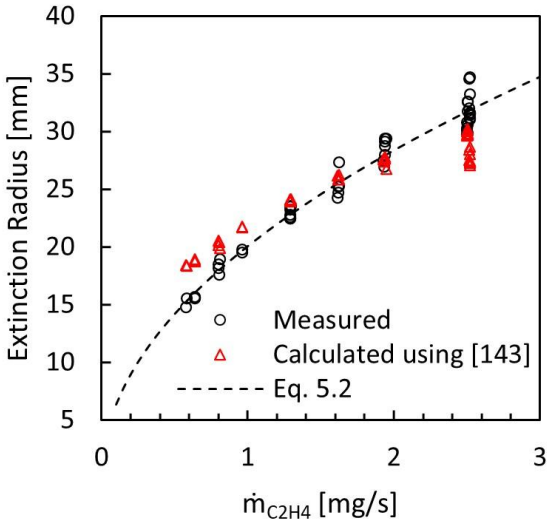

Fig. 5.5. Flame radius at extinction as a function of fuel mass flow rate measured using 49 normal flames observed aboard the ISS (open circles), calculated using Nayagam et al. [143] with an empirical constant of 0.8 (open triangles), and calculated using Eq. 5.2 with a fuel mass flux of 0.2 g/m^2-s (dashed line).

With the experimentally obtained radiative extinction data, one can use Eq. 5.2 to solve for the experimental J_{C2H4} at extinction knowing r_{ext} and $\dot{m}_{C2H4}$. The average measured value of J_{C2H4} for the 49 ethylene flames considered is 0.2 g/m^2-s ± 0.014 g/m^2-s. The uncertainty in the measured fuel-based mass flux at extinction is owing to uncertainty in the mass flow controllers and in the measured flame radii. The curve calculated using Eq. 5.2 fits the measured data with an R^2 value of 0.95. The predicted extinction radii using the theory of Nayagam et al. show reasonable agreement, but deviate from the long duration experimental data, presumably due to the assumption that the radiative loss fraction is constant at extinction [143].

5.3.2 Flame growth

An improved understanding of spherical diffusion flame growth will help explain why these flames extinguish at a constant mass flux. It is helpful to first isolate the intrinsic growth of a diffusion limited system as it approaches steady state [164]. This can be done by simulating a spherical flame with and without radiation heat loss.

Figure 5.6 shows the simulated flame radius and flame temperature as a function of time for 1.5 mg/s of pure ethylene issuing into air with and without radiation. The flame without radiation reaches a constant temperature very quickly, but the flame continues to grow as the diffusion-controlled system grows towards steady state [164]. When radiation is included, the temperature drops quickly, resulting in flame growth that is much more rapid than that without radiation, ultimately leading to the critical point for radiative extinction.

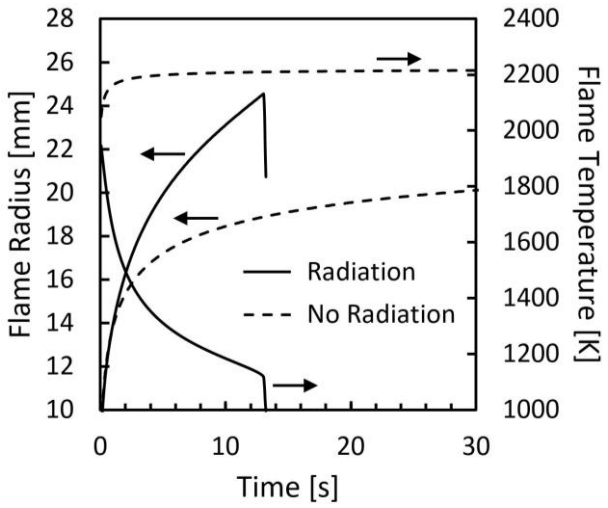

Fig. 5.6. Simulated flame radius (primary axis) and flame temperature (secondary axis) as a function of time for a 100% ethylene normal spherical diffusion flame with a fuel mass flow rate of 1.5 mg/s burning in 21% O_2 with radiation heat loss (solid lines) and without radiation heat loss (dashed lines).

During the early stage of growth, just after ignition, the spatial distributions are developing rapidly, and at this stage it is the intrinsic growth of the diffusive system that is important. Thus, the two curves overlap for the first two seconds. At longer times, the radiation-induced growth dominates, causing the two curves to diverge.

The effect of radiation, and the subsequently decreasing temperature, on flame size can be realized by evaluating the equation for the steady flame radius of a normal spherical diffusion flame derived by Mills et al [158]. By rearranging this equation, it can be shown that for a given set of initial conditions (i.e., flow rate and concentration), the size of a normal spherical diffusion flame is primarily dependent on the transport properties of the oxidizer, or ρD_O:

$$r_f = \dot{m}_{total}/[4\pi\rho D_O ln(1+\nu^{-1}X_O)] \ , \tag{5.3}$$

where r_f is flame radius, ρ is density, D is diffusivity, ν is the stoichiometric coefficient of the oxidizer, X is mole fraction (i.e., concentration), and the subscript O denotes the oxidizer. The conclusion that flame size is dependent upon ρD of the oxidizer for a normal flame is reasonable, because for the normal spherical flame configuration, the diffusive flux of oxidizer to the flame is the controlling mechanism of transport for the ambient. In contrast, convection from the burner dominates transport of fuel to the flame.

It is also important to recognize that ρD has a temperature dependence of $T^{1/2}$. The dependence of flame radius on ρD, coupled with the dependence of ρD on temperature, suggests that when the flame temperature decreases due to radiation, ρD also decreases. This subsequently decreases the diffusive flux of ambient reactant to the flame, causing the flame to propagate outward (i.e., the flame increases in size) to maintain stoichiometry. Thus, this mechanism, which we refer to as radiation-induced growth, can ultimately lead to radiative extinction (cf. Fig. 5.6).

Because radiation-induced growth dominates after the ignition transient, it is reasonable to assume that for a constant flow rate, after the ignition transient, the size of the spherical diffusion flame is largely dependent on temperature. Realizing this, it is expected that if these flames extinguish at a constant temperature, they should also extinguish at a constant reactant flux to the flame (since flux is dependent on flame size for a given fuel mass flow rate). Therefore, for a normal flame configuration, $\dot{m}_F$ provides a convenient way to estimate this extinction flux.

Considering this, the following path to radiative extinction is proposed: After the flame is established, the combustion products radiate heat from the flame, decreasing the flame temperature. Owing to the reduction in temperature, the transport properties of the ambient reactant decrease, and this decrease, along with the depletion of ambient reactant, causes the flux of ambient reactant to the flame to decrease. The flame grows outward to where the fluxes of fuel and oxidizer are in stoichiometric proportions. For flames that radiatively extinguish, this process continues until the flame reaches the critical extinction point.

5.3.3 Inverse flames

Radiative extinction of inverse spherical diffusion flames (i.e., oxidizer flowing from the burner into an ambient fuel) is also investigated. A total of seven inverse flames were observed to radiatively extinguish, and these are investigated experimentally and numerically. These inverse flames span the range of conditions below:

1. Ambient fuel concentration, X_{C2H4}: 0.08 – 0.12
2. Burner oxygen concentration, X_{O2}: 0.4 – 0.85
3. Total mass flow rate, $\dot{m}_{total}$: 2.3 – 11.3 mg/s
4. Adiabatic flame temperature, T_{ad}: 2080 – 2590 K

The critical extinction temperature of approximately 1130 K remains the same for inverse spherical diffusion flames, owing to the chemical kinetics. Following the logic outlined above for normal flames, the critical reactant mass flux at extinction for inverse flames can now be determined by using the mass flow rate of oxygen and accounting for stoichiometry. The oxygen-based mass flux at extinction, J_{O2}, is estimated by multiplying the fuel-based mass flux by the mass-weighted stoichiometric coefficient, σ, for the combustion of ethylene and oxygen (i.e., $J_{O2} = \sigma J_{C2H4}$, where $\sigma = 3.42$). Thus, the flame size (i.e., location of peak temperature) of an inverse flame at extinction for any oxygen mass flow rate can be estimated using,

$$r_{ext,inverse} = sqrt(\dot{m}_{O2}/4\pi J_{O2}) \; . \tag{5.4}$$

Using the ethylene-based mass flux at extinction (0.2 g/m^2-s), the oxygen-based mass flux at extinction is estimated to be 0.68 g/m^2-s.

Figure 5.7 shows flame extinction radius as a function of oxygen mass flow rate using Eq. 5.4. It also shows the simulated and measured extinction radii for the seven inverse flames that radiatively extinguished aboard the ISS. The simulated and experimental data agree well with Eq. 5.4. Moreover, the experimental data fit the curve calculated using Eq. 5.4 with an R^2 value of 0.97.

The above findings provide a simple method to estimate the size of a normal or inverse ethylene spherical diffusion flame at atmospheric pressure at radiative extinction. Further research must be conducted to elucidate the critical point for radiative extinction in other fuels, and the effect of pressure.

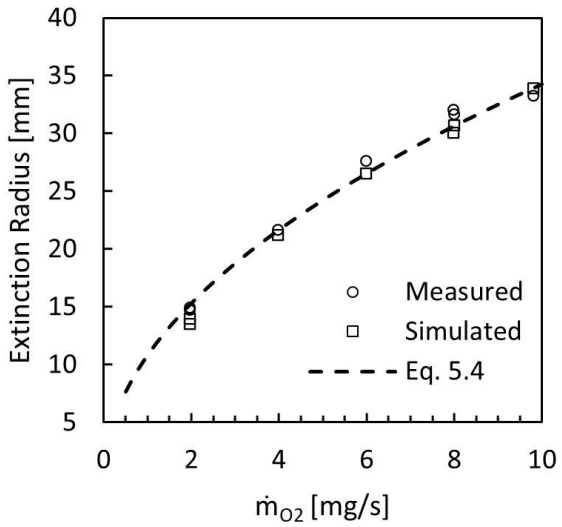

Fig. 5.7. Flame radius at extinction as a function of oxygen mass flow rate measured (open circles) and simulated (open squares) from 7 inverse flames that radiatively extinguished aboard the ISS and calculated using Eq. 5.4 with an oxygen mass flux of 0.68 g/m^2-s (dashed line).

5.4 Conclusions

Radiative extinction of microgravity spherical diffusion flames was investigated using experiments conducted aboard the ISS and a transient numerical model. The following conclusions were made:

1) All of the atmospheric-pressure microgravity spherical diffusion flames that radiatively extinguish, did so at the same extinction temperature and the same reactant-based mass flux at the flame. For all atmospheric-pressure ethylene spherical diffusion flames, the critical extinction temperature is 1130 K, and the critical reactant-based mass flux is found to be approximately 0.2 g/m^2-s for ethylene and 0.68 g/m^2-s for oxygen. The size of an ethylene spherical flame at extinction can be conveniently estimated using the burner reactant mass flow rate.
2) At a constant burner reactant mass flow rate, microgravity spherical diffusion flames grow with time, owing to the intrinsic development of a diffusion-limited system and, more

importantly, radiation-induced growth, which is a consequence of the temperature dependence of transport properties. After the flame is established, this growth can lead to radiative extinction via the following diminishing feedback loop: i) the combustion products radiate heat from the flame, and this decreases the flame temperature, ii) the decrease in flame temperature causes the transport properties of the ambient reactant to decrease, iii) this causes the flux of ambient reactant to the flame to decrease, and iv) this causes the flame to grow to a new location where the fluxes of fuel and oxidizer are once again in stoichiometric proportions. The process repeats itself and, eventually, if the flame reaches the critical extinction temperature and flux, it will extinguish.

This effort to study radiative extinction in microgravity spherical diffusion flames has elucidated the fundamentals of radiation extinction in spherical diffusion flames. Further research must be conducted to elucidate the chemical kinetics that lead to flame extinction at the critical extinction temperature and the effect of pressure on extinction. Furthermore, other fuels should be investigated to elucidate if this critical point for radiative extinction is universal.

Chapter 6: On the existence of steady-state spherical diffusion flames in the presence of radiation heat loss

6.1 Introduction

The existence of a steady-state gaseous microgravity spherical diffusion flame is an important fundamental question and has implications for spacecraft fire safety. Steady-state spherical diffusion flames are often theorized [133,144,158] but have yet to be observed experimentally. Prior to the International Space Station (ISS) gaseous spherical diffusion flames had not been investigated for sufficiently long duration to experimentally explore this possibility. Furthermore, while an approximate analytical transient solution exists for spherical diffusion flames without radiation [145], no such solution has been found when radiation losses are included.

Semi-spherical candle flames have been investigated on the Space Shuttle and the Mir Orbiting Station, and the candle flames burned anywhere from 40 s to 45 min, depending on ambient oxygen concentration and wick size [132]. Candle flames, however, have an uncontrollable flow rate, and a spherically symmetric flow field only at the tip of the wick. Because a steady-state solution does not exist for cylindrical flow (as induced over the length of the wick), the resulting flame is a hemispherical cap where oxygen is free to diffusive into the fuel rich region of the flame, possible creating a partial premixture. Thus, these flames cannot be considered purely spherical diffusion flames.

Past microgravity burner-supported gaseous spherical diffusion flame experiments have been limited by terrestrial experimental conditions that allow for only a few seconds of microgravity [133,135-137]. NASA's Zero Gravity Research Facility can provide 5.18 s of microgravity, but this is still insufficient to achieve the timescales necessary to observe a steady-state spherical diffusion flame in microgravity. During these short times, the flame either continues to grow, or extinguishes. No experimental evidence has been shown to prove or disprove the existence of a

steady-state spherical diffusion flame. Owing to this intrinsic time limit, terrestrial drop tower studies of gaseous spherical diffusion flames have focused on extinction [133,135-137].

While exact analytical solutions for a steady-state gaseous spherical diffusion flame have been presented, the solutions often include assumptions such as no radiation heat loss and/or constant transport properties [144,158]. Both radiation heat loss and the temperature dependence of transport properties (i.e., radiation-induced growth) have been shown to be a critical part of the transient growth process of microgravity spherical diffusion flames that leads to radiative extinction [55]. Thus, analytical solutions that neglect radiation and temperature-dependent transport properties are not able to confirm the existence of steady-state spherical diffusion flames.

Tang et al. attempted to achieve a steady-state flame without radiation using a numerical model but found that the outer temperature profile did not converge to a unique solution, and they concluded that a steady-state solution does not exist for the burner-stabilized spherical diffusion flame configuration [138-139]. Moreover, they concluded that without radiation extinction, the flame would grow indefinitely, or until radiative extinction.

Recently, as part of the NASA project Advanced Combustion via Microgravity Experiments (ACME), long-duration gaseous microgravity spherical diffusion flames been observed. Irace et al. [54] showed that for a normal flame configuration, flames can last up to 336 s. However, even after 336 s, the flame extinguished via radiative extinction.

While a steady-state spherical diffusion flame in microgravity exists in theory, the lack of experimental evidence has led some to doubt their existence [139]. These doubts are reasonable, considering the rapid flame growth that can occur owing to radiation heat loss [55]. This investigation aims to answer the question, “Do steady-state gaseous microgravity spherical

diffusion flames exist in the presence of radiation heat loss?" By conducting experiments on the ISS in a normal and inverse flame configuration, we have sufficient time in microgravity to address this question. Experimental results are compared to a transient numerical model. This investigation was conducted under the experiment Flame Design, which is one of six experiments under the NASA project ACME.

6.2 Methods

6.2.1 Experimental

Microgravity experiments are conducted aboard the ISS in the Combustion Integrated Rack (CIR). The experimental configuration and diagnostics are described in more detail in [54,55].

Normal (fuel issuing into an ambient of oxidizer) and inverse (oxidizer issuing into an ambient of fuel) flames are investigated. The fuel is ethylene (C_2H_4), the oxidizer is oxygen (O_2), and the diluent is nitrogen (N_2). For normal flames, pure or diluted fuel can be supplied from the burner, and the ambient oxygen concentration is limited to 40%, owing to safety concerns aboard the ISS. For inverse flames, 85% or less oxygen (the oxygen bottle is 85% O_2 and 15% N_2) can be supplied from the burner, and the ambient fuel concentration is limited to approximately 27% fuel at atmospheric pressure, owing to fuel bottle size.

Figure 1 shows a photograph of the experimental configuration. The burner is a 6.4 mm diameter porous stainless-steel sphere. The burner reactant and diluent are introduced into the porous sphere via a 1.17/1.5 mm (inside/outside diameter) tube. Because this tube was found to be physically weak, it was encased in a larger 1.6/1.83 mm support tube to avoid damage to the reactant supply tube during assembly on the ISS. Gas flow rates are controlled with mass flow controllers with an

estimated uncertainty of ± 5%. Flame ignition is achieved using a hot-wire retractable igniter that retracts after ignition.

The ACME chamber insert is a 105 L chamber with free volume of 88 L. Experiments are conducted in test sessions that can last up to 12 hours. At the beginning of each test session, the

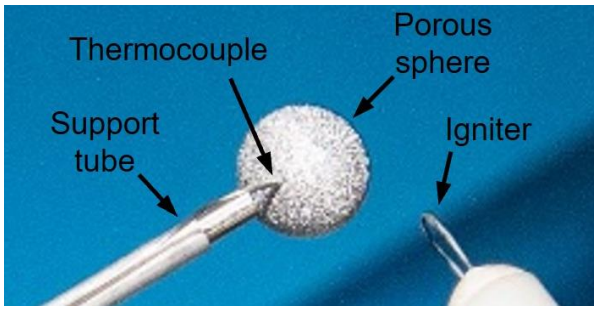

Fig. 6.1. Photograph of the experimental configuration aboard the ISS. Image courtesy of NASA.

chamber is filled to the desired ambient reactant concentration and pressure. The remainder of the test session is limited to the 12-hour time window, or up to 999 s of gas flow time. The concentration of the ambient reactant decreases marginally throughout the test session, as it is consumed by combustion. Quiescent conditions are established before each test, with the ambient at about 295 K. Between tests, a mixing fan is used to ensure a homogenous chamber environment. In this work, the pressure is approximately 1 bar.

Experiments are recorded at 30 frames per second (fps) using the ACME operations camera, a 0.44-megapixel color camera with an adjustable gain.

Flame radius is measured as a function of time, as in [54], using still images extracted from the ACME operations camera video. An ellipse is fit to the flame where the intensities are approximately midway between the peak blue and the ambient intensities, as in [54]. The flame diameter is taken as the axis of the ellipse perpendicular to the fuel supply tube. The flame is

typically quenched in the vicinity of the burner support tube, making it difficult to interpret the location of the flame sheet in that region. Additionally, the flame is shifted somewhat towards the burner support tube (i.e., the flame is spherical, but not concentric with the porous sphere). This is likely due to either reactant leakage where the fuel supply tube connects to the porous sphere creating a bulk flow towards the burner support tube, or to the lower temperature in the quenched region. Recent studies indicate the latter. Uncertainties in the flame radii are estimated to be ± 4%.

Spectral radiance of OH* (310 nm) is measured using a photomultiplier tube (PMT) with a bandpass filter. Burner temperature is measured using a sheathed 0.25 mm diameter type-K thermocouple embedded into the burner surface.

Peak gas-phase temperature as a function of time is measured using thin-filament pyrometry, as in [54]. The fibers inserted into the flame are 14 μm SiC fibers. Images are taken using the ACME data camera, a 1.4-megapixel color camera with a charge-coupled device (CCD) sensor and variable gain. The lens on the ACME camera allows for control of the zoom, focus, and aperture. The ACME camera was calibrated using a blackbody calibration source prior to launch. Fiber temperature is corrected to gas temperature by accounting for radiative losses [54]. The uncertainty in accuracy for an individual TFP measurement is estimated to be ± 100 K, owing to the inability to recalibrate the camera, the radiation correction, and uncertainties associated with testing in space. However, the difference in peak temperature for two times during a given test has an estimated uncertainty of ± 10 K. Thus, the fiber temperatures can provide the qualitative trends necessary to evaluate the existence of steady-state flames.

6.2.2 Numerical model

Transient simulations are performed using the SphDiff numerical model used in refs. [54,136,137,151,152], which is a modification of Sandia PREMIX [153]. The governing equations are discretized using finite differencing methods, and then solved using a modified Newton method. The equations for conservation of mass, energy, and species are the same as in [54]. Radiation from and reabsorption by CO, CO_2, and H_2O is included and calculated using a detailed absorption/emission statistical narrow band model with wavenumbers ranging from 150 – 9300 cm^{-1}, coupled with a discrete-ordinates method with 20 ordinates. A detailed description of both methods is found in [154].

The grid algorithm employed is the same as in [54]. To simulate an infinite boundary, the computational domain spans from 0.32 cm at the burner surface to 1000 cm at the outer boundary. There was no detectable change in species or temperature at the outer boundary, indicating that the size of the domain is sufficiently large. The detailed boundary conditions for each equation are shown in [154]. As noted in [54], the effect of burner heating is second order, but non-negligible. In this work, the inner boundary is held constant at 298 K. This represents the most rigorous condition for steady-state, as burner heating has been shown to heat the gas leaving the porous sphere, supporting the flame [54].

Because the transient terms in the governing equations are expressed using an implicit Euler method, the time step is varied during simulations to ensure accuracy. As the problem approaches steady-state, the maximum time step necessary to accurately capture the changes in the system increases. Thus, in order to achieve the long times necessary to demonstrate steady-state, the time

step is increased as the solution becomes steadier [154]. The UCSD mechanism with 57 species and 270 reaction steps is used to simulate the flames [155].

6.3 Analytical

6.3.1 Characteristic time to reach steady-state

In a spherical diffusion flame, the transport of the ambient reactant is governed by diffusion. When a physical system is governed by diffusion, it theoretically takes an infinite amount of time for that system to reach steady-state. While this is true in the strict definition of steady-state, there exists a finite time at which the diffusion-controlled process is effectively at steady-state (i.e., the difference between the steady-and transient solution is less than a specified tolerance) [164]. The time it takes to reach this transition is often characterized as proportional to,

$$t_{diff} = l^2/D \, , \tag{6.1}$$

where t_{diff} is the characteristic time for diffusion, D is the diffusivity, and l is a characteristic length scale. However, the choice of the diffusivity and characteristic length scale in Eq. 6.1 is system dependent and is not always obvious.

For an approximation of t_{diff}, the diffusivity is taken as the diffusivity of nitrogen at ambient temperature (20.4 mm^2/s), and the characteristic length is defined as the outer edge of the thermal boundary at steady-state where a perturbation of the peak temperature results in a negligible change in temperature. To determine this characteristic length scale, the outer zone of the steady-state temperature solution for a spherically symmetric diffusion flame provided in ref. [156] is evaluated. Rearranging the solution from [156] shows that for a change in flame temperature of, ΔT_f, there is a change in temperature in the outer zone at radius r given by

$$\Delta T(r) = \Delta T_f\{[1-\exp(-Z_T\dot{m}/r)]/[1-\exp(-Z_T\dot{m}/r_f)]\}\,, \tag{6.2}$$

where T is temperature, $\dot{m}$ mass flow rate, and r_f flame radius. Assuming unity Lewis number, the parameter Z_T is defined by

$$Z_T = 1/4\pi\rho D\,, \tag{6.3}$$

where ρ is density and D the diffusivity. In the numerator of Eq. 6.2, the characteristic length $Z_T\dot{m}$ determines, through the dimensionless combination ($Z_T\dot{m}/r$), the rate of decrease in ΔT as r goes to infinity. It is interesting to note that this decrease in ΔT as r goes to infinity is not exponential, but much slower, asymptotically. For example, the length scale (distance r) that is required to reduce $\Delta T(r)$ to $1/100^{th}$ of that of ΔT_f is approximately 100 times the characteristic length, $Z_T\dot{m}$. Assuming an $\dot{m}$ of 10 mg/s, evaluating ρD as in [54] with a characteristic temperature of 1300 K, and assuming that a location where ΔT is reduced by a factor of 100 is sufficient to define a thermal boundary, then a length scale of approximately 1.6 m is obtained. In other words, if the flame temperature is perturbed 100 K, then at 1.6 m away from the flame the temperature would be perturbed only 1 K. This rather large length scale may be nonintuitive and is a consequence of the spherical geometry. Even more enlightening, this length scale results in a characteristic diffusion time of approximately 130,000 s. Thus, if a steady-state spherical flame exists, a significant duration of microgravity must be available to demonstrate it.

6.3.2 Identifying initial conditions favorable for steady-state spherical diffusion flames

It has been shown that after ignition, microgravity spherical diffusion flames can grow rapidly with time. As they grow, the rate of radiation heat loss increases asymptotically due to the

production of radiating product gases (primarily CO_2 and H_2O) and the increasing path length of the radiating products (i.e., increasing gaseous emissivity). This increasing radiation causes the peak (i.e., flame) temperature to decrease, while the total heat release rate from the flame remains relatively constant. It has recently been concluded that the continuous growth of spherical diffusion flames can be attributed to a combination of the intrinsic development of a diffusion-controlled system as it approaches steady-state and the temperature dependence of transport properties (i.e., radiation-induced growth) [9]. Irace et al. observed that this radiation-induced growth process leads to radiative extinction for many flames when the flame temperature reduces to the critical temperature for radiative extinction (1130 K) [54,55,136,139,143]. This is why in past microgravity studies of burner-supported spherical gaseous flames, the flames have either extinguished or the experiment ended due to finite duration microgravity (e.g., in drop towers).

The question is, is it possible to reach some asymptotic extent of radiation before the flame temperature has reached the extinction temperature? If so, a steady-state gaseous spherical diffusion flame can exist in the presence of radiation heat loss.

An approach to addressing this question can be realized by considering recent results of Irace et al. [55], where a simple theory to calculate the flame size at extinction for a spherical diffusion flame in microgravity was developed based on their experimental observations of a critical extinction temperature and a critical reactant-based mass flux at the flame. Based on their theory, the flame radius at extinction, r_{ext}, can be calculated for any spherical flame from

$$r_{ext} = sqrt(\dot{m}_{reactant}/4\pi J_{cr,reactant}) \,, \tag{6.4}$$

where $\dot{m}_{reactant}$ is the mass flow rate of the reactant from the burner (fuel for normal flames and oxygen for inverse flames), and $J_{cr,reactant}$ is the critical mass flux of burner reactant at extinction (0.2 g/m^2-s for ethylene and 0.68 g/m^2-s for oxygen).

The implication of this finding is that if a flame is larger than r_{ext} it will extinguish. But more importantly for this work, if conditions can be found where the flame is smaller than this size, then a steady-state spherical flame can exist. Whether such conditions are possible now becomes the question. To address this, we follow the work of [54] and adapt the quasi-steady results from droplet combustion to obtain the steady-state flame radius of gaseous microgravity spherical diffusion flames. For a normal spherical diffusion flame, this is given by

$$r_{f,normal} = \dot{m}_{total}/4\pi\rho D\ln(1/1-Z_{st}) , \tag{6.5}$$

where r_f is flame radius, $\dot{m}_{total}$ is total mass flow rate from the porous sphere, ρ is density, D is diffusivity, and Z_{st} is the stoichiometric mixture fraction. Z_{st} is described in detail in [124]. Eq. 6.5 can be easily adapted to the inverse flame configuration by taking the stoichiometric mass of fuel per mass of oxidizer, f, in terms of Z_{st} for inverse flames as,

$$f = (1-Z_{st})/Z_{st} . \tag{6.6}$$

Then, the flame radius for an inverse spherical diffusion flame is given by

$$r_{f,inverse} = \dot{m}_{total}/4\pi\rho D\ln(1/Z_{st}) . \tag{6.7}$$

While having an equation for the theoretical steady-state flame radius is useful, this does not, in and of itself, prove that a steady-state flame can exist because it is possible that the flame will radiative extinguish before it reaches this radius. Nonetheless, as noted above, Eq. 6.8 gives an equation for the flame radius at extinction, and thus, if the flame radius, r_f, given by Eqs. 6.5 or

6.7, is less than the flame size at extinction, r_{ext}, given by Eq. 6.8, the possibility for steady-state flames can exist. To characterize this condition, we define R as

$$R = r_f/r_{ext} , \tag{6.9}$$

wherein *R* serves to identify a limit condition where flames can exist in steady-state. Flames with R > 1 cannot exist at steady-state because their steady-state size is greater than their extinction size. In contrast, flames with R < 1 should approach steady-state.

Solving Eqs. 6.5, 6.7, and 6.8 for various initial conditions (e.g., fuel concentration (X_{C2H4}), oxygen concentration (X_{O2}), and $\dot{m}$) where R=1 allows one to identify a limit for where steady-state flames can exist. Figures 6.2a and 6.2b show $\dot{m}_{total}$ as a function of ambient reactant concentration for

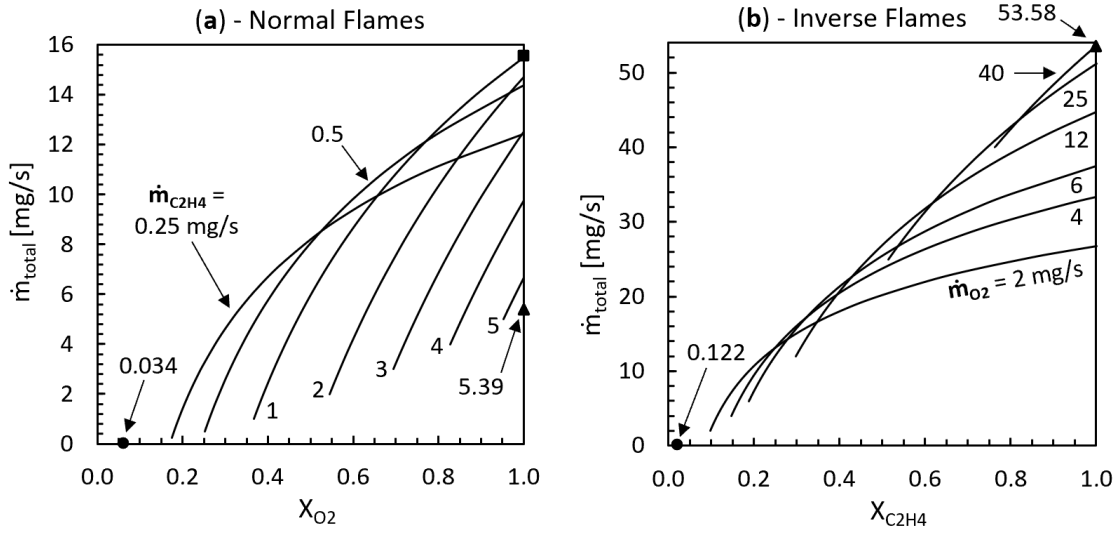

Fig. 6.2. $\dot{m}_{total}$ as a function of ambient reactant concentration for various (**a**) $\dot{m}_{C2H4}$ for normal flames and (**b**) $\dot{m}_{O2}$ for inverse flames, where R=1. Flames to the right of each curve should exhibit steady-state behavior and flames to the left should extinguish. The circle and triangle denote the minimum and maximum reactant flow rate at which a steady-state flame can exist, respectively, defined by the adiabatic flame temperature being less than 1130 K. The square denotes the maximum $\dot{m}_{total}$.

various burner reactant rates where R=1 for normal and inverse flames, respectively. Equations 6.5 and 6.7 are evaluated as in [54], with the exception that the characteristic temperature is taken as the average between the ambient and critical extinction temperature (1130 K).

Using Figs. 6.2a and 6.2b, one can easily identify initial conditions that can lead to steady-state spherical diffusion flames. In both figures, flames to the right of each curve should approach steady-state (i.e., R < 1), and flames to the left should extinguish radiatively (i.e., R > 1).

Furthermore, it is interesting to note that the shape of the curves is primarily a function of dilution and stoichiometry. For a given burner reactant flow rate the flame extinction size is constant, and as the burner reactant concentration is reduced (i.e., $\dot{m}_{total}$ increases), the steady flame size increases, thus the ambient reactant concentration must increase to reduce the flame size back to where R=1.

6.4 Results & Discussion

6.4.1 Challenges to achieving steady-state spherical diffusion flames aboard the ISS

Experimentation aboard the ISS comes with intrinsic limitations that make it difficult to achieve most of the conditions in Figs. 6.2a and 6.2b. First, the ambient reactant concentration is limited to 40% for normal flames and 27% for inverse flames, significantly limiting the steady-state conditions attainable. Furthermore, the temperature limit of the porous sphere is 450 – 500°C, and the small flow rates necessary to achieve steady-state flames result in small flames that overheat the burner [54]. Moreover, perhaps the most important limitation is the finite boundary. In experiments, the ambient reactant concentration decreases with time, and the nearest wall of the cylindrical ACME chamber insert is only 19 cm from the burner center. Based on the characteristic diffusion time from Eq. 6.1, the finite chamber size will become a disturbance well before the flame reaches steady-state. Owing to these experimental limitations, steady-state spherical

diffusion flames are first investigated numerically. Numerical results and conclusions will then be compared to the steadiest and longest burning flames observed aboard the ISS.

6.4.2 Modeling steady-state spherical diffusion flames

The critical point for radiative extinction is best defined in terms of temperature [55,133,136]. If the change in flame temperature with time becomes negligible, it is reasonable to assume that the flame is near its steady-state and would not extinguish in infinite time. Thus, the flame temperature is used to calculate the threshold specified to denote the finite time for steady-state in the numerical simulations. The threshold is defined as, when the change in flame temperature with time relative to the average of the five previous time steps is less than 1E-5, given as,

$$(T_{fi}\text{-}(1/5)\sum_{n=i-6}^{n=i-1} T_{fn})/(t_i\text{-}(1/5)\sum_{n=i-6}^{n=i-1} t_n) < 1E\text{-}5, \quad (6.10)$$

where T_f is flame temperature and t the elapsed time.

The parameter R in Figs. 6.2a and 6.2b is used as the basis for choosing flames that should or should not exhibit steady-state behavior. Table 6.1 shows the initial conditions for six spherical diffusion flames that have been simulated. NS1 (normal simulated) and IS1 (inverse simulated) are chosen such that R>1, indicating that the flames should extinguish. However, NS1 and IS1 are not far from steady-state behavior and will likely burn for a significant time before extinction. NS2 and IS2 are chosen such that R<1 and the flames should exhibit steady-state behavior. IE1 (inverse experiment) and IE2 are two experimental inverse flames that had R<1.

Table 6.1
Initial conditions for the spherical flames investigated

Flame	X_F	X_O	$\dot{m}_{Reactant}$ [mg/s]	$\dot{m}_{Total}$ [mg/s]
Normal				
NS1	0.2	0.5	1.2	6
NS2	0.2	0.68	1.2	6
Inverse				
IS1	0.34	0.2	4.44	20
IS2	0.57	0.2	4.44	20
IE1	0.257	0.212	2.37	10.05
IE2	0.27	0.212	2.15	9.11

Figure 6.3a shows simulated R as a function of time for each flame. The simulation is stopped when the flame extinguishes, or when it reaches the threshold for steady-state in Eq. 6.10. As expected, IS1 and NS1 both extinguish (when R=1). They each burn at least 1200 s, which is a significant amount of time when compared to a typical diffusion flame. However, their burn times are still not comparable to the characteristic steady-state diffusion time of the system from Eq. 6.1.

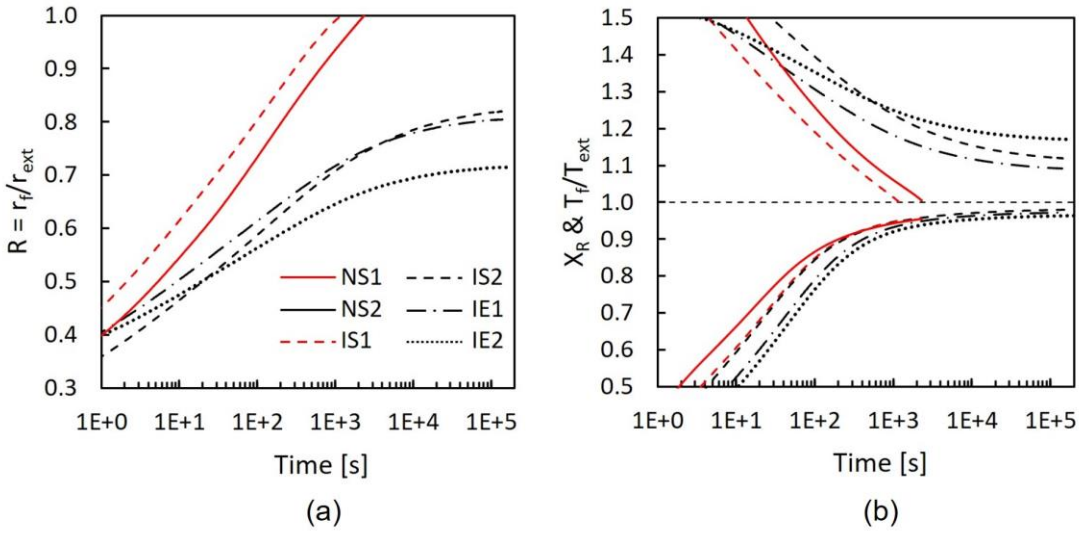

Fig. 6.3. (**a**) Simulated R as a function of time for each flame in Table 6.1. (**b**) Flame temperature normalized by the critical extinction temperature and radiative loss fraction as a function of time for each flame in Table 6.1. In (**b**), curves above one represent the normalized temperature and curves below one represent the radiative loss fraction.

NS2 and IS2 both exhibit steady-state behavior and asymptote to R values of 0.75 and 0.82, respectively. Both flames burn over 150,000 s before reaching the prescribed threshold, confirming the existence of steady-state flames in the presence of radiation heat loss, and validating the theories illustrated in Figs. 6.2a and 6.2b. IE1 and IE2 also reach the threshold for steady-state and will be further evaluated using the experimental data below.

Figure 3b shows simulated flame temperature normalized by the critical extinction temperature, and the radiative loss fraction, X_R as a function of time. The radiative loss fraction is defined as the rate of radiation heat loss, Q_R, divided by the heat release rate, Q_C. This figure shows that for flames that exhibit steady-state behavior, the radiative loss fraction asymptotes to a nearly constant value, preventing the flame temperature from decreasing and allowing the flame to reach steady-state. While the radiative loss fraction for NS1 and IS1 also shows asymptotic behavior, the radiation does not asymptote to the extent necessary for steady-state before the flames reached the critical point for radiative extinction.

6.4.3 Experimental results

IE1 and IE2 were both investigated experimentally aboard the ISS and burned until the flow of gas was stopped. IE1 burned for 867.6 s and flow was stopped due to time limitations. IE2 burned for 126.4 s and flow was stopped due to the burner reaching its limit temperature.

Figure 6.4 shows measured OH* emission normalized by the PMT saturation value (0.1 W/cm^2), flame temperature normalized by the extinction temperature, and R as a function of time for IE1 and IE2. Experimental flame temperature is not available for IE2, owing to the thin filament fibers

not being inserted into the flame, and is only included after 400 s for IE1 because that is when the flame reached the fiber location.

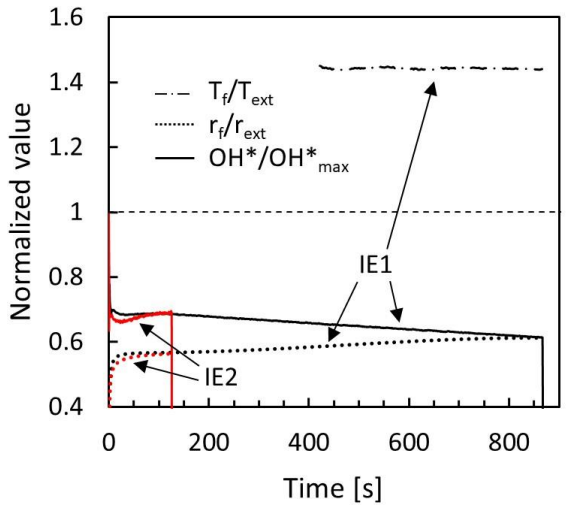

Fig. 6.4. Measured OH* emission normalized by its saturation value, flame temperature normalized by the extinction temperature, and flame radius normalized by extinction radius as a function of time for IE1 and IE2. The fibers were not inserted in IE2.

Burning heating is significant for both flames, which results in the initial increase in OH* emission. The growth rate of both flames is also slower at short times, owing to the effect of burner heating [54]. After the burner temperature reaches a peak in IE1 (at 180 s), the flame exhibits quasi-steady behavior, as the flame continues to slowly grow and decrease in OH* emission.

Figure 6.5 shows photographs of (a) IE1 at 11 s and 840 s, and, for comparison, (b) a typical unsteady flame at 2 s and 10 s. It is clear that IE1 is growing very slowly compared to the flame in Fig. 6.5b. Much of the flame growth for 1E1 can be attributed to the intrinsic diffusive growth of the system, but the finite boundary, and resulting decrease in ambient reactant concentration also plays a role. It is noteworthy that the ambient reactant concentration drops 2.4% over the duration of IE1.

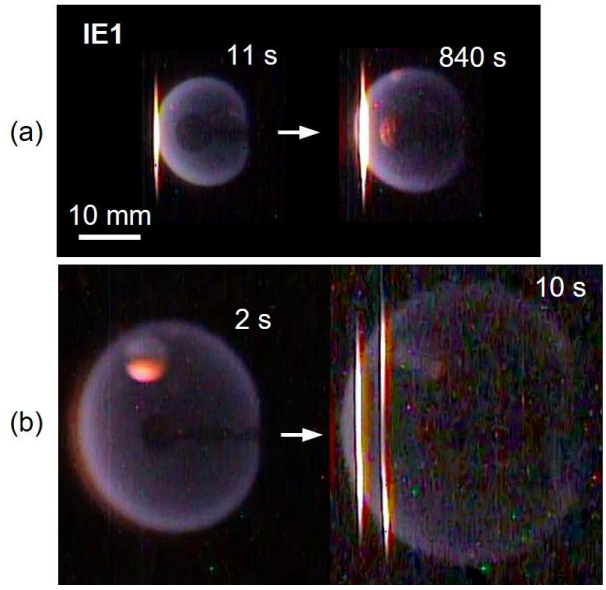

Fig. 6.5. Photographs of (**a**) IE1 and (**b**) an inverse flame of X_{O2} = 0.85 and $\dot{m}_{O2}$ = 6 mg/s issuing into X_{C2H4} = 0.12.

Considering the quasi-steady behavior, long burn time attained, and effect of the outer boundary, the experimental results presented herein indicate that steady-state flames do exist in the presence of radiation heat loss.

6.5 Conclusions

The existence of steady-state gaseous microgravity spherical diffusion flames in the presence of radiation heat loss was investigated using a transient numerical model and experiments conducted aboard the ISS. The following conclusions were obtained:

1) Steady-state gaseous microgravity spherical diffusion flames do exist in the presence of radiation heat loss. While spherical diffusion flames theoretically take infinite time to reach steady-state, there is a finite time, on the order of 100,000 s in which the system is effectively at steady-state.

2) In order for a steady-state flame to exist, the steady-state flame size must be less than the critical flame size for extinction. The flame must also develop sufficiently fast compared to the time for the radiating region of product gases to develop such that the flame temperature does not drop to the critical temperature for radiative extinction.
3) Spherical diffusion flames that exhibit early signs of steady-state behavior can be observed experimentally. However, steady-state spherical diffusion flames are difficult to achieve in experiment, owing to the intrinsic limitations of time, a finite boundary, and burner material temperature limits.

This investigation has demonstrated the existence of steady-state gaseous microgravity spherical diffusion flame in the presence of radiation heat loss experimentally and numerically. Further research must be conducted to investigate steady-state spherical flames using other fuels, and the effects of pressure.

Chapter 7: Effects of ultra-low strain on the kinetic structure of non-sooting ethylene diffusion flames

7.1 Introduction

Ethylene (C_2H_4) is one of the most important intermediate species in the oxidation of aliphatic fuels [165]. Thus, a fundamental knowledge of its oxidation is important for the development of combustion models that are valid over a wide range of temperatures. Ethylene microgravity spherical diffusion flames that radiatively extinguish provide a unique opportunity to study the kinetics of ethylene oxidation over a wide range of temperatures. Microgravity spherical diffusion flames ignite at high temperatures (i.e., near the adiabatic flame temperature at the instant of ignition), and then, owing to increasing flame size and thermal radiation, their temperature gradually decreases until they reach the critical temperature for radiative extinction (1130 K at atmospheric pressure) [54,55,136,139].

The reaction path for the oxidation of strained (e.g., counterflow) ethylene diffusion flames is well-understood for flames with a peak temperature greater than 1500 K [165]. Sun et al. [165] and Skeen et al. [121] studied the kinetic structure of non-sooting ethylene flames and elucidated the dominant reactions for ethylene oxidation. The reaction path shown in Fig. 7.1 outlines the critical reaction steps described in [165]. In Fig. 7.1, fuel pyrolysis is defined by

$$C_2H_4 + H \leftrightarrow C_2H_3 + H_2 \tag{7.1}$$

$$C_2H_3 + M \leftrightarrow C_2H_2 + H + M, \tag{7.2}$$

with conversion of C_2H_4 to acetylene (C_2H_2). The primary oxidation zone is then defined by the oxidation of C_2H_2 to form CO, which is dominantly via O atoms and the reactions:

$$C_2H_2 + O \leftrightarrow CH_2 + CO \tag{7.3}$$

$$C_2H_2 + O \leftrightarrow HCCO + H \tag{7.4}$$

$$HCCO + H \leftrightarrow CH_2 + CO \tag{7.5}$$

$$CH_2 + O_2 \leftrightarrow HCO + OH \tag{7.6}$$

$$HCO + M \leftrightarrow CO + \mathrm{H} + \mathrm{M}. \tag{7.7}$$

The secondary oxidation zone is then defined by the formation of the stable products CO_2 and H_2O via the reactions:

$$CO + OH \leftrightarrow CO_2 + H \tag{7.8}$$

$$H_2 + OH \leftrightarrow H_2O + H. \tag{7.9}$$

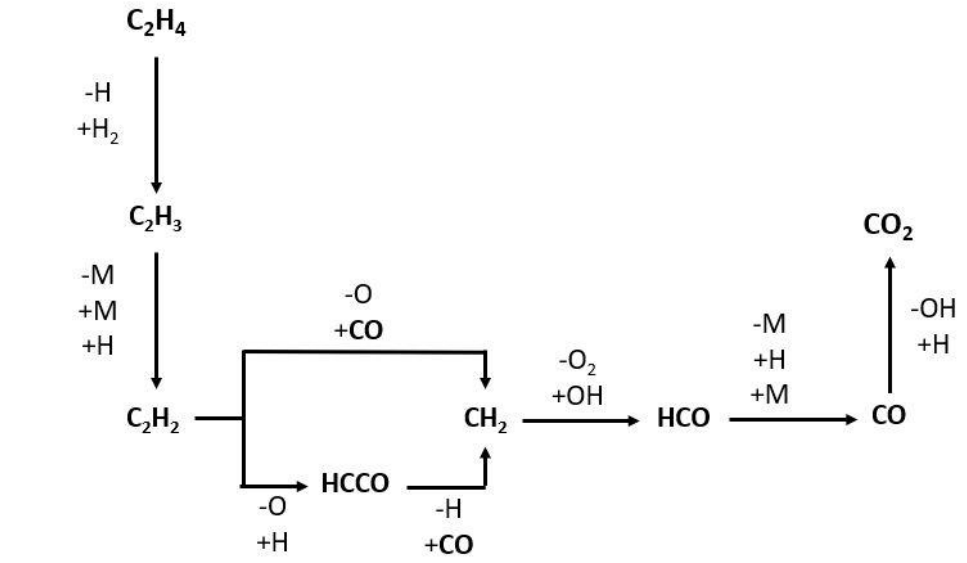

H-O Reaction Chain Cycle

7.10	$H+O_2<=>OH+O$	Branching
7.11	$H_2+O<=>OH+H$	Branching
7.9	$H_2+OH<=>H_2O+H$	Carrying

Other Radical Reactions

7.12	$H_2O+O<=>2OH$	Branching
7.13	$H+OH+M<=>H_2O+M$	Terminating
7.14	$H+O_2(+M)<=>HO_2(+M)$	Carrying
7.15	$HO_2+OH<=>H_2O+O_2$	Terminating

Fig. 7.1. Dominate reaction pathway for the oxidation of ethylene in a strained diffusion flame.

As seen in Fig. 7.1, the net production of radicals (e.g., O, H, and OH) is critical for sustained combustion. The critical reactions in the radical pool for a typical strained ethylene diffusion flame, outlined in Fig. 7.1, are the classic hydrogen-oxygen reaction scheme [58], given by reaction 7.9 and,

$$H + O_2 \leftrightarrow OH + \mathrm{O} \tag{7.10}$$

$$H_2 + O \leftrightarrow OH + \mathrm{H}, \tag{7.11}$$

and the reactions:

$$H_2O + O \leftrightarrow 2OH \tag{7.12}$$

$$H + OH + M \leftrightarrow H_2O + \mathrm{M}. \tag{7.13}$$

On the oxidizer side of the radical pool, at the boundary of the reaction zone, relatively inactive HO_2 radicals are produced and terminated to form H_2O via the reactions:

$$H + O_2 + M \leftrightarrow HO_2 + \mathrm{M} \tag{7.14}$$

$$HO_2 + OH \leftrightarrow H_2O + O_2 \tag{7.15}$$

Sun et al. [165], and Skeen et al. [121], also elucidated the reactions that dominate the heat release zone for these strained ethylene flames. Skeen et al. [121] distinguished four heat zones within the flame, a fuel pyrolysis zone that is either endothermic or slightly exothermic (depending on Z_{st}), a high heat intensity zone where C_2H_2 is oxidized by O (e.g., Eqs. 7.3 and 7.4), a moderate intensity zone where most CO_2 and H_2O are formed (e.g., Eqs. 7.8, 7.9, and 7.11), and a broad low heat intensity zone that extends into the oxygen rich region (e.g., Eqs. 7.14 and 7.15). These heat zones agree well with the heat release profiles of Sun et al. [165]. Furthermore, Skeen et al. [121], found

that the location of Z_{st} is always near the peak rate for the oxygen consumption reaction, Eq. 7.10, and that the location of peak heat release and peak temperature are dependent on the location and structure of the heat release profiles.

In this work, we study the reaction path and heat release rate for the oxidation of ethylene under ultra-low strain conditions at high temperature (1600 K) and low temperature (1130 K) using microgravity spherical diffusion flames. The residence time under ultra-low strain conditions is significantly higher than in a strained flame and may have a large impact on chemical kinetics. This work is the first steps of a systematic study on the kinetic structure of ethylene microgravity spherical diffusion flames at atmospheric pressure as they go from high temperatures near ignition to the critical temperature for radiative extinction (1130 K) [54,55,136,139]. The initial conditions for the simulated normal ethylene spherical diffusion flame studied are outlined in Table 7.1. The numerical model and detailed chemical kinetics used to simulate the flames are outlined in Chapters 4, 5, and 6 of this dissertation.

Table 7.1
Initial conditions of the simulated flame.

X_{O2} Ambient	X_{C2H4} Burner	$\dot{m}_{C2H4}$ [mg/s]	$\dot{m}_{N2}$ [mg/s]	T_{ad} [K]	P [atm]	Z_{st}
0.333	0.159	1.5	7.92	2370	1	0.4

7.2 High temperature kinetics

The chemical kinetics 2.5 s after ignition when the peak flame temperature is 1600 K are examined. Figure 7.2 shows the reaction rate profiles for the dominant reactions at 1600 K and Fig. 7.3 shows the dominant reaction pathway for the oxidation of ethylene, based on Fig. 7.2.

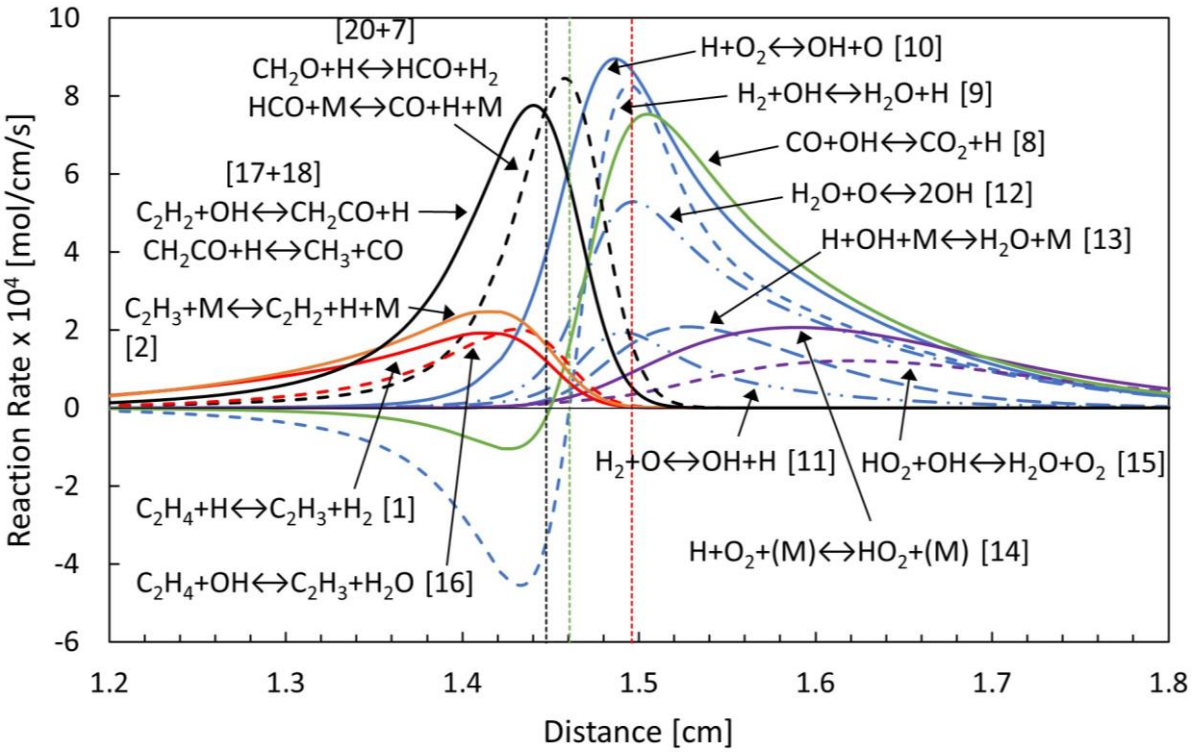

Fig. 7.2. Computed reaction rate profile of the ethylene spherical flame when the peak temperature is 1600 K. The vertical red, black, and green dashed lines indicate the locations of peak temperature, Zst, and peak total heat release rate, respectively.

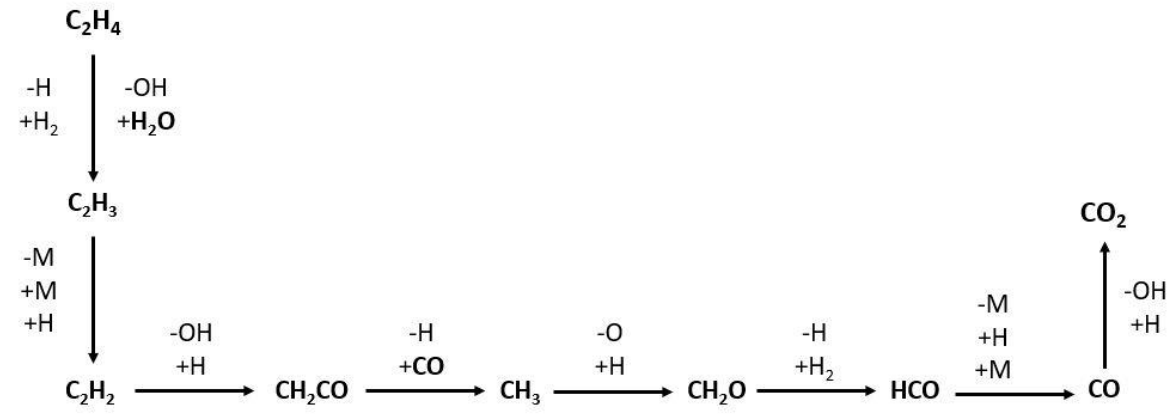

H-O Reaction Chain Cycle

7.10	$H+O_2<=>OH+O$	Branching
7.11	$H_2+O<=>OH+H$	Branching
7.9	$H_2+OH<=>H_2O+H$	Carrying

Other Radical Reactions

7.12	$H_2O+O<=>2OH$	Branching
7.13	$H+OH+M<=>H_2O+M$	Terminating
7.14	$H+O_2(+M)<=>HO_2(+M)$	Carrying
7.15	$HO_2+OH<=>H_2O+O_2$	Terminating

Fig. 7.3. Dominant reaction pathway for the oxidation of ethylene in a microgravity spherical diffusion flame at 1600 K.

Figures 7.2 and 7.3 show that the fuel pyrolysis zone is dominated by reactions 7.1, 7.2, and

$$C_2H_4 + OH \leftrightarrow C_2H_3 + H_2O. \quad (7.16)$$

This is analogous to the fuel pyrolysis zone for the strained counterflow ethylene flame with the exception that ref. [165] notes reaction 7.16 as of lesser importance when compared to reaction 7.1. In Fig. 7.2, reactions 7.1 and 7.16 are of comparable importance. The higher importance of reaction 7.16 is attributed to longer residence times and higher OH concentrations in the pyrolysis region, which will be discussed below.

Figs. 7.2 and 7.3 also show that in ultra-low strain microgravity spherical diffusion flames, the primary oxidation of C_2H_2 to CO is now via the OH radical in lieu of the O radical, which results in the cycle

$$C_2H_2 + OH \leftrightarrow CH_2CO + H \quad (7.17)$$

$$CH_2CO + H \leftrightarrow CH_3 + CO, \quad (7.18)$$

where C_2H_2 breaks down into CH_3 and CO. CH_3 eventually leads to the formation of CO via the reactions:

$$CH_3 + O \leftrightarrow CH_2O + H, \quad (7.19)$$

$$CH_2O + H \leftrightarrow HCO + H_2, \quad (7.20)$$

and reaction 7.7. The oxidation of C_2H_2 by OH instead of by O can be attributed to a combination of longer residence time and a higher concentration of OH. The longer residence time is an intrinsic feature of the ultra-low stain system and spherical geometry. The higher concentration of OH in both the fuel pyrolysis and primary oxidation zone is attributed to the reversal of reactions 7.8 and

7.9 in these regions, where the stable products H_2O and CO_2 react with H radicals to produce OH. This reversal and destruction of stable products is not seen in a typical strained flame [165]. In the ultra-low strain microgravity environment, the reversal of reactions 7.8 and 7.9 in the primary oxidation zone can be attributed to the longer residence time and the accumulating spatially broad region of high H_2O and CO_2 concentration, as there is no natural convection to remove them from of the system.

The secondary oxidation zone and radical pool in Figs. 7.2 and 7.3 show the same behavior as that of the strained ethylene flame in refs. [121,165]. It is interesting to note that in Fig. 7.2, the location of Z_{st} is to the left (i.e., the fuel side) of the radical pool and the peak of reaction 7.10, indicating that the location of oxygen consumption has shifted toward the fuel side of the flame.

Figure 7.4 shows the dominant spatial heat release profiles for the investigated flame at 1600 K. Similar to ref. [165], the fuel pyrolysis region is endothermic via reaction 7.2. The primary oxidation (i.e., oxidation of C_2H_2 to CO) is high heat intensity via reactions 7.17, 7.18, 7.19, 7.20, and

$$H + CH_3 + M \leftrightarrow CH_4 + M, \tag{7.21}$$

$$CH_2O + OH \leftrightarrow HCO + H_2O, \tag{7.22}$$

The secondary oxidation zone is moderate heat intensity and dominated by the formation of CO_2 and H_2O (reactions 7.8, 7.13, and 7.9). Last, the edge of the reaction zone on the oxidizer side has a low intensity heat zone dominated by the consumption of radicals and formation of H_2O (i.e., reactions 7.14 and 7.15).

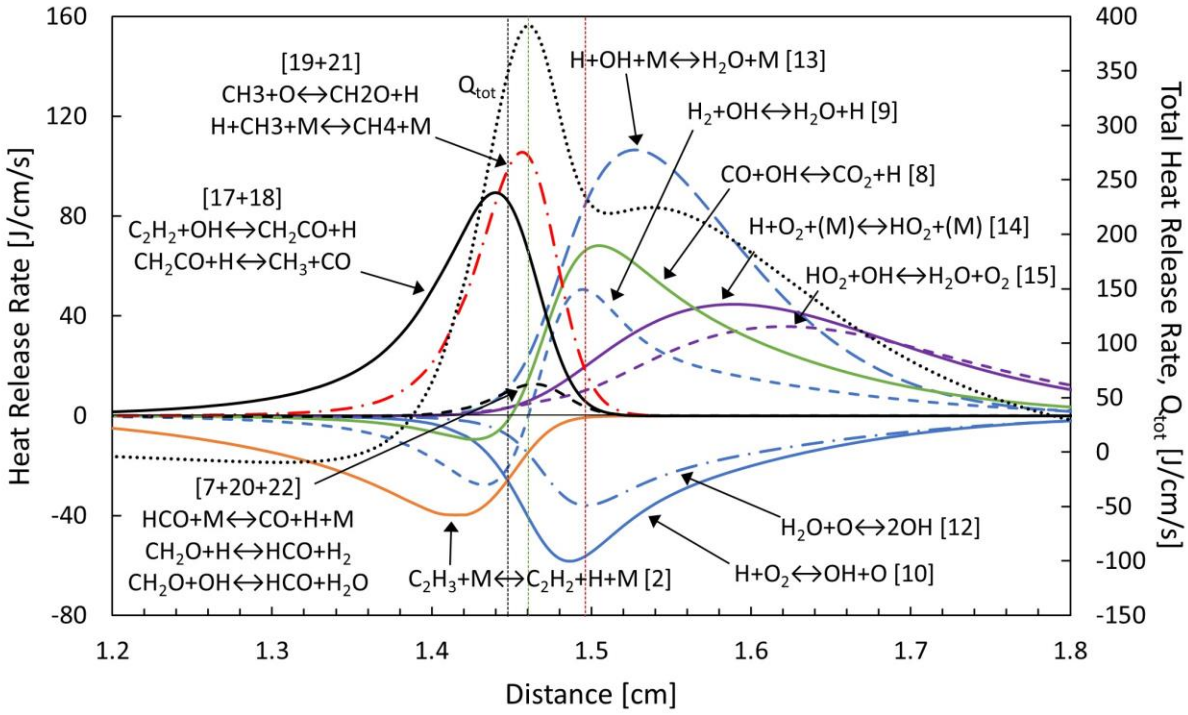

Fig. 7.4. Computed heat release rate profiles of the ethylene spherical flame when the peak temperature is 1600 K. The vertical red, black, and green dashed lines indicate the locations of peak temperature, Zst, and peak total heat release rate, respectively.

7.3 Low temperature kinetics

The chemical kinetics 38 s after ignition when the peak flame temperature is 1130 K, just before radiative extinction, are examined. Figure 7.5 shows the reaction rate profiles for the dominant reactions at 1130 K and Fig. 7.6 shows the dominant reaction pathway for the oxidation of ethylene based on Fig. 7.5.

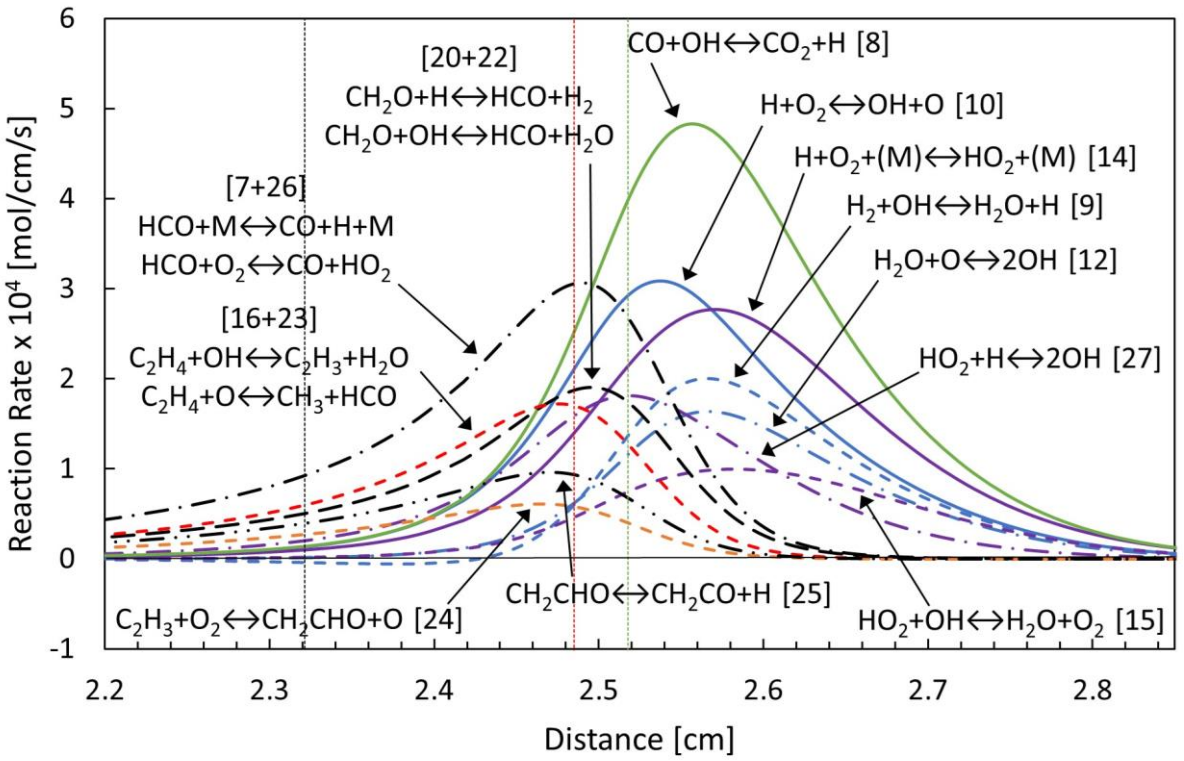

Fig. 7.5. Computed reaction rate profile of the ethylene spherical flame when the peak temperature is 1130 K. The vertical red, black, and green dashed lines indicate the locations of peak temperature, Zst, and peak total heat release rate, respectively.

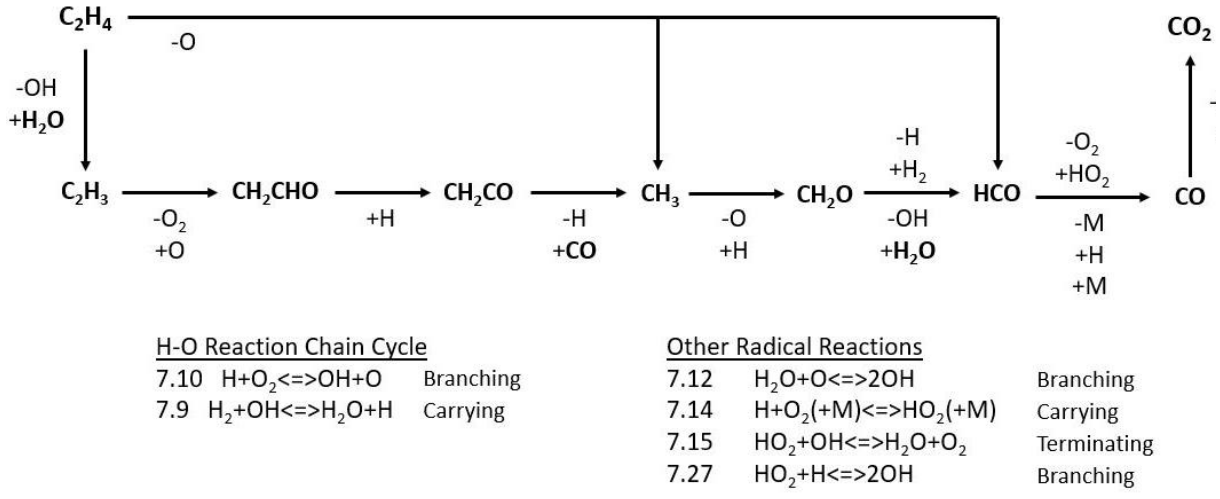

H-O Reaction Chain Cycle

7.10	$H+O_2<=>OH+O$	Branching
7.9	$H_2+OH<=>H_2O+H$	Carrying

Other Radical Reactions

7.12	$H_2O+O<=>2OH$	Branching
7.14	$H+O_2(+M)<=>HO_2(+M)$	Carrying
7.15	$HO_2+OH<=>H_2O+O_2$	Terminating
7.27	$HO_2+H<=>2OH$	Branching

Fig. 7.6. Dominant reaction pathway for the oxidation of ethylene in a microgravity spherical diffusion flame at 1130 K.

Figures 7.5 and 7.6 show that the breakdown of C_2H_4 at low temperature is dominated by reaction 7.16 and reactions:

$$C_2H_4 + O \leftrightarrow CH_3 + HCO \quad (7.23)$$

$$C_2H_3 + O_2 \leftrightarrow CH_2CHO + O. \quad (7.24)$$

The reactions 7.2 and 7.3, which were important for pyrolysis at high temperature, are now small and the breakdown of C_2H_4 occurs via the O radical in reaction 7.23, in lieu of the H radical in reaction 7.2, indicating a higher concentration of oxygen on the fuel side of the flame. Moreover, at low temperature, near extinction, C_2H_4 no longer pyrolyzes into C_2H_2. Instead, C_2H_4 directly forms CH_3 and HCO via an O radical in reaction 7.23, or it is consumed via OH to form C_2H_3, which is oxidized into a vinyloxy radical (CH_2CHO) by O_2.

Figure 7.5 also shows that the former fuel pyrolysis (where C_2H_4 pyrolyzed to C_2H_2) and primary oxidation zones (where C_2H_2 oxidized to CO) are now nearly coincident at low temperatures near extinction. They now form one zone, which is best described as the primary oxidation zone, where C_2H_4 is oxidized to CO via reactions 7.7, 7.16, 7.18, 7.19, 7.20, 7.22, 7.23, 7.24, and

$$CH_2CHO \leftrightarrow CH_2CO + H \quad (7.25)$$

$$HCO + O_2 \leftrightarrow CO + HO_2. \quad (7.26)$$

In a similar fashion, Fig. 7.5 shows that the former secondary oxidation zone, radical pool, and region of HO_2 formation/destruction have merged into one zone at low temperature. In this zone, CO_2 is formed via reaction 7.8 and H_2O is formed via reactions 7.9 and 7.15. The typical radical pool reactions, 7.11 and 7.13, have become negligible, and the rates of reactions 7.8, 7.10, and

7.12 have decreased substantially, thus decreasing the concentration of H, OH, and O radicals. The flame, however, is able to survive by shifting to low or zero activation energy reactions to generate radicals and ultimately produce heat, which will be discussed below. These low or zero activation energy reactions, which are now more important at low temperature are reactions 7.14, 7.15, and

$$HO_2 + H \leftrightarrow 2OH. \tag{7.27}$$

Overall, reaction 7.8 forms the spatial bounds for this secondary oxidation zone. The fuel side boundary of reaction 7.8 and the secondary oxidation zone is coincident with the fuel side boundary for reactions 7.10 and 7.27. This is interesting because reactions 7.10 and 7.27 produce the OH radicals needed to sustain reaction 7.8. No other reactions in the primary oxidation zone produce OH radicals, indicating that the reactions 7.10 and 7.27 are the limiting factor for reaction 7.8 on the fuel side of the secondary oxidation zone. Reaction 7.8 also produces H radicals, which are consumed by reactions 7.10 and 7.27. However, reactions 7.25 and 7.7 also produce H radicals which can be consumed by reactions 7.10 and 7.27.

It is also interesting to note that the location of Z_{st} has shifted further towards the fuel side of the flame, indicating that the location of oxygen consumption has shifted further to the fuel side of the flame. This is reasonable, as the net destruction of oxygen has decreased, owing to the reduction of reaction 7.10.

Figure 7.7 shows the dominant spatial heat release profiles for the investigated flame at 1130 K. In the primary oxidation zone (i.e., oxidation of C_2H_4 to CO), the heat release is dominated by the destruction of C_2H_4 and C_2H_3 via reactions 7.23 and

$$C_2H_3 + O_2 \leftrightarrow CH_2O + HCO, \tag{7.28}$$

the destruction of oxygenated species such as CH_2CO and CH_3OH via reactions 7.18 and

$$CH_3OH + M \leftrightarrow CH_3 + OH + M, \tag{7.29}$$

the destruction of CH_3 via reactions 7.19 and 7.21, and the formation of CO via 7.26. The formation of formaldehyde in reactions 7.28 and 7.19 is also important.

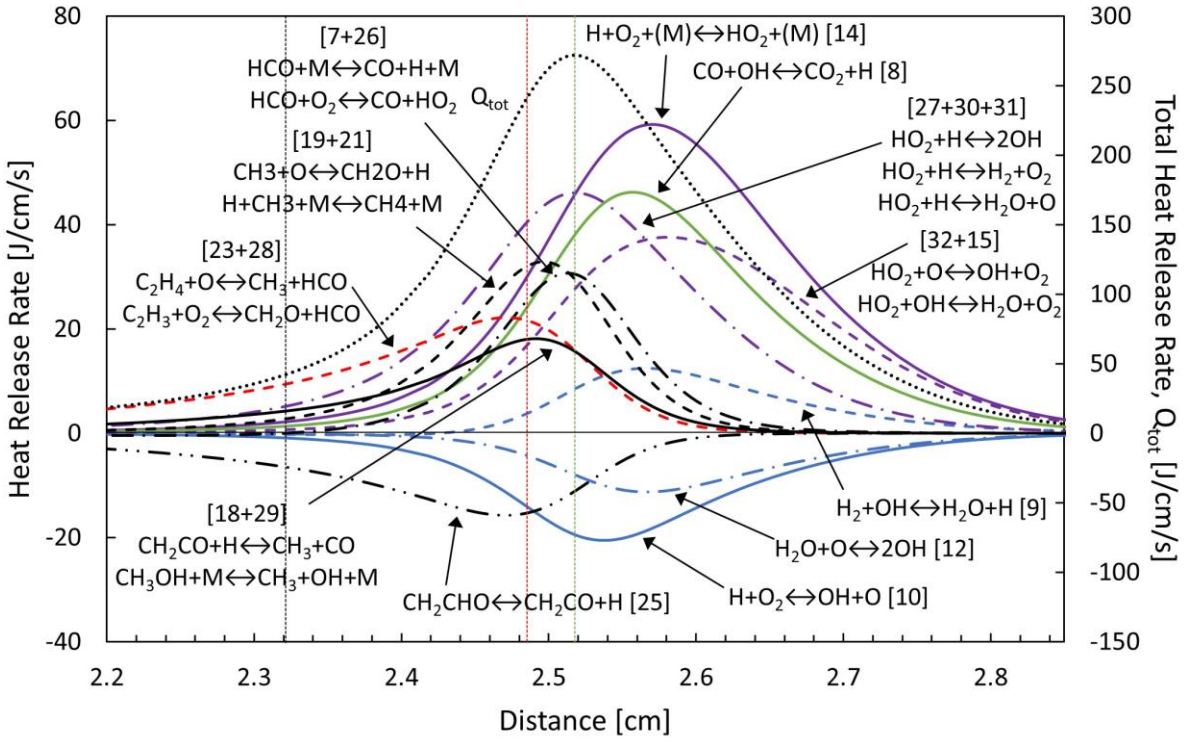

Fig. 7.7. Computed heat release rate profiles of the ethylene spherical flame when the peak temperature is 1130 K. The vertical red, black, and green dashed lines indicate the locations of peak temperature, Zst, and peak total heat release rate, respectively.

In the secondary oxidation zone, the heat release is dominated by the consumption of H radicals to form HO_2 radicals in reaction 7.14, the formation of CO_2 in reaction 7.8, and the consumption of H, O, and OH radicals by HO_2 in reactions 7.15, 7.27,

$$HO_2 + H \leftrightarrow H_2 + O_2, \tag{7.30}$$

$$HO_2 + H \leftrightarrow H_2O + O, \tag{7.31}$$

$$HO_2 + O \leftrightarrow OH + O_2. \quad (7.32)$$

Overall, as the flame transitions form high temperature chemistry to low temperature chemistry, high activation energy reactions become less favorable, and the flame shifts towards a new type of chemistry in which the typically relatively inactive HO_2 radicals become the dominant mechanism for producing heat.

7.4 Conclusions

This work outlines a preliminary effort to study the oxidation path and chemical kinetics of normal ultra-low strain ethylene microgravity spherical diffusion flames. The following observations have been made:

1) At high temperatures (i.e., above 1500 K), the path for the oxidation of C_2H_4 in ultra-low strain spherical diffusion flames is similar to that of a typical strained diffusion flame, with the exception that the oxidation of C_2H_2 occurs via OH radicals in lieu of H radicals. The oxidation of C_2H_2 by OH is caused by an increase in OH concentration in the primary oxidation zone. The increased residence time and the spatially broadened region of product gases in the ultra-low strain microgravity spherical diffusion leads to the destruction of CO_2 and H_2O by H in the primary oxidation zone to produce OH.
2) At low temperature, near extinction (i.e., 1130 K), the fuel pyrolysis and primary oxidation zone merge into one primary oxidation zone where C_2H_4 is oxidized to CO.
3) At low temperature, near extinction (i.e., 1130 K), the typical radical pool (H, OH, and O) is significantly depleted owing to the reduction of high activation energy reactions such as 7.9, 7.10, 7.11, and 7.12. In order to survive, the radical pool shifts to low or zero activation energy reactions that involve the typically relatively inactive HO_2 radical such as 7.14,

7.15, and 7.27. These HO_2 reactions along with reaction 7.8 and the primary oxidation zone become the dominant heat release.

4) At low temperature, the fuel side boundary of reaction 7.8 is limited by reactions 7.10 and 7.27, as they produce the OH necessary to sustain reaction 7.8.
5) The location of Z_{st} shifts further towards the fuel side of the reaction zone as the temperature decreases owing to a reduction in net oxygen consumption.

This work elucidated the fundamental chemical kinetics of these flames. Further work, such as a sensitivity analysis, must be conducted to discover the fundamental reason for extinction at 1130 K in atmospheric pressure ethylene microgravity spherical diffusion flames. Furthermore, reactions 7.13 and 7.14 are three-body reactions and highly pressure dependent. Preliminary analysis shows that increasing the pressure (e.g., 3-5 bar) allows the flame to survive to even lower temperatures (i.e., 975 K), exhibiting warm flame behavior. At even higher pressures (i.e., 10 bar or higher) near extinction, C_2H_4 begins to pyrolyze into C_2H_6 and C_3H_8, and CH_3OH and CH_2O become dominant species, indicative of cool flame behavior, but the flame goes out. The present kinetic model used does not have the reactions necessary to model cool flames. Thus, a detailed investigation of these flames at high pressure with cool flame chemistry could yield fruitful results.

Chapter 8: Flame-Assisted Additive Manufacturing (FLAMe): A novel approach to 3D printing ultra-high temperature materials

8.1 Introduction

Additive manufacturing (AM), particularly AM of metals, is an emerging technology that allows for rapid prototyping of complex, near-net shaped components of high temperature materials. These high temperature materials, such as refractory metals or alloys, are of great interest for thermal management systems, plasma facing materials, Nuclear Thermal Propulsion, solar probes, wing leading edges systems, and many more applications where material properties at high temperature can limit system performance [50,51,166-168].

Most metal AM methods use a concentrated energy source (e.g., laser, electron beam, or arc welding) to melt and fuse a pre-made feedstock material (e.g., powder or wire) layer-by-layer in a user-defined pattern to construct a 3D component. Two of the most common, state-of-the-art (SOA) methods are Direct Energy Deposition (DED) [169-171] and Powder Bed Fusion (PBF) [172-174]. In DED, a concentrated energy source is used to create a melt pool on a workpiece or previously deposited layer of material, and the feedstock powder is then blown into the melt pool using inert gas (e.g., argon) to be fused to the part. Several AM technologies are considered DED processes such as Laser Engineer Net Shaping (LENS), Laser Aided Manufacturing Process (LAMP), and Direct Metal Deposition (DMD) [175]. In PBF, a layer of feedstock powder is raked onto a surface and then a laser selectively melts a pattern into the layer of powder. After that, a new layer of powder is raked over the first, and the laser selectively melts the second layer to the first. This process continues, layer-by-layer, until 3D part is constructed.

Despite their many advantages, the primary disadvantages of these concentrated energy source metal AM techniques are porosity and residual stresses, which cause microcracking, particularly when considering high melting point materials. Refractory metals, for example, are highly desired

for their high melting/solidus temperature and high thermal conductivity, but these same properties make them particularly challenging to manufacture using DED or PBF. This is because DED and PBF require localized melting and re-solidification. The large thermal gradients between the melt pool and the substrate, coupled with the generally fast quench rates as the energy source moves around the workpiece, result in residual thermal stresses in the part [176-178]. Tungsten, which is the highest melting point refractory metal, is particularly susceptible to cracking under these conditions due to its high ductile-to-brittle transition temperature (DBTT) [179-187]. The high temperatures required to reduce surface tension and produce an acceptable melt pool without balling [182,188] also limit the flexibility to locally control the thermal history and create desired microstructural variations in the build. Furthermore, lack of fusion or vaporization at the melt pool in AM components results in porosity that contributes to low ductility and low fatigue life, particularly when coupled with microcracking [189-191].

Another disadvantage of current SOA metal AM methods is that they require a high-quality metal powder or wire that must be produced prior to the AM process. Powders are particularly difficult to produce for refractory metals, owing to their intrinsically high melting points, and for alloys, owing to the vastly different properties (e.g., melting temperature, vapor pressure) of the constituent elements. Using DED, a metal alloy can be fabricated by mixing the desired metal powders in the desired concentration *in-situ*, but this often results in poor elemental mixing and a non-homogeneous microstructure [192].

This work introduces a new method of AM, particularly well-suited for fabricating with high-temperature materials such as refractory metals, refractory multi-principal element alloys (MPEAs), and ultra-high temperature ceramics, that overcomes the shortcomings of current SOA metal AM methods. Flame-Assisted Additive Manufacturing (FLAMe) is a new AM technique in

which metals or alloys are rapidly synthesized via a high temperature gas-phase combustion process, and then selectively deposited in a semi-molten state at high velocities and appropriate temperatures onto a substrate.

Because FLAMe uses gas-phase precursors, there is no limit on the melting point of the material that can be produced, making the process ideal for high temperature materials. Furthermore, the resulting materials are very high purity because there is no oxygen in the system and the synthesis temperature is very high.

FLAMe is also well-suited for the fabrication of alloys because the metal vapors produced via the synthesis rection homogenously nucleate to form compositionally uniform particles. This makes FLAMe particularly advantageous for difficult to produce alloys such as W-Ti, where the melting point of W ($T_{m,W}$ = 3695 K) is sufficiently high relative to the boiling point of Ti ($T_{b,Ti}$ = 3560 K), that Ti will begin to vaporize before W melts. Figure 8.1a shows the deposition of compositionally uniform W-Ti particles using the FLAMe process. Fig. 8.1b illustrates the deposition of individual W and Ti particles via DED, where the deposited material is not compositionally uniform, owing

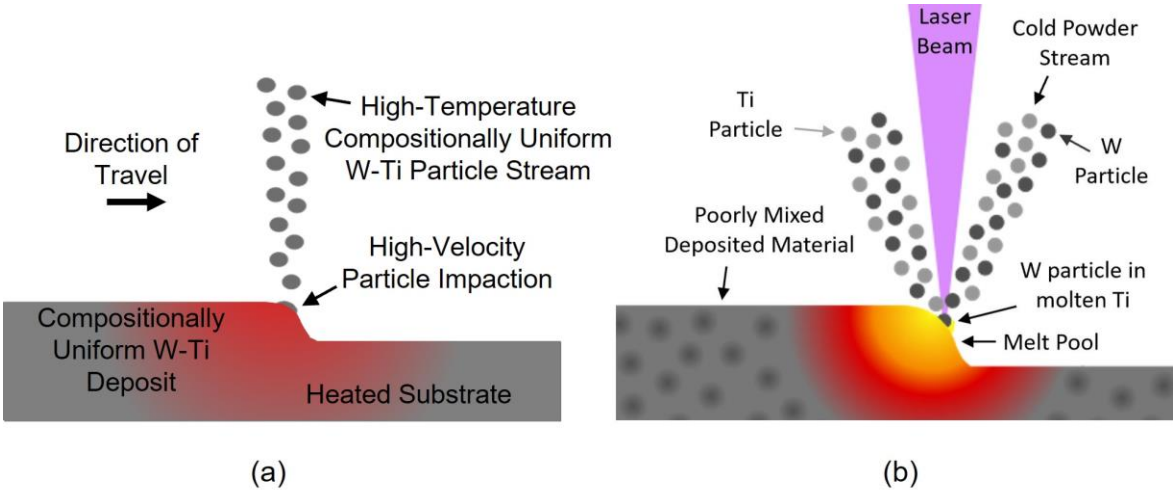

Fig. 8.1. Illustration of the production of a W-Ti alloy via (**a**) FLAMe and (**b**) DED.

to the vastly different material properties of the constituent elements. Additionally, because the flowrates of the gaseous precursors can be easily adjusted *in-situ*, FLAMe is ideal for producing functionally graded materials (FGMs) with locally tailored properties.

Moreover, FLAMe has the potential to mitigate, or even alleviate, the micro-cracking that occurs in SOA AM methods that rely on concentrated energy sources to create a melt pool. Because the pure or alloyed particles produced via the combustion synthesis process are in a high temperature state and are accelerated to high velocities, it will not be necessary to create a melt pool on the workpiece, thereby reducing the thermal gradient in the build, and the driving force for cracking (Fig. 8.1b). Furthermore, the fine particles are expected to produce a deposit with a fine microstructure, which could be coarsened as desired using a local heat source (e.g., a laser) immediately post-deposition.

FLAMe will allow for the development and fabrication of new high-purity materials with improved high-temperature properties and locally tailored material properties via compositional and microstructural gradients. This flexibility enables multiple separate components to be combined into a single piece, reducing weight, and simplifying assembly. In addition, the ability to focus the particle stream is well suited to the production of geometrically complex shapes, such as integrated cooling channels for components which experience extreme temperatures, e.g., wing leading edge systems, solar probes, plasma facing components in fusion reactors, and thin-wall parts that can be hermetically sealed.

The goal of this work is to outline the proposed FLAMe process and demonstrate deposition of a thin layer of titanium with minimal contamination of the synthesis reaction byproduct. Titanium is a well-characterized material that has been produced using the FLAMe synthesis chemistry, but

it has never been deposited without salt encapsulation of the synthesized Ti particles. Furthermore, Ti-6Al-4V is the most common material manufactured using current SOA metal AM methods, making Ti an important reference material [193].

8.2 Process synthesis chemistry

The synthesis chemistry is extremely versatile and ideally suited for the *in-situ* synthesis/deposition that is needed for the FLAMe process. This chemistry, also known as sodium/halide chemistry, is well-studied [194-206] and has been commercialized to produce salt-encapsulated powders of tantalum and niobium via the so-called sodium flame process (SFP), which was developed by Axelbaum et al. [201].

The precursors are metal halides (*e.g.*, $TiCl_4$, $NbCl_5$, WCl_6), and the reducing reactant is an alkali metal or alkaline earth metal (*e.g.*, Na, K, Mg). The halide reduction reaction is hypergolic (i.e., occurs spontaneously when the gaseous halide mixes with the alkali/alkaline earth metal vapor) and exothermic, thus producing a high-temperature non-premixed diffusion flame. The reactants are carried in an inert carrier gas (*e.g.*, Ar) and the concentration of the inert gas can be used to control the reaction temperature. The product of the reaction is a pure metal (*e.g.*, Ti,) if one metal precursor is used, or an alloy (*e.g.*, Nb-Ti-W) if multiple metal precursors are used. The byproduct is a salt (*e.g.*, NaCl, KCl, $MgCl_2$), which for the FLAMe process is kept in the gas phase and removed from the system due to its low concentration and by operating the deposition chamber at a modest vacuum ($\leq$ 76 torr), which will be discussed below in section 8.3. Since the process is hypergolic, no ignition source is required and there is no chance of flame extinction or incomplete reaction due to quenching.

Equation 8.1 shows the reduction of WCl_6 with Na to produce tungsten (W), and Eq. 8.2 shows the reduction of WCl_6 and $NbCl_5$ with Na to produce a binary, W-Nb alloy, where the ratio of elements is controlled by *a*.

$$WCl_6(g) + 6Na(g) + xAr \rightarrow W(l) + 6NaCl(g) + xAr\,, \tag{8.1}$$

$$WCl_6(g) + aNbCl_5(g) + (6+5a)Na(g) + xAr \rightarrow WNb_a(l) + (6+5a)NaCl(g) + xAr\,, \tag{8.2}$$

The temperature of the reaction can be as high as 2863 K for Eq. 8.1, and 3274 K for Eq. 8.2 [207]. Dilution of the reactants via inert gas can be used to reduce the temperature of the reaction. The materials produced via the sodium/halide chemistry are very high purity because the reaction occurs at high temperature and impurity metals form halides that remain in the gas-phase, as they exist in low concentrations [194]. Also, there is no intrinsic oxygen in the system. Furthermore, metal halide precursors are readily available and low cost, and sodium or magnesium reduction (in the liquid phase) is a common industrial process for producing, for example, titanium (i.e., the Kroll and Armstrong processes).

Figure 8.2 shows a diffusion flame of Na reducing $TiCl_4$ to produce pure Ti particles [196,199]. Owing to the homogenous nucleation of the gaseous metals at the flame front, the SFP has enabled

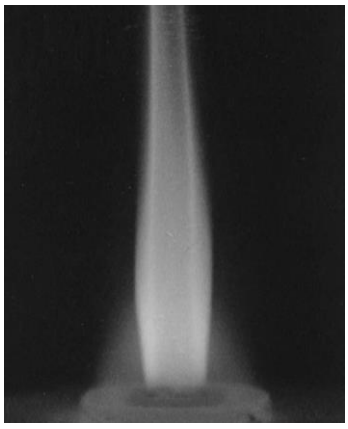

Fig. 8.2. Photo of a TiCl4-Na-Ar flame producing salt-encapsulated, pure Ti particles. Reproduced from [199].

the production of particles of difficult to manufacture metal alloys such as W-Ti [197] and Fe-Nb [206].

Furthermore, the sodium/halide chemistry can be strategically used to enable AM of highly desired refractory metals, refractory metal alloys, and many more promising high temperature materials yet to be produced, such as refractory MPEAs. Equation 8.3 shows the reduction reaction necessary to create the refractory HEA, MoNbTaVW:

$$MoCl_5+NbCl_5+TaCl_5+VCl_4+WCl_6+25Na+xAr \rightarrow MoNbTaVW(l)+25NaCl(g)+xAr\ . \qquad (8.3)$$

Table 8.1 shows a non-exhaustive list of metals that can be readily produced using the FLAMe process [201]. Any of the metals in Table 8.1 can be mixed to fabricate metal alloys, including many refractory MPEAs (e.g., NbTiVZr, MoNbTaW, HfNbTaZr, HfMoNbTiZr, MoNbTaVW, etc.). Table 8.2 shows a non-exhaustive list of ultra-high temperature ceramics that can be produced using the FLAMe process.

Table 8.1
Metals that can be fabricated using FLAMe.

Al	B	C	Co	Cu	Fe	Ge	Hf	Mo
Nb	Re	Si	Ta	Ti	V	W	Zn	Zr

Table 8.2
Ultra-high temperature ceramics that can be fabricated using FLAMe.

HfB_2	HfC	HfN	NbB_2	NbC	NbN	SiC	TaB_2
TaC	TaN	TiB_2	VC	VN	ZrB_2	ZrC	ZrN

8.3 The FLAMe process

Figure 8.3 shows a cross section of the FLAMe system and an illustration of the FLAMe process. The burner consists of four concentric tubes, suppling from innermost to outermost: $TiCl_4$ in an Ar carrier gas, Ar, Na in an Ar carrier gas, and Ar. From innermost to outermost tube, tube

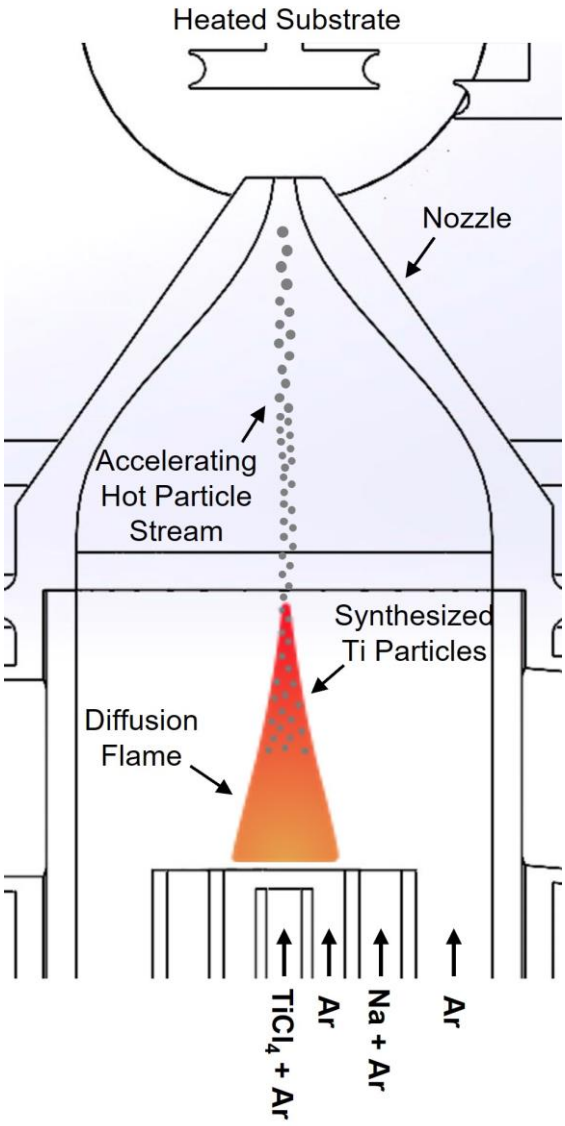

Fig. 8.3. Cross sectional view of the FLAMe system and illustration of the FLAMe process.

dimensions (ID/OD) are 3.0/4.8, 10.2/12.7, 19.7/22.2, and 34.8/38.1 mm. Due to the hypergolic nature of the sodium-halide chemistry, the inner coflow of Ar is necessary to prevent particle formation and clogging on the central tube. The outer coflow of Ar is used to control the reaction temperature and velocity at the nozzle exit. A stable uniform flow field is established in the three outermost tubes using honeycomb flow straighteners. The central halide tube is at least twice the length necessary for fully developed laminar flow.

All flow rates of Ar are controlled using rotameters (Matheson model FM-1050 series). Because $TiCl_4$ is liquid at room temperature, it is supplies via a bubbler with Ar as the carrier gas. The concentration of $TiCl_4$ in the gas phase is obtained by measuring the liquid temperature and assuming saturation. Na is supplied using a Na pump and a vaporizer tube with Ar as the carrier gas. The flow rate of liquid Na is set using the velocity of the Na pump and the concentration of Na in the vapor phase is obtained using the Ar flowrate through the vaporizer and ensuring that the vaporizer temperature is above the saturation temperature. The temperature of the tubes downstream of the $TiCl_4$ bubbler and Na vaporizer are heated above the saturation temperature to avoid reactant condensation.

Once a flame is ignited, the synthesized particles travel downstream and are accelerated using a converging nozzle. The contour of the nozzle contraction is designed using the equation driven spline of refs. [208,209] for a wind tunnel contraction to maintain a uniform velocity profile and prevent boundary layer separation. The nozzle exit diameter is 1.6 mm. The accelerated particle stream is then impacted onto a heated substrate. Deposition is ensured by maintain a vacuum (10 – 76 torr) in the deposition chamber to decrease the mean free path and increase the Stokes number. Three deposition plates are used to find the optimal impaction length ratios (i.e., substrate standoff distance to nozzle exit diameter). The three length ratios used in this work are 1.5, 3, and 4.5. The NaCl byproduct is maintained in the gas phase in the nozzle, owing to the high reaction temperature, and during deposition, owing to the heated substrate and the chamber being maintained under vacuum, which reduces the vapor pressure.

8.4 Experimental methods

In this work, a thin layer of Ti is deposited onto a substrate using a Na/$TiCl_4$/Ar flame, without the vacuum chamber and nozzle section attached, to show proof-of-concept for deposition of Ti with minimal NaCl contamination. The experimental conditions are seen in Table 8.3, where X denotes molar concentration and $\dot{m}$ mass flow rate. The subscripts 1-4 denote the burner tubes in Fig. 8.3 from innermost to outermost.

Table 8.3
Experimental conditions.

X_{TiCl4}	X_{Na}	$\dot{m}_{TiCl4}$ [mg/s]	$\dot{m}_{Na}$ [mg/s]	$\dot{m}_{Ar1}$ [mg/s]	$\dot{m}_{Ar2}$ [mg/s]	$\dot{m}_{Ar3}$ [mg/s]	$\dot{m}_{Ar4}$ [mg/s]
0.6	0.08	1.1	1.8	0.15	4.0	36.4	123

The substrate used is a 6.35 mm OD/4.57 mm ID Inconel 600 tube with composition shown in Table 8.4. The substrate is heated to 1050 °C (±10%) using a propane torch to thermophoretically

Table 8.4
Composition of Inconel 600 tube

Element	wt%
Ni	72 Min
Cr	14-17
Fe	6-10
C	0.05-1.5
Mn	1 Max
Si	0.5 Max
Cu	0.5 Max
Al	0.3 Max
Ti	0.3 Max
B	0.006 Max
P	0.015 Max
S	0.015 Max

sample particles and avoid salt condensation/contamination during the deposition process. The substrate is thrust into the center of the flame and held in place for approximately 3 seconds (±1 s) before removal.

After sampling the flame, the substrates were placed on an aluminum SEM mount with adhesive carbon tape, and then analyzed for Ti and NaCl using an Environmental Scanning Electron Microscope (ESEM).

8.5 Results & Discussion

Figure 8.4 shows the typical topography of a sample. The pattern on the tube should be indicative of the cross-sectional structure of the flame (i.e., Na as the outer reactant, $TiCl_4$ as the inner reactant, and the products Ti and NaCl at the reaction zone). Owing to the high temperate of the flame and the substrate, NaCl should remain in the gas phase. Thus, the thin region outlined in Fig

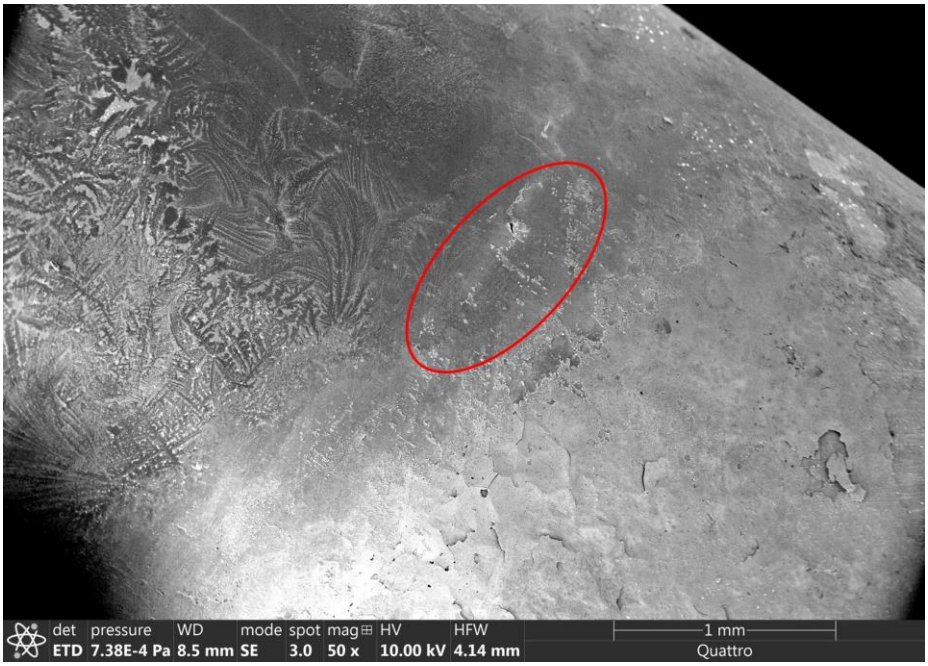

Fig. 8.4. ESEM image of the typical topography of a sample. The red oval denotes the region that may be Ti-rich.

8.4 should be where Ti was deposited, while the upper left and lower right regions relative to that are the regions where Na and TiCl4 flowed over the substrate, respectively.

Figure 8.5a shows a zoomed-in ESEM image of the topography of the proposed Ti-rich region. Using the ESEM, an Energy-dispersive X-ray spectroscopy (EDX) line spectrum can be obtained through the proposed Ti-rich region to probe the presence of Ti and NaCl. Figure 8.5b shows the normalized EDX signal for Ti and Cl as a function of distance along the line shown in Fig. 8.5a. The EDX signal shows that the detected Ti increases by a factor of 5 in the proposed Ti-rich zone, indicating that the zone indeed contains an increased concentration of Ti. The Cl signal is small and remains relatively constant, indicating that there is not substantial NaCl deposition/contamination. Owing to stoichiometry (i.e., 4 moles of NaCl are produced for every mole of Ti), if NaCl was present, the signal from Cl would be substantially higher than seen in Fig. 8.5b. The sharp drop in the Ti signal in Fig. 8.5b is owing to flaking of deposit or substrate surface.

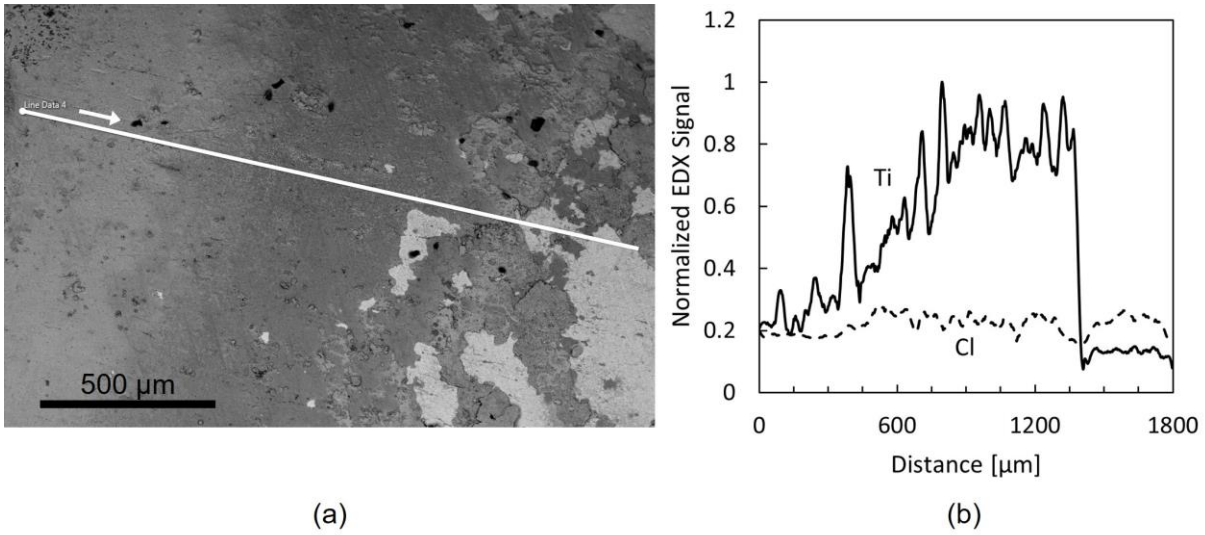

Fig. 8.5. (**a**) ESEM image of the topography of the assumed Ti-rich region and (**b**) normalized EDX signal along the line denoted in (a) for Ti and Cl.

Figure 8.6 shows a zoomed in ESEM image of the Ti-rich region identified in Fig. 8.5. Fig. 8.6 shows two distinct structures.

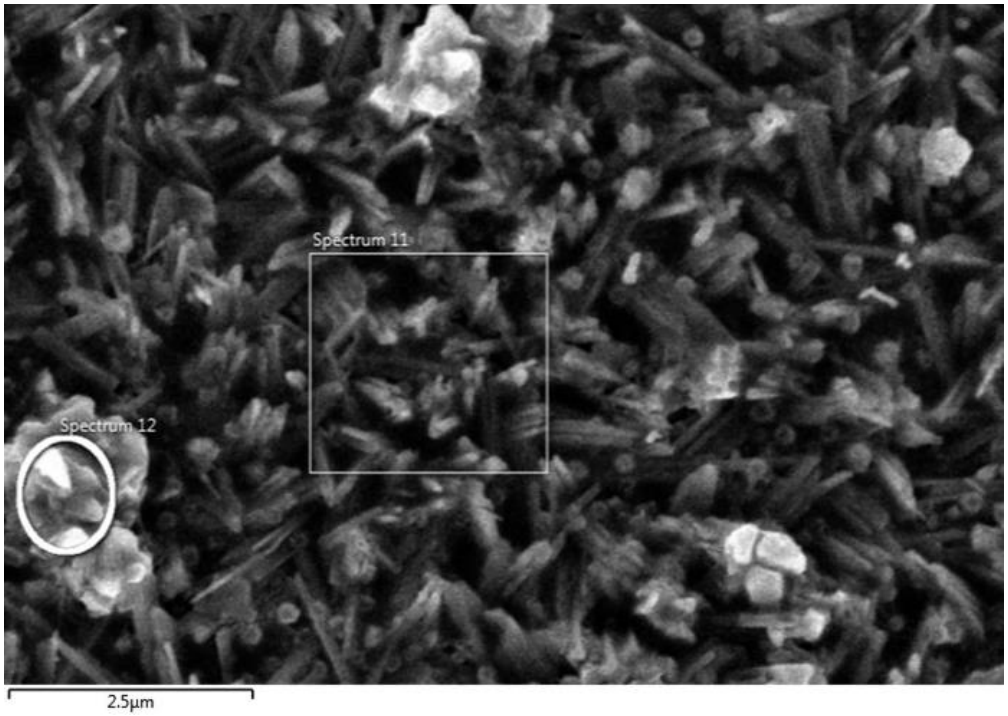

Fig. 8.6. Zoomed in ESEM image of the Ti-rich region.

The composition of the two structures in Fig. 8.6 (indicated by the regions Spectrum 11 and Spectrum 12) are analyzed using EDX. The EDX spectrum of region 12 and the corresponding composition are shown in Fig. 8.7. Figure 8.7 shows that the Na and Cl content in region 12 are very small, suggesting that there is little NaCl. Region 12, however, has a very high content of Fe, O, and Cr, suggesting that this structure is primarily composed of contamination from iron and chromium oxides. This contamination is likely from oxidation of the Inconel 600 after it was heated by the propane torch in air, or from the stainless-steel tubes in the burner [210-211]. There is also a small amount of Ni, as expected owing to the composition of the substrate and beam penetration. The Ti wt% is not significant, but it is much greater than that of the raw substrate material, suggesting that some Ti was deposited on the surface in this location.

The EDX spectra of region 11, shown in Fig. 8.8, shows little Cl, indicating that there is minimal NaCl. However, the concentration of Na is significantly higher than seen in region 11. This is

attributed to NaOH, where Na may have condensed onto the surface as the substrate was pulled from the flame, and then oxidized. There is also very high content of Cr, Ti, and O. The high Ti concentration (three orders of magnitude greater than the raw substrate material) suggest that this structure is a thin layer of deposited titanium that has oxidized [212]. The high Cr content can be attribute to a layer of chromium oxide that formed on the surface of the tube while it was heated by the propane torch in air [210-211]. A relatively small amount of Ni and Fe are also present from the Inconel 600.

Figures 8.6, 8.7, and 8.9 show evidence that a thin layer of synthesized Ti was deposited onto a surface using the sodium/halide FLAMe synthesis chemistry with minimal NaCl contamination. Owing to the thin layer and presence of oxygen in the ambient, the Ti layer oxidized.

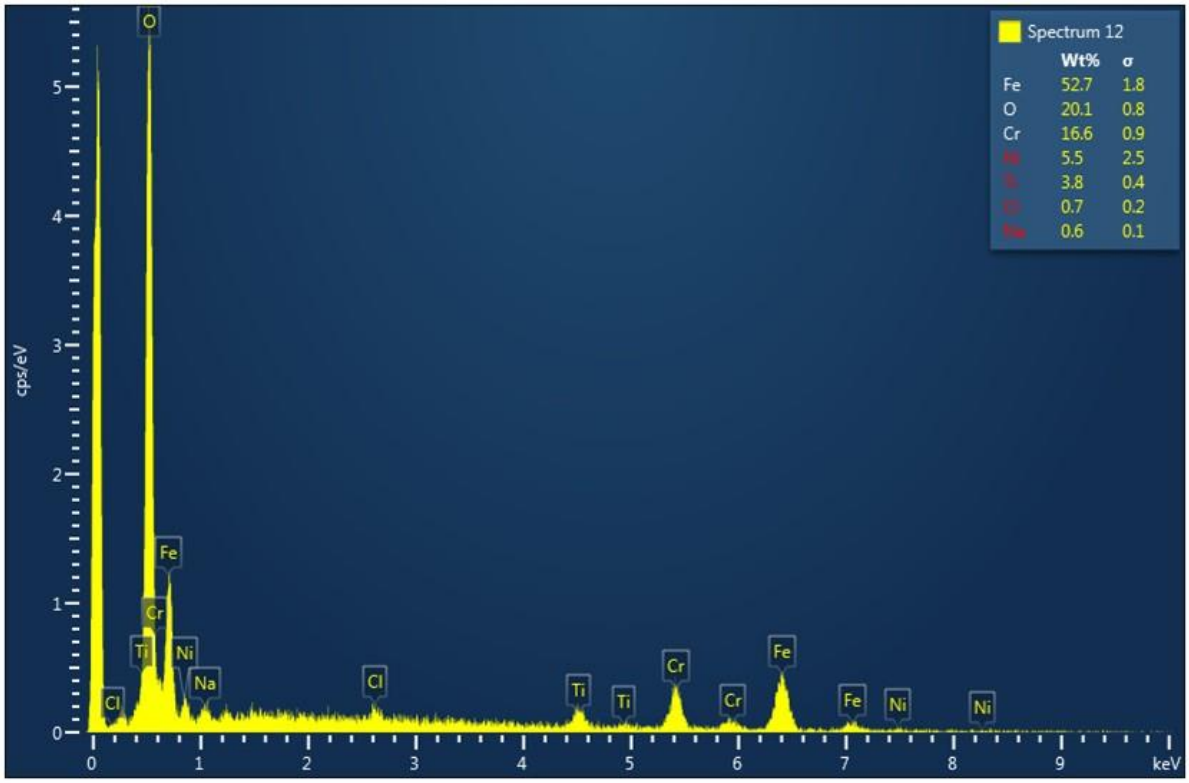

Fig. 8.7. EDX spectrum from the region “Spectrum 12” outlined in Fig. 8.6.

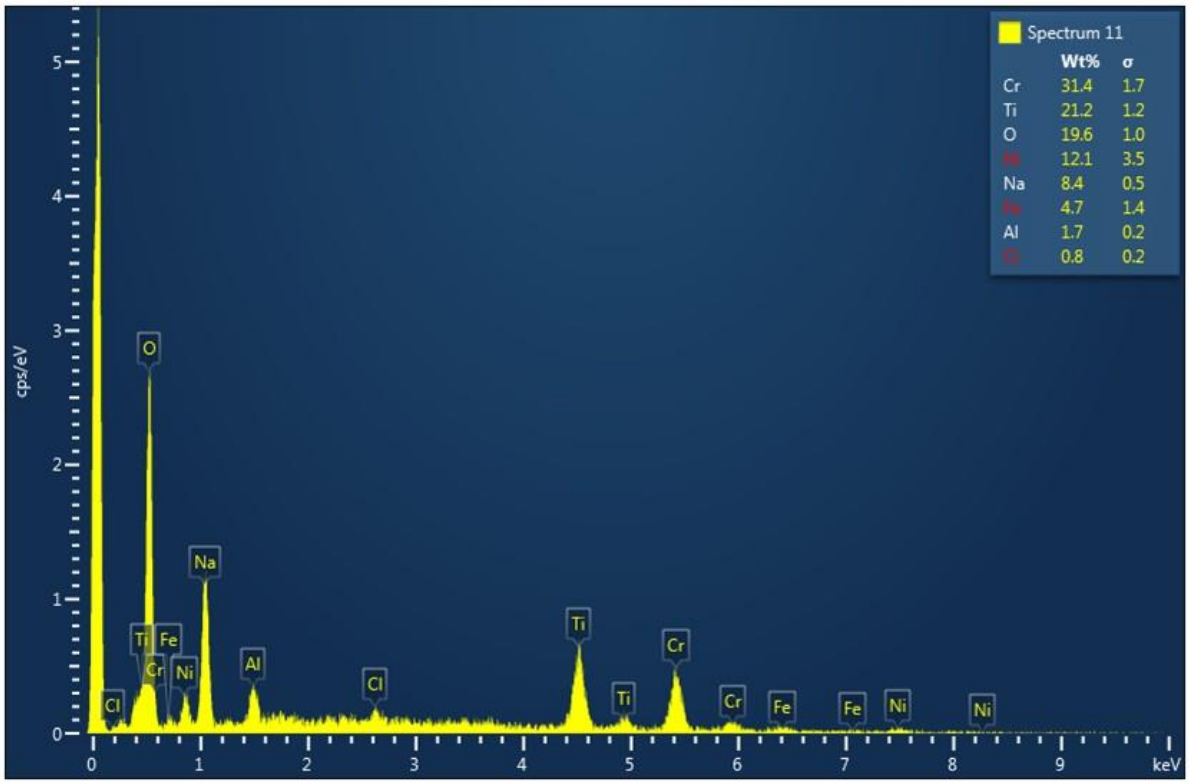

Fig. 8.8. EDX spectrum from the region “Spectrum 11” outlined in Fig. 8.6.

8.6 Conclusions

In this work, evidence for the deposition of a thin layer of synthesized titanium particles onto a substrate with minimal NaCl contamination using the sodium/halide FLAMe synthesis chemistry was presented. Based on the results, more research on FLame-Assisted Additive Manufacturing is needed, as the method holds promise as a new AM method for producing high temperature materials such as titanium. Further research must be conducted to investigate the feasibility of using a converging nozzle to create a high velocity particle stream that can deposit particles and create a dense line deposit. Furthermore, a second, or even third, material must be added to investigate the feasibility of producing and depositing alloys and ceramics.

Chapter 9: Summary and recommendations for future work

9.1 Summary of results

This work advances the fundamental scientific understanding of the effects of particle formation and thermal radiation in laminar diffusion flames by conducting three unique experiments with applications to energy and/or materials. The results of this work are summarized below.

1) The impact of central oxygen enrichment on thermal radiation from laminar tri-coflow methane and ethylene diffusion flames was studied to determine if central oxygen could be used to enhance/control radiant emissions from methane flames for applications to natural gas combustion. It was found that under any condition, central oxygen alone did not increase radiant emission from the methane flames to that of a fuel with a higher propensity for soot formation such as ethylene. However, this work showed that a small amount of central oxygen could significantly enhance soot formation in methane flames and elucidated the importance of soot and gas emissivity on flame radiation. Based on these results, the effect of toluene dopant on thermal radiation from laminar tri-coflow methane diffusion flames with central oxygen was studied. It was found that a small amount of central oxygen and only 2% toluene dopant by volume could increase radiant emission from a normal coflow methane flame by 110%, to levels greater than that of a fuel with a higher propensity for soot formation such as ethylene. These results show that the radiant emission from methane (i.e., natural gas) flames can be controlled or "designed" such that natural gas can be a promising drop-in replacement for more polluting fossil fuels (e.g., coal or oil) using a combination of central oxygen enrichment and fuel additives.
2) Spherical diffusion flames in microgravity were investigated as part of the experiment Flame Design, which is part of the NASA project Advanced Combustion via Microgravity Experiments (ACME), to optimize oxygen enriched combustion for applications to carbon

capture and storage. The fundamental dynamics of spherical diffusion flames in microgravity were elucidated. It was shown that atmospheric pressure ethylene microgravity spherical diffusion flames radiatively extinguish at a critical point, defined by a burner reactant-based mass flux (0.2 g/m^2-s for ethylene and 0.68 g/m^2-s for oxygen) and peak (i.e., flame) temperature (1130 K). A simple equation to estimate flame size at extinction was derived using only the burner reactant mass flow rate. Two fundamental mechanisms for flame growth were identified: 1) the intrinsic growth of a diffusion limited system as it approaches steady-state and 2) radiation-induced growth that is a result of the temperature dependence of transport properties. Furthermore, the existence of steady-state microgravity spherical diffusion flames in an infinite domain in the presence of radiation heat loss was validated. A simple analytical model was developed that allows one to identify conditions that will lead to a steady-state spherical diffusion flame. The fundamental oxidation pathway for ultra-low strain ethylene diffusion flames at high and low temperature was also elucidated.

3) Proof-of-concept for synthesis and deposition of a thin layer of Ti with minimal NaCl contamination using the sodium/metal halide combustion synthesis chemistry was demonstrated. This work shows great promise for the feasibility of a novel additive manufacturing method capable of fabricating components of refractory metals, alloys, multi-principal element alloys, and FGMs with locally tailored properties.

9.2 Recommendations for future work

Based on the results and conclusions presented in this dissertation, some promising future research projects are identified and listed below:

9.2.1 Tri-coflow diffusion flames

1) Toluene showed great promise as a method of increasing radiation heat transfer from methane tri-coflow flames. Many other aromatic fuels can be tested as fuel additives in these methane tri-coflow flames to identify which additive gives the best radiative performance. Furthermore, an economic analysis can then be performed to find the most efficient (on a cost and performance basis) fuel additive for increasing the radiative performance of natural gas combustion.
2) The effectiveness of using central oxygen enrichment and fuel additives in a laminar tri-coflow flame configuration on increasing thermal radiation can be studied using commercial natural gas as the fuel. The results can be compared to the results of the methane tri-coflow flames presented herein. Natural gas often contains small concentrations of species with a higher propensity for soot formation than methane (i.e., ethane), which may slightly increase its radiative performance compared to the flames presented herein.
3) Most practical combustion systems use turbulent diffusion flames. Thus, it would be practical to investigate the scalability of using the tri-coflow flame configuration with central oxygen to increase radiation heat transfer in turbulent diffusion flames.

9.2.2 Spherical diffusion flames in microgravity

1) Modelling the chemical kinetics of spherical diffusion flames in microgravity has shown that the kinetic structure of flames at ultra-low strain is different, and changes significantly with temperature. A detailed analysis of these results could show why all ethylene microgravity spherical diffusion flames at 1 bar extinguish at a critical extinction temperature. Additionally, the chemical reactions that are shown to be important in the

vicinity of extinction are known to be highly pressure dependent. Modelling these flames at higher pressure has shown that higher pressure allows the flames to survive at lower temperatures, indicative of warm flames, and possibly even cool flames. Further studies of the chemical kinetics in microgravity flames, particularly at high pressure, could elucidate an entirely new understanding of low temperature flame chemistry.

2) Sooting limits for ethylene spherical diffusion flames in microgravity can be identified using the data acquired aboard the ISS. A fundamental understanding of the effects of flame structure on soot formation in these flames can lead to the optimization of oxygen-enriched combustion for applications to facilitate carbon capture and storage.
3) Radiative extinction of spherical diffusion flames in microgravity could be studied for a wide variety of fuels to elucidate if the critical extinction point shown here for ethylene is universal, or fuel dependent. This theory could also be expanded to microgravity droplet and candle flames.
4) Flame Design serendipitously observed soot super-agglomerates in normal ethylene microgravity spherical diffusion flames. On Earth, such super-agglomerates are typically only observed in wildfires. Their formation mechanism is not well-understood and is extremely difficult to study due to the danger associated with wildfires and their inability to be replicated on a laboratory scale. However, one could study these flames in microgravity using normal spherical diffusion flames in microgravity with a variety of fuels with various propensities for soot formation to gain a fundamental understanding of the formation mechanisms of soot super-agglomerates.
5) Understanding the effect of soot and gaseous radiation reabsorption is critical for accurate modelling of large soot laden flames such as wildfires and industrial combustion processes.

Spherical flames in microgravity give a unique opportunity to study soot and gaseous radiation under optically thick conditions. Furthermore, in the ACME experiments, spherical flames have shown to exhibit diminishing gaseous radiation with time due to optically thick conditions, demonstrating a unique structure of radiation reabsorption in flames.

9.2.3 Flame-Assisted Additive Manufacturing

1) Deposition of a dense line deposit using the converging nozzle and deposition chamber must be achieved. Furthermore, a detailed systematic study on the microstructure and porosity of titanium deposits produced via FLAMe could help optimize process parameters for improved deposition and material properties.
2) Now that proof-of-concept of deposition has been demonstrated for the FLAMe using titanium, one can demonstrate deposition of more difficult to deposit materials such as refractory metals or a refractory alloy.
3) One of the most attractive aspects of the FLAMe process is the potential for the fabrication of functionally graded materials (FGMs). One could fabricate functionally graded materials using the FLAMe process and develop in-situ characterization methods for material properties such as density and hardness. The data acquired could then be used in a machine learning application, where the system could design and locally tailor material properties based on user inputs and in-situ feedback of the material properties.

References

[1] S. Brookes, J. Moss, Predictions of Soot and Thermal Radiation Properties in Confined Turbulent Jet Diffusion Flames, Combust. Flame 116 (1999) 486–503.

[2] C.J. Unrau, R.L. Axelbaum, P. Biswas, P. Fraundorf, Synthesis of single-walled carbon nanotubes in oxy-fuel inverse diffusion flames with online diagnostics, Proc. Combust. Inst. 31 (2007) 1865-1872.

[3] W. Merchan-Merchan, A.V. Saveliev, L. Kennedy, W.C. Jiminez, Combustion synthesis of carbon nanotubes and related nanostructures, Progress in Energy and Combustion Science 36 (2010) 696-727.

[4] M.T. Zainal, M.F. Mohd Yasin, M. Addul Wahid, M. Mohd Sies, A Flame Structure Approach for Controlling Carbon Nanotube Growth in Flame Synthesis, Combust. Sci. Tech. 193 (2021) 1326-1342.

[5] J.E. Madero, J. Li, K.Y. Shen, J. Wojtak, R.L. Axelbaum, An approach to low-temperature flame spray pyrolysis for the synthesis of temperature-sensitive materials: Application to Li1.2Mn0.54Ni0.13Co0.13O2, Applications in Energy and Combustion Science 5 (2021) 100020.

[6] A. Naseri, M.J. Thomson, Development of a numerical model to simulate carbon black synthesis and predict the aggregate structure in flow reactors, Combust. Flame 207 (2019) 314-326.

[7] A. Khitab, S. Ahmad, M.J. Munir, S.M.S. Kazmi, T. Arshad, R.A. Khushnood, Synthesis and applications of nano titania particles: A review, Review on Advanced Materials Science, 53 (2018) 90-105.

[8] F. Meierhofer, U. Fritsching, Synthesis of Metal Oxide Nanoparticles in Flame Sprays: Review on Process Technology, Modeling, and Diagnostics, Energy Fuels 35 (2021) 5495-5537.

[9] H. Lund, B.V. Mathiesen, Energy System Analysis of 100% renewable energy systems - The case of Denmark in years 2030 and 2050, Energy 34 (2009) 524-531.

[10] D. Connolly, H. Lund, B.V. Mathiesen, M. Leahy, The first step towards a 100% renewable energy-system for Ireland, Applied Energy 88 (2011) 502-507.

[11] M.Z. Jacobson, M.A. Delucchi, Providing all global energy with wind, water, and solar power, Part I: Technologies, energy resources, quantities and areas of infrastructure, and materials, Energy Policy 39 (2011) 1154-1169.

[12] M.A. Delucchi, M.Z. Jacobson, Providing all global energy with wind, water, and solar power, Part II: Reliability, system and transmission costs, and policies, Energy Policy 39 (2011) 1170-1190.

[13] I.G. Mason, S.C. Page, A.G. Williamson, Scenarios for a sustainable energy system in the Åland Islands in 2030, Energy Policy 60 (2013) 324-333.

[14] B.V. Mathiesen, H. Lund, D. Connolly, H. Wenzel, P.A. Ostergaard, M. Moller, S. Nielsen, I. Ridjan, P. Karnoe, K. Sperling, F.K. Hvelplund, Smart Energy Systems for coherent 100% renewable energy and transport solutions, Applied Energy 145 (2015) 139-154.

[15] J. Rogelj, M. Schaeffer, M. Meinhausen, R. Knutti, J. Alcamo, K. Riahi, W. Hare, Zero emission targets as long-term global goals for climate protection, Environmental Research Letters 10 (2015) 105007.

[16] D.F. Dominikovic, I. Bacekovic, B. Cosic, G. Krajacic, T. Puksec, N. Duic, N. Markovska, Zero carbon energy system of South East Europe in 2050, Applied Energy 184 (2016) 1517-1528.

[17] M. Child, C. Breyer, Vision and initial feasibility analysis of a recarbonised Finnish energy system for 2050, Renewable and Sustainable Energy Reviews 66 (2016) 517-536.

[18] M. Child, A. Nordling, C. Breyer, Scenarios for a sustainable energy system in the Åland Islands in 2030, Energy Conversion and Management 137 (2017) 49-60.

[19] J. Wang, Y. Zong, S. You, C. Traeholt, A review of Danish integrated multi-energy system flexibility options for high wind power penetration, Clean Energy 1 (2017) 23-35.

[20] P. Pinson, L. Mitridati, C. Ordoudis, J. Ostergaard, Towards Fully Renewable Energy Systems: Experience and Trends in Denmark, CSEE Journal of Power and Energy Systems 3 (2017) 2096-0042.

[21] B.D. Solomon, A.M. Wellstead, Shooting for Perfection: Hawaii's Goal of 100% Renewable Energy Use, Case Studies in the Environment 2 (2018) 1-9.

[22] H. Meschede, M. Child, C. Breyer, Assessment of sustainable energy system configuration for a small Canary Island in 2030, Energy Conversion and Management 165 (2018) 363-372.

[23] A.M. Elshurafa, H.M. Farag, D.A. Hobbs, Blind spots in energy transition policy: Case studies from Germany and USA, Energy Reports 5 (2019) 20-28.

[24] K. Hansen, B.V. Mathiesen, I.R. Skov, Full energy system transition towards 100% renewable energy in Germany in 2050, Renewable and Sustainable Energy Reviews 102 (2019) 1-13.

[25] K. Hansen, C. Breyer, H. Lund, Status and perspectives on 100% renewable energy systems, Energy 175 (2019) 471-480.

[26] H.L. van Soest, M.G.J. den Elzen, D.P. van Vuuren, Net-zero emission targets for major emitting countries consistent with the Paris Agreement, Nature Communications 12 (2021) 2140.

[27] T. Trainer, Can Australia run on renewable energy? The negative case, Energy Policy 50 (2012) 306-314.

[28] T. Trainer, Can Europe run on renewable energy? The negative case, Energy Policy 63 (2013) 845-850.

[29] T. Trainer, 100% Renewable supply? Comments on the reply by Jacobson and Delucchi to the critique by Trainer, Energy Policy 57 (2013) 634-640.

[30] C.T.M. Clack, S.A. Qvist, J. Apt, M. Bazilian, A.R. Brandt, K. Caldeira, S.J. Davis, V. Diakov, M.A. Handschy, P.D.H. Hines, P. Jaramillo, D.M. Kammen, J.C.S. Long, M.G. Morgan, A. Reed, V. Sivaram, J. Sweeney, G.R. Tynan, D.G. Victor, J.P. Weyeant, J.F. Whitacre, Evaluation of a proposal for reliable low-cost grid power with 100% wind, water, and solar, Proceedings of the National Academy of Sciences of the United States of America 114 (2017) 6722-6727.

[31] T. Trainer, Some problems in storing renewable energy, Energy Policy 110 (2017) 386-393.

[32] B.P. Heard, B.W. Brook, T.M.L. Wigley, C.J.A. Bradshaw, Burden of proof: A comprehensive review of the feasibility of 100% renewable-electricity system, Renewable and Sustainable Energy Reviews 76 (2017) 1122-1133.

[33] A. Harjanne, J.M. Korhonen, Abandoning the concept of renewable energy, Energy Policy 127 (2019) 330-340.

[34] W. Zappa, M. Junginger, M. van den Broek, Is a 100% renewable European power system feasible by 2050?, Applied Energy 233-234 (2019) 1027-1050.

[35] S. Nalley, A. LaRose, International energy outlook 2021 (IEO2021), U.S. Energy Information Administration (2021).

[36] International Energy Agency (IEA), available at <https://www.iea.org/fuels-and-technologies/renewables>.

[37] A. Mikhaylov, Geothermal Energy Development in Iceland, International Journal of Energy Economics and Policy 10 (2020) 31-35.

[38] R.L. Axelbaum, P.H. Irace, Why Was ERCOT's CEO Bill Magness Terminated? A Lesson for Utility Executives, Real Clear Energy, March 16, 2021.

[39] P.Y. Oei, H. Hermann, P. Herpich, U. Holtemoller, B. Lunenburger, C. Schult, Coal phase-out in Germany - Implications and policies for affected regions, Energy 196 (2020) 117004.

[40] V. Vivoda, How disrupted Russian gas supplies will hit global and Australian prices, The Conversation, March 1, 2022.

[41] Trading Economics, available at <https://tradingeconomics.com/commodity/natural-gas>.

[42] B.J.P. Buhre, L.K. Elliott, C.D. Sheng, R.P. Gupta, T.F. Wall, Oxy-fuel combustion technology for coal-fired power generation, Progress in Energy and Combustion Science 31 (2005) 283-307.

[43] S.S. Daood, W. Nimmo, P. Edge, B.M. Gibbs, Deep-staged, oxygen enriched combustion of coal, Fuel 101 (2012) 187-196.

[44] F. Xia, Z. Yang, A. Adeosun, A. Gopan, B.M. Kumfer, R.L. Axelbaum, Pressurized oxy-combustion with low flue gas recycle: Computational fluid dynamic simulations of radiant boilers, Fuel 181 (2016) 1170-1178.

[45] S.A. Hume, Z. Yang, B.M. Kumfer, R.L. Axelbaum, B. Dhungel, J.D. Slater, R.S. Panesar, P.J. Melling, Improving Flexibility and Performance of Staged Pressurized Oxy-Combustion, 14th International Conference on Greenhouse Gas Control Technologies (2018), Melbourne, Australia.

[46] Z. Yang, D. Khatri, P. Verma, T. Li, A. Adeosun, B.M. Kumfer, R.L. Axelbaum, Experimental study and demonstration of pilot-scale, dry feed, oxy-coal combustion under pressure, Applied Energy 285 (2021) 116367.

[47] F. Normann, K. Andersson, B. Leckner, F. Johnson, Emission control of nitrogen oxides in the oxy-fuel process, Progress in Energy and Combustion Science 35 (2009) 385-397.

[48] Z. ur Rahman, J. Zhang, L. Zhang, X. Wang, Z. Yang, H. Tan, R.L. Axelbaum, A kinetic evaluation and optimization study on NOx reduction by reburning under pressurized oxy-combustion, Journal of Environmental Management 290 (2021) 112690.

[49] R. Allam, S. Martin, B. Forrest, J. Fetvedt, X. Lu, D. Freed, G.W. Brown Jr., T. Sasaki, M. Itoh, J. Manning, Demonstration of the Allam Cycle: An update on the development status of a high efficiency supercritical carbon dioxide power process employing full carbon capture, Energy Procedia 114 (2017) 5948-5966.

[50] L.M. Luo, Z.H. Zhao, G. Yao, Y.C. Wu, Recent progress on preparation routes and performance evaluation of ODS/CDS-W alloys for plasma facing materials in fusion devices, Journal of Nuclear Materials 548 (2021) 152857.

[51] D. Pierce, A. Haynes, J. Hughes, R. Graves, P. Maziasz, G. Muralidharan, A. Shyam, B. Wang, R. England, C. Daniel, High temperature materials for heavy duty diesel engines: Historical and future trends, Progress in Materials Science 103 (2019) 109-179.

[52] P.H. Irace, A. Gopan, R.L. Axelbaum, An investigation of thermal radiation from laminar diffusion flames in a tri-coflow burner with central oxygen, Combust. Flame 2021 (submitted).

[53] P.H. Irace, R.L. Axelbaum, Effect of toluene dopant on thermal radiation from laminar tri-coflow methane diffusion flames with central oxygen, Proc. Combust. Inst. 2022 (submitted).

[54] P.H. Irace, H.J. Lee, K. Waddell, L. Tan, D.P. Stocker, P.B. Sunderland, R.L. Axelbaum, Observations of long duration microgravity spherical diffusion flames aboard the International Space Station, Combustion and Flame 229 (2021) 111373.

[55] P.H. Irace, K.A. Waddell, D. Constales, P.B. Sunderland, R.L. Axelbaum, Critical temperature and reactant mass flux for radiative extinction of ethylene microgravity spherical diffusion flames at 1 bar, Proc. Combust. Inst. 2022 (submitted).

[56] P.H. Irace, K.A. Waddell, D. Constales, G. Yablonsky, M. Kim, P.B. Sunderland, R.L. Axelbaum, On the existence of steady state gaseous microgravity spherical diffusion flames in the presence of radiation heat loss, Proc. Combust. Inst. 2022 (submitted).

[57] J.P. Gore, G.M. Faeth, D. Evans, D.B. Pfenning, Structure and radiation properties of large-scale natural gas/air diffusion flames, Fire and Materials 10 (1986) 161-169.

[58] C.K. Law, Combustion Physics, Cambridge University Press, 2006.

[59] S.S. Hwang, J.P. Gore, Characteristics of combustion and radiation heat transfer of an oxygen-enhanced flame burner, Proc. Inst. Mech. Eng., Part A: J. Power Energy 216 (2002) 379-386.

[60] C.E. Baukal, Oxygen-Enhanced Combustion, 2nd ed., CRC Press, 2013.

[61] S. Iuliis, M. Barbini, S. Benecchi, F. Cignoli, G. Zizak, Determination of the Soot Volume Fraction in an Ethylene Diffusion Flame by Multiwavelength Analysis of Soot Radiation, Combust. Flame 115 (1998) 253-261.

[62] C.R. Shaddix, T.C. Williams, The Effect of Oxygen Enrichment on Soot Formation and Thermal Radiation in Turbulent, Non-Premixed Methane Flames, Proc. Combust. Inst. 36 (2017) 4051–4059.

[63] M. Bidi, R. Hosseini, M.R.H. Nobari, Numerical analysis of methane–air combustion considering radiation effect, Energy Conversion and Management 49 (2008) 3634-3647.

[64] M. Ditaranto, T. Oppelt, Radiative heat flux characteristics of methane flames in oxy-fuel atmospheres, Experimental Thermal and Fluid Science 35 (2011) 1343-1350.

[65] Z. Sun, B. Dally, Z. Alwahabi, G. Nathan, The effect of oxygen concentration in the co-flow of laminar ethylene diffusion flames, Combust. Flame 211 (2020) 96-111.

[66] W.H. Giedt, Principles of engineering heat transfer, Van Nostrand, 1957.

[67] C.L. Tien, Thermal Radiation Properties of Gases, Advances in Heat Transfer 5 (1968) 253-321.

[68] A.F. Mills, C.F.M. Coimbra, Heat Transfer, 3rd ed., Temporal Publishing, 2016.

[69] J.R. Howell, M.P. Mengüç, K. Daun, R. Siegel, Thermal Radiation Heat Transfer, 7th ed., CRC Press, 2020.

[70] M.F. Modest, S. Mazumder, Radiative Heat Transfer, 4th ed., Academic Press, 2021.

[71] H.C. Hottel, Chapter 4, Radiant-heat transmission, in: W.H. MacAdams (Ed.), Heat Transmission, McGraw-Hill, New York, 1954.

[72] D.K. Edwards, A. Balakrishnan, Thermal radiation by combustion gases, Int. J. Heat Mass Transfer 16 (1973) 25–40.

[73] D.K. Edwards, Molecular gas band radiation, Adv. Heat Transfer 12 (1976) 115–193.

[74] A. Coppalle, P. Vervisch, The Total Emissivities of High-Temperature Flames, Combust. Flame 49 (1983) 101-108.

[75] K. Lee, C.M. Megaridis, S. Zelepouga, A.V. Saveliev, L.A. Kennedy, O. Charon, F. Ammouri, Soot Formation Effects of Oxygen Concentration in the Oxidizer Stream of Laminar Coannular Nonpremixed Methane/Air Flames, Combust. Flame 121 (2000) 323-333.

[76] S.W. Du, C.P. Yeh, W.H. Chen, C.H. Tsai, J.A. Lucas, Burning characteristics of pulverized coal within blast furnace raceway at various injection operations and ways of oxygen enrichment, Fuel 143 (2015) 98-106.

[77] K. Yamamoto, Y. Isobe, N. Hayashi, H. Yamashita, S.H. Chung, Behaviors of tribrachial edge flames and their interactions in a triple-port burner, Combust. Flame 162 (2015) 1653-1659.

[78] B.M. Kumfer, S.A. Skeen, R.L. Axelbaum, Soot inception limits in laminar diffusion flames with application to oxy-fuel combustion, Combust. Flame 154 (2008) 546-556.

[79] S.S. Krishnan, M.K. Saini, Y. Zheng, J.P. Gore, Radiation Properties of Oxygen-Enhanced Normal and Inverse Diffusion Flames, ASME J. Heat Transfer 134 (2012) 022701.

[80] Y.H. Li, C.Y. Wu, H.T. Lin, J.S. Wu, Experimental and Numerical Study of Oxygen Enrichment on Methane Diffusion Flame in a Triple Port Burner, 25th International Colloquium on the Dynamics of Explosions and Reactive Systems (2015).

[81] K. Yamamoto, M. Takemoto, Measurement of PAH and Soot of Diffusion Flames in a Triple Port Burner, Fuel Processing Technology 107 (2013) 99–106.

[82] Y.R. Sivathanu, J.P. Gore, Effects of gas-band radiation on soot kinetics in laminar methane / air diffusion flames, Combust. Flame 110 (1997) 256-263.

[83] A. Datta, A. Saha, Contributions of Self-Absorption and Soot on Radiation Heat Transfer in a Laminar Methane - Air Diffusion Flame, Proc. Inst. Mech. Eng., Part A: J. Power Energy 221 (2007) 955–970.

[84] H. Guo, J.A. Castillo, P.B. Sunderland, Digital Camera Measurements of Soot Temperature and Soot Volume Fraction in Axisymmetric Flames, Applied Optics 52 (2013) 8040-8047.

[85] G.H. Markstein, Correlations for smoke points and radiant emission of laminar hydrocarbon diffusion flames, Symp. (Int.) Combust. 22 (1989) 363-370.

[86] G.H. Markstein, Relationship between smoke point and radiant emission from buoyant turbulent and laminar diffusion flames, Symp. (Int.) Combust. 20 (1985) 1055-1061.

[87] D.R. Burgess Jr., Thermochemical Data in NIST Chemistry WebBook, NIST Standard Reference Database Number 69, Eds. P.J. Linstrom, W.G. Mallard, National Institute of Standards and Technology, Gaithersburg MD, 20899 (retrieved May 20, 2020).

[88] P. Kuhn, B. Ma, B. Connelly, M. Smooke, M. Long, Soot and Thin-Filament Pyrometry Using a Color Digital Camera, Proc. Combust. Inst. 33 (2011) 743–750.

[89] N.J. Kempema, M.B. Long, Effect of soot self-absorption on color-ratio pyrometry in laminar coflow diffusion flames, Optics Letters 43 (2018) 1103-1106.

[90] B. Ma, M.B. Long, Combined soot optical characterization using 2-D multi-angle light scattering and spectrally resolved line-of-sight attenuation and its implication on soot color-ratio pyrometry, Appl. Phys. B. 117 (2014) 287-303.

[91] F. Cignoli, S.D. Iuliis, V. Manta, G. Zizak, Two-Dimensional Two-Wavelength Emission Technique for Soot Diagnostics, Applied Optics 40 (2001) 5370-5378.

[92] B. Ma, S. Cao, D. Giassi, D.P. Stocker, F. Takahashi, B.A.V. Bennett, M.D. Smooke, M.B. Long, An experimental and computational study of soot formation in a coflow jet flame under microgravity and normal gravity, Proc. Combust. Inst. 35 (2015) 839-846.

[93] D.K. Kim, P.B. Sunderland, Fire ember pyrometry using a color camera, Fire Safety Journal 106 (2019) 88-93.

[94] B. Ma, G. Wang, G. Magnotti, R.S. Barlow, M.B. Long, Intensity-ratio and color-ratio thin-filament pyrometry: Uncertainties and accuracy, Combust. Flame 161 (2014) 908-916.

[95] Y. Matsui, T. Kamimoto, S. Matsuoka, A Study on the Time and Space Resolved Measurement of Flame Temperature and Soot Concentration in a D.I. Diesel Engine by the Two-Color Method, SAE Transactions 88 (1979) 1808-1822.

[96] R.G. Siddall, I.A. McGrath, The Emissivity of Luminous Flames, Symp. (Int.) Combust. 9 (1963) 102-110.

[97] D. Coffin, Decoding Raw Digital Photos in Linux, (2018) https://www.cybercom.net/~dcoffin/dcraw/.

[98] MATLAB, version 9.8.0 (R2020a). Natick, Massachusetts: The MathWorks Inc. (2020).

[99] H. Chang, T.T. Charalampopoulos, Determination of the Wavelength Dependence of Refractive Indices of Flame Soot, Proc. R. Soc. Lond. A 430 (1990) 577–591.

[100] S.A. Zelepouga, A.V. Saveliev, L.A. Kennedy, A.A. Fridman, Relative effect of acetylene and PAHs addition on soot formation in laminar diffusion flames of methane with oxygen and oxygen-enriched air, Combust. Flame 122 (2000) 76-89.

[101] H.S. Hura, I. Glassman, Fuel Oxygen Effects on Soot Formation in Counterflow Diffusion Flames, Combust. Sci. and Tech. 53 (1987) 1-21.

[102] B.H. Chao, R.L. Axelbaum, Triaxial Burke-Schumann Flames with Applications to Flame Synthesis, Combust. Sci. and Tech. 156 (2000) 291–314.

[103] J.D. Felske, C.L. Tien, Calculation of the Emissivity of Luminous Flames, Combust. Sci. Tech. 7 (1973) 25-31.

[104] W.W. Yuen, C.L. Tien, A simple calculation scheme for the luminous-flame emissivity, Symp. (Int.) Combust. 16 (1977) 1481-1487.

[105] P. Verma, Z. Yang, S. Hume, A. Maxson, R.L. Axelbaum, Process design and analysis of a novel carbon-capture-ready process for flexible-load power generation: Modular pressurized air combustion, Energy Conversion and Management 228 (2021) 113638.

[106] C.S. McEnally, L.D. Pfefferle, Soot formation in methane/air nonpremixed flames doped with small quantities of C3 hydrocarbons, Combust. Flame 112 (1998) 545-558.

[107] C.S. McEnally, L.D. Pfefferle, Species and Soot Concentration Measurements in a Methane/Air Nonpremixed Flame Doped With C4 Hydrocarbons, Combust. Flame 115 (1998) 81-92.

[108] J.L. Consalvi, F. Liu, M. Kashif, G. Legros, Numerical study of soot formation in laminar coflow methane/air diffusion flames doped by n-heptane/toluene and iso-octane/toluene blends, Combust. Flame 180 (2017) 167-174.

[109] A. Daca, O.L. Gulder, Soot formation characteristics of diffusion flames of methane doped with toluene and n-heptane at elevated pressures, Proc. Combust. Inst. 36 (2017) 737-744.

[110] M. Gu, F. Liu, J.L. Consalvi, I.L. Gulder, Effects of pressure on soot formation in laminar coflow methane/air diffusion flames doped with n-heptane and toluene between 2 and 8 atm, Proc. Combust. Inst. 38 (2021) 1403-1412.

[111] B.A.V. Bennett, C.s. McEnally, L.D. Pfefferle, M.D. Smooke, Computational and experimental study of axisymmetric coflow partially premixed methane/air flames, Combust. Flame 123 (2000) 522-546.

[112] H.P. Mungekar, A. Atreya, Effect of partial premixing on the sooting structure of methane flames, Combust. Flame 144 (2006) 336-348.

[113] H.P. Mungekar, A. Atreya, Flame Radiation and Soot Emission From Partially Premixed Methane Counterflow Flames, J. Heat Transfer 128 (4) (2006) 361-367.

[114] D.X. Du, R.L. Axelbaum, C.K. Law, The influence of carbon dioxide and oxygen as additives on soot formation in diffusion flames, Proc. Combust. Inst. 23 (1) (1991) 1501-1507.

[115] J. Du, R.L. Axelbaum, The effect of flame structure on soot-particle inception in diffusion flames, Combust. Flame 100 (1995) 367-375.

[116] J. Du, R.L. Axelbaum, The effects of flame structure on extinction of CH4-O2-N2 diffusion flames, Symp. (Int.) Combust. 26 (1996) 1137-1142.

[117] K.C. Lin, G.M. Faeth, Effects of Hydrodynamics on Soot Formation in Laminar Opposed-Jet Diffusion Flames, Journal of Propulsion and Power 12 (1996) 691-698.

[118] K.C. Lin, G.M. Faeth, Structure of laminar permanently blue, opposed-jet ethylene-fueled diffusion flames, Combust. Flame 115 (1998) 468-480.

[119] B.M. Kumfer, S.A. Skeen, R. Chen, R.L. Axelbaum, Measurement and analysis of soot inception limits of oxygen-enriched coflow flames, Combust. Flame, 147 (2006) 233-242.

[120] C. Lou, X. Chen, W. Yan, Y. Tian, B.M. Kumfer, Effect of stoichiometric mixture fraction on soot fraction and emission spectra with application to oxy-combustion, Proc. Combust. Inst. 37 (2019) 4571-4578.

[121] S.A. Skeen, G. Yablonsky, R.L. Axelbaum, Characteristics of non-premixed oxygen-enhanced combustion: I. The presence of appreciable oxygen at the location of maximum temperature, Combust. Flame 156 (2009) 2145-2152.

[122] K.C. Lin, P.B. Sunderland, G.M. Faeth, Soot Nucleation and Growth in Acetylene Air Laminar Coflowing Jet Diffusion Flames, Combust. Flame 104 (1996) 369-375.

[123] G. Sugiyama, Nonluminous diffusion flame of diluted acetylene in oxygen-enriched air, Symp. (Int.) Combust. 25 (1994) 601-608.

[124] P.B. Sunderland, R.L. Axelbaum, D.L. Urban, B.H. Chao, S. Liu, Effects of structure and hydrodynamics on the sooting behavior of spherical microgravity diffusion flames, Combust. Flame 132 (2003) 25-33.

[125] P.B. Sunderland, D.L. Urban, D.P. Stocker, B.H. Chao, R.L. Axelbaum, Sooting Limits of Microgravity Spherical Diffusion Flames in Oxygen-Enriched Air and Diluted Fuel, Combust. Sci. Tech. 176 (2004) 2143-2164.

[126] S.A. Skeen, G. Yablonsky, R.L. Axelbaum, Characteristics of non-premixed oxygen-enhanced combustion: II. Flame structure effects on soot precursor kinetics resulting in soot-free flames, Combust. Flame 157 (2010) 1745-1752.

[127] D.L. Dietrich, J.B. Haggard Jr., F.L. Dryer, V. Nayagam, B.D. Shaw, F.A. Williams, Droplet combustion experiments in spacelab, Symp. (Int.) Combust. 26 (1996) 1201-1207.

[128] D.L. Dietrich, V. Nayagam, M.C. Hicks, P.V. Ferkul, F.L. Dryer, T. Farouk, B.D. Shaw, H.K. Suh, M.Y. Choi, Y.C. Liu, C.T. Avedisian, F.A. Williams, Droplet Combustion Experiments Aboard the International Space Station, Microgravity Science and Technology 26 (2014) 65-76.

[129] B.D. Shaw, ISS Droplet Combustion Experiments - Uncertainties in Droplet Sizes and Burning Rates, Microgravity Science and Technology 26 (2014) 89-99.

[130] Y.C. Liu, Y. Xu, C.T. Avedisian, M.C. Hicks, The effect of support fibers on micro-convection in droplet combustion experiments, Proc. Combust. Inst. 35 (2015) 1709-1716.

[131] V. Nayagam, D.L. Dietrich, M.C. Hicks, F.A. Williams, Cool-flame extinction during n-alkane droplet combustion in microgravity, Combust. Flame 162 (2015) 2140-2147.

[132] D.L. Dietrich, H.D. Ross, Y. Shu, P. Chang, J.S. T'ien, Candle Flames in Non-Buoyant Atmospheres, Combust. Sci. Tech. 156 (2000) 1-24.

[133] S. Tse, D. Zhu, C.J. Sung, Y. Ju, C.K. Law, Microgravity burner-generated spherical diffusion flames: experiment and computation, Combust. Flame 125 (2001) 1265–1278.

[134] E.W. Christiansen, S.D. Tse, C.K. Law, A computational study of oscillatory extinction of spherical diffusion flames, Combust. Flame 134 (2003) 327-337.

[135] M. Chernovsky, A. Atreya, H. Im, Effect of CO2 diluent on fuel versus oxidizer side of spherical diffusion flames in microgravity, Proc. Combust. Inst. 31 (2007) 1005–1013.

[136] K. Santa, B.H. Chao, P.B. Sunderland, D. Urban, D. Stocker, R.L. Axelbaum, Radiative extinction of gaseous spherical diffusion flames in microgravity, Combust. Flame 151 (2007) 665–675.

[137] K.J. Santa, Z. Sun, B.H. Chao, P.B. Sunderland, R.L. Axelbaum, D.L. Urban, D.P. Stocker, Numerical and Experimental Observations of Spherical Diffusion Flames, Combustion Theory and Modelling 11 (2007) 639-652.

[138] S. Tang, M. Chernovsky, H. Im, A. Atreya, A computational study of spherical diffusion flames in microgravity with gas radiation part I: model development and validation, Combust. Flame 157 (2010) 118–126.

[139] S. Tang, H. Im, A. Atreya, A computational study of spherical diffusion flames in microgravity with gas radiation. part II: parametric studies of the diluent effects on flame extinction, Combust. Flame 157 (2010) 127–136.

[140] B.H. Chao, C.K. Law, J.S. T'ien, Structure and extinction of diffusion flames with flame radiation, Symp. (Int.) Combust. 23 (1991) 523-531.

[141] M.K. Rodenhurst, B.H. Chao, P.B. Sunderland, R.L. Axelbaum, Structure and extinction of spherical burner-stabilized diffusion flames that are attached to the burner surface, Combust. Flame 187 (2018) 22-29.

[142] Q. Wang, B.H. Chao, Kinetic and radiative extinctions of spherical burner-stabilized diffusion flames, Combust. Flame, 158 (2011) 1532-1541.

[143] V. Nayagam, D.L. Dietrich, F.A. Williams, Radiative extinction of burner-supported spherical diffusion flames: A scaling analysis, Combust. Flame 205 (2019) 368–370.

[144] K. Mills, M. Matalon, Extinction of spherical diffusion flames in the presence of radiant loss, Symposium (International) on Combustion 27 (2) (1998) 2535-2541.

[145] A. Markan, H.R. Baum, P.B. Sunderland, J.G. Quintiere, J.L. deRis, Transient Ellipsoidal Combustion Model for a Porous Burner in Microgravity, Combust. Flame 212 (2020) 93-106.

[146] Z. Wang, P.B. Sunderland, R.L. Axelbaum, Double blue zones in inverse and normal laminar jet diffusion flames, Combust. Flame 211 (2020) 253-259.

[147] J.D. Maun, P.B. Sunderland, D.L. Urban, Thin-filament pyrometry with a digital still camera, Applied Optics 46 (2007) 483-488.

[148] J. Tinajero, D. Giassi, D. Stocker, M. Long, Experimental Study on the Influence of Gravity on Highly Diluted and Sooting Coflow Flames, The Combustion Institute, 11th U.S. National Combustion Meeting (2019).

[149] D. Giassi, B. Liu, M.B. Long, Use of high dynamic range imaging for quantitative combustion diagnostics, Applied Optics 54 (2015) 4580-4588.

[150] M.B. Long, Optical Multi-channel Analyzer 2 (OMA2) for Mac OS X, (2019) http://oma-x.org/oma2WebPage/index.html

[151] V.R. Lecoustre, P.B. Sunderland, B.H. Chao, R.L. Axelbaum, Modeled quenching limits of spherical hydrogen diffusion flames, Proc. Combust. Inst. 34 (2013) 887-894.

[152] V.R. Lecoustre, P.B. Sunderland, B.H. Chao, R.L. Axelbaum, Numerical investigation of spherical diffusion flames at their sooting limits, Combust. Flame 159 (2012) 194-199.

[153] R.J. Kee, J.F. Grcar, M.D. Smooke, J.A. Miller, E. Meeks, Premix: A FORTRAN Program for Modeling Steady Laminar One-Dimensional Pre-Mixed Flames, Report No. SAND85-8240, Sandia National Laboratories, 1987.

[154] V. Lecoustre, Numerical Investigations of Gaseous Spherical Diffusion Flames, PhD thesis, The University of Maryland, College Park, Maryland, 2009.

[155] U. Mechanism, Chemical-kinetic Mechanisms for Combustion Applications, Mechanical and Aerospace Engineering (Combustion Research), University of California at San Diego, 2014 http://web.eng.ucsd.edu/mae/groups/combustion/mechanism.html.

[156] A. Murty Kanury, Introduction to Combustion Phenomena, Gordon and Breach Science Publishers, New York, 1975.

[157] C.L. Vang, B.D. Shaw, Evaluation of Free-Floating Droplet Acceleration in ISS Droplet Combustion Experiments, Microgravity Science and Technology 32 (2020) 531-543.

[158] K. Mills, M. Matalon, Burner-Generated Spherical Diffusion Flames, Combust. Sci. Tech. 129 (1997) 295-319.

[159] J.S. T'ien, Diffusion flame extinction at small stretch rates: The mechanism of radiative loss, Combust. Flame 65 (1986) 31-34.

[160] A.J. Marchese, F.L. Dryer, The Effect of Non-Luminous Thermal Radiation in Microgravity Droplet Combustion, Combust. Sci. Tech. 124 (1997) 371-402.

[161] A. Kazakov, J. Conley, F.L. Dryer, Detailed modeling of an isolated, ethanol droplet combustion under microgravity conditions, Combust. Flame 134 (2003) 301-314.

[162] T.I. Farouk, F.L. Dryer, On the extinction characteristics of alcohol droplet combustion under microgravity conditions – A numerical study, Combust. Flame 159 (2012) 3208-3223.

[163] X. Yuhao, M.C. Hicks, C.T. Avedisian, The combustion of iso-octane droplets with initial diameters from 0.5 to 5 mm: Effects on burning rate and flame extinction, Proc. Combust. Inst. 36 (2017) 2541-2548.

[164] E.J. Carr, Characteristic time scales for diffusion processes through layers and across interfaces, Physical Review E 97 (2018) 042115.

[165] C.J. Sun, C.J. Sung, H. Wang, C.K. Law, On the structure of nonsooting counterflow ethylene and acetylene diffusion flames, Combust. Flame 107 (1996) 321-335.

[166] J. Hebda, W. Chang, Niobium Alloys and High Temperature Applications, Niobium Science & Technology: Proceedings of the International Symposium Niobium (2001) Orlando, FL.

[167] V.V Satya Prasad, R.G. Baligidad, A.A. Gokhale, Niobium and Other High Temperature Refractory Metals for Aerospace Applications, In N.E. Prasad, R.J.H. Wanhill (Eds.), Aerospace Materials and Material Technologies (2017) Singapore: Springer Science+Business Media, 267-288.

[168] H.K.M. Al-Jothery, T.M.B. Albarody, P.S.M. Yusoff, M.A. Abdullah, A.R. Hussein, A review of ultra-high temperature materials for thermal protection system, IOP Conference Series: Materials Science and Engineering 863 (2020) 012003.

[169] T. Bhardwaj, M. Shukla, C.P. Paul, K.S. Bindra, Direct Energy Deposition - Laser Additive Manufacturing of Titanium-Molybdenum alloy: Parametric studies, microstructure and mechanical properties, Journal of Alloys and Compounds 787 (2019) 1238-1248.

[170] A. Dass, A. Moridi, State of the Art in Directed Energy Deposition: From Additive Manufacturing to Materials Design, Coatings 9 (2019) 418.

[171] X.X. Yao, P. Ge, J.Y. Li, Y.F. Wang, T. Li, W.W. Liu, Z. Zhang, Controlling the solidification process parameters of direct energy deposition additive manufacturing considering laser and powder properties, Computational Materials Science 182 (2020) 109788.

[172] Z. Luo, Y. Zhao, A survey of finite element analysis of temperature and thermal stress fields in powder bed fusion Additive Manufacturing, Additive Manufacturing 21 (2018) 318-332.

[173] A.A. Martin, N.P. Calta, S.A. Khairallah, J. Wang, P.J. Depond, A.Y. Fong, V. Thampy, G.M. Guss, A.M. Kiss, K.H. Stone, C.J. Tassone, J.N. Weker, M.F. Toney, T. van Buuren, M.J. Matthews, Dynamics of pore formation during laser powder bed fusion additive manufacturing, Nature Communications 10 (2019) 1987.

[174] Z. Snow, A.R. Nassar, E.W. Reutzel, Invited Review Article: Review of the formation and impact of flaws in powder bed fusion additive manufacturing, Additive Manufacturing 36 (2020) 101457.

[175] A. Saboori, D. Gallo, S. Biamino, P. Fino, M. Lombardi, An Overview of Additive Manufacturing of Titanium Components by Directed Energy Deposition: Microstructure and Mechanical Properties, Applied Sciences 7 (2017) 883.

[176] A. Bose, C.A. Schuh, J.C. Tobia, N. Tuncer, N.M. Mykulowycz, A. Preston, A.C. Barbati, B. Kernan, M.A. Gibson, D. Krause, T. Brzezinski, J. Schroers, R. Fulop, J.S. Myerberg, M. Sowerbutts, Y.M. Chiang, A.J. Hart, E.M. Sachs, E.E. Lomeli, A.C. Lund, Traditional and additive manufacturing of a new Tungsten heavy alloy alternative, International Journal of Refractory Metals and Hard Materials 73 (2018) 22-28.

[177] H. Dobbelstein, M. Thiele, E. L. Gurevich, E.P. George, A. Ostendorf, Direct Metal Deposition of Refractory High Entropy Alloy MoNbTaW, Physics Procedia 83 (2016) 624-633.

[178] G. Marinelli, F. Martina, H. Lewtas, D. Hancock, S. Ganguly, S. Williams, Functionally graded structures of refractory metals by wire arc additive manufacturing, Science and Technology of Welding and Joining 24 (2019) 495-503.

[179] A. Ivekovic, N. Omidvari, B. Vrancken, K. Lietaert, L. Thijs, K. Vanmeensel, J. Vleugels, J.P. Kruth, Selective laser melting of tungsten and tungsten alloys, International Journal of Refractory Metals & Hard Materials 72 (2018) 27-32.

[180] A. Muller, G. Schlick, R. Neu, C. Anstatt, T. Klimkait, J. Lee, B. Pascher, M. Schmitt, C. Seidel, Additive manufacturing of pure tungsten by means of selective laser beam melting with substrate preheating temperatures up to 1000 °C, Nuclear Materials and Energy 19 (2019) 184-188.

[181] C. Tan, K. Zhou, W. Ma, B. Attard, P. Zhang, T. Kuang, Selective laser melting of high-performance pure tungsten: parameter design, densification behavior and mechanical properties, Science and Technology of Advanced Materials 19 (1) (2018) 370-380.

[182] D. Wang, C. Yu, X. Zhou, J. Ma, W. Liu, Z. Shen, Dense Pure Tungsten Fabricated by Selective Laser Melting, Appl. Sci. 7 (4) (2017) 430.

[183] D.Z. Wang, K.L. Li, C.F. Yu, J. Ma, W. Liu, Z.J. Shen, Cracking Behavior in Additively Manufactured Pure Tungsten, Acta Metallurgica 32 (2019) 127-135.

[184] B. Nie, L. Yang, H. Huang, S. Bai, P. Wan, J. Liu, Femtosecond laser additive manufacturing of iron and tungsten parts, Appl. Phys. A 119 (2015) 1075-1080.

[185] W. Jeong, Y.S. Kwon, D. Kim, Three-dimensional printing of tungsten structures by directed energy deposition, Materials and Manufacturing Processes 34 (2019) 986-992.

[186] M. Guo, D. Gu, L. Xi, H. Zhang, J. Zhang, J. Yang, R. Wang, Selective laser melting additive manufacturing of pure tungsten: Role of volumetric energy density on densification, microstructure and mechanical properties, International Journal of Refractory Metals & Hard Materials 84 (2019) 105025.

[187] D. Gu, D. Dai, W. Chen, H. Chen, Selective Laser Melting Additive Manufacturing of Hard-to-Process Tungsten-Based Alloy Parts with Novel Crystalline Growth Morphology and Enhanced Performance, Journal of Manufacturing Science and Engineering 138 (2016) 081003.

[188] X. Zhou, X. Liu, D. Zhang, Z. Shen, W. Liu, Balling phenomena in selective laser melted tungsten, Journal of Materials Processing Technology 222 (2015) 33-42.

[189] B.E. Carroll, T.A. Palmer, A.M. Beese, Anisotropic Tensile Behavior of Ti–6Al–4V Components Fabricated with Directed Energy Deposition Additive Manufacturing, Acta Materialia 87 (2015) 309–320.

[190] A.J. Sterling, B. Torries, N. Shamsaei, S.M. Thompson, D.W. Seely, Fatigue Behavior and Failure Mechanisms of Direct Laser Deposited Ti–6Al–4V, Materials Science and Engineering: A 655 (2016) 100–112.

[191] S.J. Wolff, S. Lin, E.J. Faierson, W.K. Liu, G.J. Wagner, J. Cao, A Framework to Link Localized Cooling and Properties of Directed Energy Deposition (DED)-Processed Ti-6Al-4V, Acta Materialia 132 (2017) 106–117.

[192] C. Schneider-Maunoury, L. Weiss, P. Acquier, D. Boisselier, P. Laheurte, Functionally graded Ti6Al4V-Mo alloy manufactured with DED-CLAD process, Additive Manufacturing 17 (2017) 55-66.

[193] S. Liu, Y.C. Shin, Additive Manufacturing of Ti6Al4V Alloy: A Review, Materials & Design 164 (2019) 107552.

[194] H.F. Calcote, W. Felder, A New Gas-Phase Combustion Synthesis Process for Pure Metals, Alloys, and Ceramics, Symp. (Int.) Combust. 24 (1992) 1869-1876.

[195] R.L. Axelbaum, S.E. Bates, W.E. Buhro, C. Frey, K.F. Kelton, S.A. Lawton, L.J. Rosen, S.M. Sastry, Wet Chemistry and Combustion Synthesis of Nanoparticles of TiB2, Nanostructured Materials 2 (1993) 139-147.

[196] D.P. DuFaux, R.L. Axelbaum, Nanoscale Unagglomerated Nonoxide Particles from a Sodium Coflow Flame, Combust. Flame 100 (1995) 350-358.

[197] R.L. Axelbaum, J.I. Huertas, C.R. Lottes, S. Hariprasad, S.M.L. Sastry, Nano-Phase W and W-Ti Composite via Gas-Phase Combustion Synthesis, Materials and Manufacturing Processes 11 (1996) 1043-1053.

[198] K.L. Steffens, M.R. Zachariah, D.P. DuFaux, R.L. Axelbaum, Optical and Modeling Studies of Sodium/Halide Reactions for the Formation of Titanium and Boron Nanoparticles, Chem. Mater. 8 (1996) 1871-1880.

[199] R.L. Axelbaum, D.P. DuFaux, C.A. Frey, S.M.L. Sastry, A Flame Process for Synthesis of Unagglomerated, Low-Oxygen Nanoparticles: Application to Ti and TiB2, Metallurgical and Materials Transactions B 28B (1997) 1199-1211.

[200] J.I. Huertas, Sodium/Halide Flame Synthesis of W and W-Ti Nanoparticles, Dissertation (1997).

[201] R.L. Axelbaum, Synthesis of stable metal and non-oxide ceramic nanoparticles in sodium/halide flames, Powder Metallurgy 43 (2000) 323-325.

[202] R.L. Axelbaum, B.M. Kumfer, Z. Sun, B.H. Chao, Gas-Phase Combustion Synthesis of Nonoxide Nanoparticles in Microgravity, NASA Report CP-2001-210826 (2001).

[203] J.L. Barr, Consolidation and Analysis of Salt-Encapsulated Nanoparticles, Thesis (2001).

[204] D.Y. Maeng, C.K. Rhee, K.H. Kim, W.W. Kim, Synthesis and characterization of nanosize titanium particles by gas-phase combustion, Materials Science and Engineering A 375-377 (2004) 609-614.

[205] J.L. Barr, R.L. Axelbaum, M.E. Macias, Processing salt-encapsulated tantalum nanoparticles for high purity ultra-high surface area applications, Journal of Nanoparticle Research 8 (2006) 11-22.

[206] J.A. Nuetzel, C.J. Unrau, R. Indeck, R.L. Axelbaum, Flame synthesis of superparamagnetic Fe/Nb nanocomposites for biomedical applications, Proc. Comb. Inst. 32 (2009) 1871-1877.

[207] S. Gordon, B.J. McBride, Computer Program for Calculation of Complex Chemical Equilibrium Compositions and Applications, NASA Reference Publication 1311 (1996).

[208] Bell J. H., Metha R. D. Contraction Design for Small Low-Speed Wind Tunnels. NASA-CR-182747, 1988.

[209] S. Mauro, S. Brusca, R. Lanzafame, F. Famoso, A. Galvagno, M. Messina, Small-Scale Open-Circuit Wind Tunnel: Design Criteria, Construction and Calibration, International Journal of Applied Engineering Research 12 (2017) 13649-13662.

[210] J. Xiao, N. Prud'homme, N. Li, V. Ji, Influence of humidity on high temperature oxidation of Inconel 600alloy: Oxide layers and residual stress study, Applied Surface Science 284 (2013) 446-452.

[211] T.M. Copeland-Johnson, C.K.A. Nyamekye, L. Ecker, N. Bowler, E.A. Smith, R.B. Rebak, S.K. Gill, Analysis of Inconel 600 oxidized under loss-of-coolant accident conditions: A multi-modal approach, Corrosion Science 195 (2022) 109950.

[212] T. Butburee, P. Kotchasarn, P. Hirunsit, Z. Sun, Q. Tang, P. Khemthong, W. Sangkhun, W. Thongsuwan, P. Kumnorkaew, H. Wang, K. Faungnawakij, New understanding of crystal control and facet selectivity of titanium dioxide ruling photocatalytic performance, J. Mater. Chem. A 7 (2019) 8156-8166.

Appendix A: Two-color ratio pyrometry MATLAB code

This appendix outlines the MATLAB code used to calculate the soot temperature and volume fraction in Chapters 2 and 3. All images are taken using the Nikon D610 camera and the BG62 filter. The camera is placed such that it is level and the front of the silver bracket on top of the camera is 17.25” from the flame centerline. An image of a ruler at the flame centerline is always taken before a flame is ignited so the resolution and flame height can be measured. All images are taken in RAW mode and converted using dcraw with the following settings: -v -o 0 -q 3 -4 -T ImgXXXX.NEF. Using ImageJ, the R, G, and B signals and the X and Y coordinates are then extracted and saved in a .csv file, which is uploaded into MATLAB. The MATLAB processing is outlined below:

Uploaded variables:

```
R % Raw R signal in a column vector
G % Raw G signal in a column vector
B % Raw B signal in a column vector
X % Raw X coordinates in pixels in a column vector
Y % Raw Y coordinates in pixels in a column vector
```

Initial inputs:

```
res = ; % image resolution in mm/pixel
Y20 = ; % Y pixel that is 20 mm above the burner (measured using ruler image)
```

Identify number of rows and columns (cols) in the image matrix:

```
numY = unique(Y);
rows = length(numY);
cols = size(reshape(X,rows,[]),2);
```

Transform to rows x cols matrices:

```
Xm = zeros(rows,cols);
Ym = zeros(rows,cols);
Rm = zeros(rows,cols);
Gm = zeros(rows,cols);
Bm = zeros(rows,cols);
Xpix = X(1);

r = 1;
for i=1:rows
    for j=1:cols
        Xm(i,j)=X(r);
```

```
        Ym(i,j)=Y(r);
        Rm(i,j)=R2(r);
        Gm(i,j)=G2(r);
        Bm(i,j)=B2(r);
        r=r+1;
        Xm(i,j) = (Xm(i,j)-Xpix)*res;
        Ym(i,j) = ((Y20-Ym(i,j))*res)+20;
    end
end
```

2x2 bin matrices:

```
rows2 = 0;
cols2 = 0;
rows2 = floor(rows/2);
cols2 = floor(cols/2);
Xm2 = zeros(rows2,cols2);
Ym2 = zeros(rows2,cols2);
Rm2 = zeros(rows2,cols2);
Gm2 = zeros(rows2,cols2);
Bm2 = zeros(rows2,cols2);

for i=1:rows2
    for j=1:cols2
        Rm2(i,j) = 0.25*(Rm(2*i-1,2*j-1)+Rm(2*i,2*j)+Rm(2*i-1,2*j)+Rm(2*i,2*j-1));
        Gm2(i,j) = 0.25*(Gm(2*i-1,2*j-1)+Gm(2*i,2*j)+Gm(2*i-1,2*j)+Gm(2*i,2*j-1));
        Bm2(i,j) = 0.25*(Bm(2*i-1,2*j-1)+Bm(2*i,2*j)+Bm(2*i-1,2*j)+Bm(2*i,2*j-1));
        Ym2(i,j) = 0.25*(Ym(2*i-1,2*j-1)+Ym(2*i,2*j)+Ym(2*i-1,2*j)+Ym(2*i,2*j-1));
        Xm2(i,j) = 0.25*(Xm(2*i-1,2*j-1)+Xm(2*i,2*j)+Xm(2*i-1,2*j)+Xm(2*i,2*j-1));
    end
end
```

Smooth image using an Nr x Nc kernel [G. Reeves, smooth2a, Caltech (2009)]:

```
Nr= ; %input rows of kernel
Nc= ; %input cols of kernel

Rs1 = zeros(rows2,cols2);
Gs1 = zeros(rows2,cols2);
Bs1 = zeros(rows2,cols2);

Rs1 = smooth2a(Rm2,Nr,Nc);
Gs1 = smooth2a(Gm2,Nr,Nc);
Bs1 = smooth2a(Bm2,Nr,Nc);

function matrixOut = smooth2a(matrixIn,Nr,Nc)

if nargin < 2, error('Not enough input arguments!'), end

N(1) = Nr;
if nargin < 3, N(2) = N(1); else N(2) = Nc; end

if length(N(1)) ~= 1, error('Nr must be a scalar!'), end
if length(N(2)) ~= 1, error('Nc must be a scalar!'), end
```

```
[row,col] = size(matrixIn);
eL = spdiags(ones(row,2*N(1)+1),(-N(1):N(1)),row,row);
eR = spdiags(ones(col,2*N(2)+1),(-N(2):N(2)),col,col);
A = isnan(matrixIn);
matrixIn(A) = 0;
nrmlize = eL*(~A)*eR;
nrmlize(A) = NaN;
matrixOut = eL*matrixIn*eR;
matrixOut = matrixOut./nrmlize;
```

Radially smooth data before Abel inversion using Savitsky-Golay:

```
Rs = zeros(rows2,cols2);
Gs = zeros(rows2,cols2);
Bs = zeros(rows2,cols2);

order = ; %input order
framelen = ; %input framelen

for i=1:rows2
    Rs(i,:) = sgolayfilt(Rs1(i,:),order,framelen);
    Gs(i,:) = sgolayfilt(Gs1(i,:),order,framelen);
    Bs(i,:) = sgolayfilt(Bs1(i,:),order,framelen);
end
```

Filter any negative values:

```
for i=1:rows2
    for j=1:cols2
        if Rs(i,j) < 0
            Rs(i,j) = 0;
            Gs(i,j) = 0;
            Bs(i,j) = 0;
        end
        if Gs(i,j) < 0
            Rs(i,j) = 0;
            Gs(i,j) = 0;
            Bs(i,j) = 0;
        end
        if Bs(i,j) < 0
            Rs(i,j) = 0;
            Gs(i,j) = 0;
            Bs(i,j) = 0;
        end
    end
end
```

Find flame centerline using G pixel:

```
Gsmax = max(Gs,[],'all');
MAXR = zeros(1,rows2);
MAXL = zeros(1,rows2);
Cent = zeros(1,rows2);
Growmax = max(Gs,[],2);
```

```
for i=1:rows2
    go = true;
    l=0;
    while go
        l=l+1;
        if Growmax(i,1) > 0.1*Gsmax
            if Gs(i,l) >= 0.5*Growmax(i,1)
                go = false;
            end
        end
        if l == cols2
            go = false;
        end
    end
    MAXL(1,i) = l;
end

for i=1:rows2
    go = true;
    r=cols2+1;
    while go
        r=r-1;
        if Growmax(i,1) > 0.1*Gsmax
            if Gs(i,r) >= 0.5*Growmax(i,1)
                go = false;
            end
        end
        if r == 1
            go = false;
        end
    end
    MAXR(1,i) = r;
end

for i=1:rows2
    if (MAXR(i) > 1) && (MAXL(i) < cols2)
        Cent(1,i) = 0.5*(MAXR(1,i)+MAXL(1,i));
        Cent(1,i) = round(Cent(1,i));
    end
end

pos = 1;
val = 0;
for i=1:rows2
    if Cent(1,i) > 0
        pos = i+5;
        val = Cent(1,pos);
        break
    end
end

for i=1:pos
    Cent(1,i) = val;
end
```

```
pos = 1;
val = 0;
for i=1:rows2
    if Cent(1,i) == 0
        pos = i-25;
        val = Cent(1,pos);
        break
    end
end

for i=pos:rows2
    if pos ~= 1
        Cent(1,i) = val;
    end
end
```

Make matrices for deconvolution:

```
r = 1;
for i=1:cols2
    X_len(1,r) = (i-1)*2*res;
    if X_len(1,r) > 7
        break
    end
    r = r+1;
end
r = r-1;
XR = zeros(rows2,r);
YR = zeros(rows2,r);
R_R = zeros(rows2,r);
G_R = zeros(rows2,r);
B_R = zeros(rows2,r);
R_L = zeros(rows2,r);
G_L = zeros(rows2,r);
B_L = zeros(rows2,r);
for i=1:rows2
    for j=1:r
        if Cent(1,i) > 0
            if j < cols2-Cent(1,i)
                R_R(i,j) = Rs(i,Cent(1,i)+j-1);
                G_R(i,j) = Gs(i,Cent(1,i)+j-1);
                B_R(i,j) = Bs(i,Cent(1,i)+j-1);
            end
        end
        if Cent(1,i) > 0
            if j < cols2-Cent(1,i)
                R_L(i,j) = Rs(i,Cent(1,i)-j+1);
                G_L(i,j) = Gs(i,Cent(1,i)-j+1);
                B_L(i,j) = Bs(i,Cent(1,i)-j+1);
            end
        end
        R_R(i,j) = 0.5*(R_R(i,j)+R_L(i,j));
        G_R(i,j) = 0.5*(G_R(i,j)+G_L(i,j));
```

```
        B_R(i,j) = 0.5*(B_R(i,j)+B_L(i,j));
        XR(i,j) = (j-1)*2*res;
        YR(i,j) = Ym2(i,j);
    end
end
```

Deconvolution using Abel inversion:

```
L=r;
res2 = 0.5;

Rab = zeros(rows2,L);
for w=1:rows2
    py = zeros(1,L);
    for v=1:L
        py(v) = R_R(w,v);
    end

    fft=zeros(L);
    for i=1:L
        for j=i:L-1
            fft(i,j)=-1/pi()*2*(py(j+1)-py(j))/(((j+1-1)*res2)^2-((j-1)*res2)^2)*...
                (sqrt(((j+1-1)*res2)^2-((i-1)*res2)^2)-sqrt(((j-1)*res2)^2-((i-
1)*res2)^2));
        end
    end

    aby=sum(fft,2);

    for v=1:L
        Rab(w,v) = aby(v);
    end

end

Gab = zeros(rows2,L);
for w=1:rows2
    py = zeros(1,L);
    for v=1:L
        py(v) = G_R(w,v);
    end

    fft=zeros(L);
    for i=1:L
        for j=i:L-1
            fft(i,j)=-1/pi()*2*(py(j+1)-py(j))/(((j+1-1)*res2)^2-((j-1)*res2)^2)*...
                (sqrt(((j+1-1)*res2)^2-((i-1)*res2)^2)-sqrt(((j-1)*res2)^2-((i-
1)*res2)^2));
        end
    end

    aby=sum(fft,2);

    for v=1:L
```

```
        Gab(w,v) = aby(v);
    end

end

Bab = zeros(rows2,L);
for w=1:rows2
    py = zeros(1,L);
    for v=1:L
        py(v) = B_R(w,v);
    end

    fft=zeros(L);
    for i=1:L
        for j=i:L-1
            fft(i,j)=-1/pi()*2*(py(j+1)-py(j))/(((j+1-1)*res2)^2-((j-1)*res2)^2)*...
                (sqrt(((j+1-1)*res2)^2-((i-1)*res2)^2)-sqrt(((j-1)*res2)^2-((i-
1)*res2)^2));
        end
    end

    aby=sum(fft,2);

    for v=1:L
        Bab(w,v) = aby(v);
    end

end
```

Calculate signal ratios and soot temperature using curve fits from lookup table:

```
Gabmax = max(Bab,[],'all');
Rsab = Rab;
Gsab = Gab;
Bsab = Bab;

BGr = zeros(rows2,L);
BRr = zeros(rows2,L);
GRr = zeros(rows2,L);
TBG = zeros(rows2,L);
TBR = zeros(rows2,L);
TGR = zeros(rows2,L);

for i=1:rows2
    for j=1:L
        if Bsab(i,j) > 0
            if Gsab(i,j) > 0
                BGr(i,j)=Bsab(i,j)/Gsab(i,j);
            else
                BGr(i,j)=0;
            end
        else
            BGr(i,j)=0;
        end
```

```
        if Bsab(i,j) > 0
            if Rsab(i,j) > 0
                BRr(i,j)=Bsab(i,j)/Rsab(i,j);
            else
                BRr(i,j)=0;
            end
        else
            BRr(i,j)=0;
        end
        if Gsab(i,j) > 0
            if Rsab(i,j) > 0
                GRr(i,j)=Gsab(i,j)/Rsab(i,j);
            else
                GRr(i,j)=0;
            end
        else
            GRr(i,j)=0;
        end

        if Gsab(i,j) < 0.05*Gabmax
            GRr(i,j) = 0;
            BRr(i,j) = 0;
            BGr(i,j) = 0;
        end

        if (BGr(i,j) >= 0.133357576) && (BGr(i,j) <= 0.487344024) %BG1 1000-1999
            TBG(i,j) = 797.83+2704*(BGr(i,j))-985.7*(BGr(i,j)^2)+1359*(BGr(i,j)^3)-
(19.39/BGr(i,j))+(0.02276/(BGr(i,j)^2));
        end
        if (BGr(i,j) > 0.487344024) && (BGr(i,j) <= 0.798589617) %BG2 2000-3000
            TBG(i,j) = -2669.75+9002*(BGr(i,j))-
6736*(BGr(i,j)^2)+3469*(BGr(i,j)^3)+(940/BGr(i,j))-(106.6/(BGr(i,j)^2));
        end
        if (BGr(i,j) < 0.133357576) || (BGr(i,j) > 0.798589617)
            TBG(i,j) = 300;
        end

        if (BRr(i,j) >= 0.053988756) && (BRr(i,j) <= 0.550112335) %BR1 1000-1999
            TBR(i,j) = 1097.8+2256*(BRr(i,j))-1569*(BRr(i,j)^2)+982.7*(BRr(i,j)^3)-
(16.24/BRr(i,j))+(0.2503/(BRr(i,j)^2));
        end
        if (BRr(i,j) > 0.550112335) && (BRr(i,j) <= 1.225575244) %BR2 2000-3000
            TBR(i,j) = 965.95+1969*(BRr(i,j))-
641.9*(BRr(i,j)^2)+286.5*(BRr(i,j)^3)+(85.52/BRr(i,j))-(17.91/(BRr(i,j)^2));
        end
        if (BRr(i,j) < 0.053988756) || (BRr(i,j) > 1.225575244)
            TBR(i,j) = 300;
        end

        if (GRr(i,j) >= 0.404856493) && (GRr(i,j) <= 1.128836951) %GR1 1000-1999
            TGR(i,j) = -520.5+3134*(GRr(i,j))-
1844*(GRr(i,j)^2)+763.8*(GRr(i,j)^3)+(295.7/GRr(i,j))-(37.23/(GRr(i,j)^2));
        end
        if (GRr(i,j) > 1.128836951) && (GRr(i,j) <= 1.372647305) %GR2 2000-2499
```

```
            TGR(i,j) = 2116*(GRr(i,j)^3)-6366*(GRr(i,j)^2)+8013*(GRr(i,j))-1978.1;
        end
        if (GRr(i,j) > 1.372647305) && (GRr(i,j) <= 1.534729353) %GR3 2500-3000
            TGR(i,j) = 8236*(GRr(i,j)^3)-31790*(GRr(i,j)^2)+43260*(GRr(i,j))-18285.4;
        end
        if (GRr(i,j) > 1.534729353) || (GRr(i,j) < 0.404856493)
            TGR(i,j) = 300;
        end
    end
end
```

Calculate average soot temperature at each pixel:

```
Ttot = zeros(rows2,L);

for i=1:rows2
    for j=1:L
        if (TBG(i,j) > 1000) && (TBR(i,j) > 1000) && (TGR(i,j) > 1000)
            Ttot(i,j) = (TBG(i,j)+TBR(i,j)+TGR(i,j))/3;
        else
            Ttot(i,j) = 300;
        end
    end
end
```

Calculate soot volume fraction:

```
lamG = 525E-9; %Effective wavelength
n_G = 1.811+0.1263*log(lamG*1E6)+0.027*(log(lamG*1E6)^2)+0.0417*(log(lamG*1E6)^3); %G
real index
k_G = 0.5821+0.1213*log(lamG*1E6)+0.2309*(log(lamG*1E6)^2)-0.01*(log(lamG*1E6)^3); %G
imaginary index
Em_G = 6*((n_G*k_G)/((((n_G^2)-(k_G^2)+2)^2)+(4*(n_G^2)*(k_G^2))));
labsG = lamG/(6*pi()*Em_G); %G natural length for absorption [m]

Tbb =; %Temperature of black body calibration source in K
taubb =; %Exposure time of black body calibration source
tauf =; %Exposure time of flame image
SbbG =; %Signal of black body calibration source for G

fv = zeros(rows2,L); % soot volume fraction in m3/m3
Fv = zeros(rows2,L); %soot volume fraction in ppm
fv_log = zeros(rows2,L);
Tlim = 1000;

for a=1:rows2
    for b=1:L
        if (Ttot(a,b) == 300)
            fv(a,b) = 0;
        end
        if (Ttot(a,b) <= Tlim) && (Ttot(a,b) > 300)
            fv(a,b) = fv(a,b-1);
        end
        if (Ttot(a,b) >= Tlim)
```

```
            if (Ttot(a,b) >= 1000) && (Ttot(a,b) <= 3000)
                fv_log(a,b) = 1-epsbb*(tauf/taubb)*(Gsab(a,b)/SbbG)*exp(((-
h*c)/(k*lamG))*((1/Tbb)-(1/Ttot(a,b))));
                fv(a,b) = (-labsG/(Lab))*log(fv_log(a,b));
            end
        end
        Fv(a,b) = fv(a,b)*1000000;
    end
end
```

Mirror half flame to whole flame matrices:

```
F = 2*L-1;

Xf = zeros(rows2,F);
Yf = zeros(rows2,F);
RT = zeros(rows2,F);
GT = zeros(rows2,F);
BT = zeros(rows2,F);
Fvf = zeros(rows2,F);
Ttotf = zeros(rows2,F);

for t=1:rows2
    q = 1;
    for i=1:F
        if i < L
            Xf(t,i) = -1*XR(t,(L-i+1));
            Yf(t,i) = YR(t,(L-i+1));
            RT(t,i) = Rab(t,(L-i+1));
            GT(t,i) = Gab(t,(L-i+1));
            BT(t,i) = Bab(t,(L-i+1));
            Fvf(t,i) = Fv(t,(L-i+1));
            Ttotf(t,i) = Ttot(t,(L-i+1));
        end
        if i >= L
            Xf(t,i) = XR(t,q);
            Yf(t,i) = YR(t,q);
            RT(t,i) = Rab(t,q);
            GT(t,i) = Gab(t,q);
            BT(t,i) = Bab(t,q);
            Fvf(t,i) = Fv(t,q);
            Ttotf(t,i) = Ttot(t,q);
            q = q + 1;
        end
    end
end
```

Plot temperature and log plot soot volume fraction:

```
ax = 18; %axes label font size
leg = 18; %axes number font size
fs = 20;
ti = 20; %title font size
y_ax = 45;
```

```
f1 = figure;
figure(f1);
[M,d] = contourf(Xf,Yf,Fvf,2500);
set(gca,'FontSize',leg);
xlabel('r [mm]','fontsize',ax);
ylabel('z [mm]','fontsize',ax);
%title({''},'fontsize',ti);
ylim([0 y_ax]);
map = jet(256);
for i=1:1
    map(i,:) = [1,1,1];
end
colormap(map);
colorbar('FontSize',fs);
c = colorbar;
c.Label.String = 'Soot Volume Fraction [ppm]';
c.Label.FontSize = fs;
caxis ('manual');
caxis ([0.001 50]);
daspect([1 1 1]);
set(gca,'ColorScale','log');
set(d,'LineColor','none');

f2 = figure;
figure(f2);
[W,u] = contourf(Xf,Yf,Ttotf,1000);
set(gca,'FontSize',leg);
xlabel('r [mm]','fontsize',ax);
ylabel('z [mm]','fontsize',ax);
%title({''},'fontsize',ti);
ylim([0 y_ax]);
map = jet(256);
map(1,:) = [1,1,1];
colormap(map);
colorbar('FontSize',fs);
c = colorbar;
c.Label.String = 'Soot Temperature [K]';
c.Label.FontSize = fs;
caxis ('manual');
caxis ([1400 2400]);
daspect([1 1 1]);
set(u,'LineColor','none');
```

Appendix B: Images of experimental setup aboard the ISS and Flame Design images/videos

B.1 Images of the ACME chamber and experimental setup

Below are images of the experimental setup for Flame Design, including images of the ACME chamber aboard the ISS and experimental equipment. All images are generously provided by NASA.

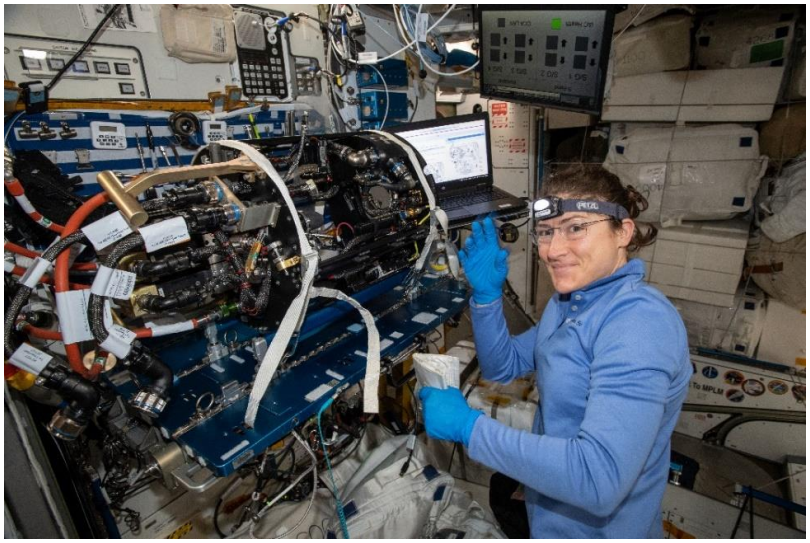

Fig. B.1. Astronaut Christina Koch installing the porous spherical burner into the ACME chamber insert aboard the ISS.

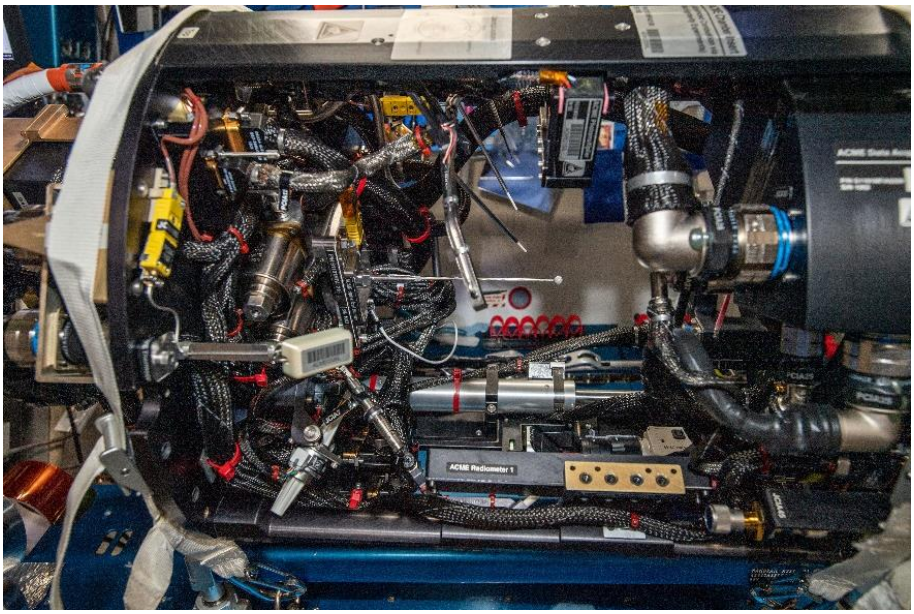

Fig. B.2. Inside of the ACME chamber insert with the porous spherical burner installed.

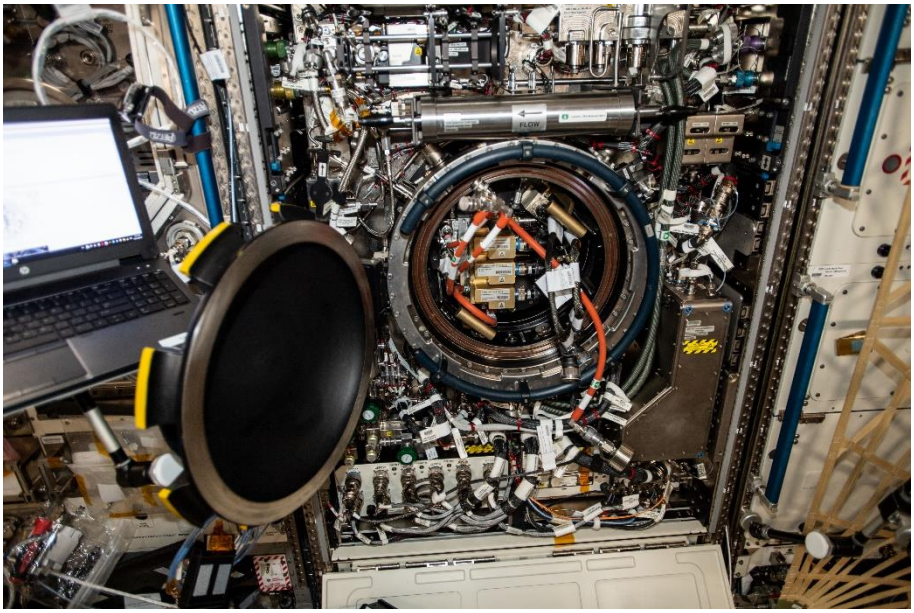

Fig. B.3. The ACME chamber insert installed in the Combustion Integrated Rack (CIR) on the ISS.

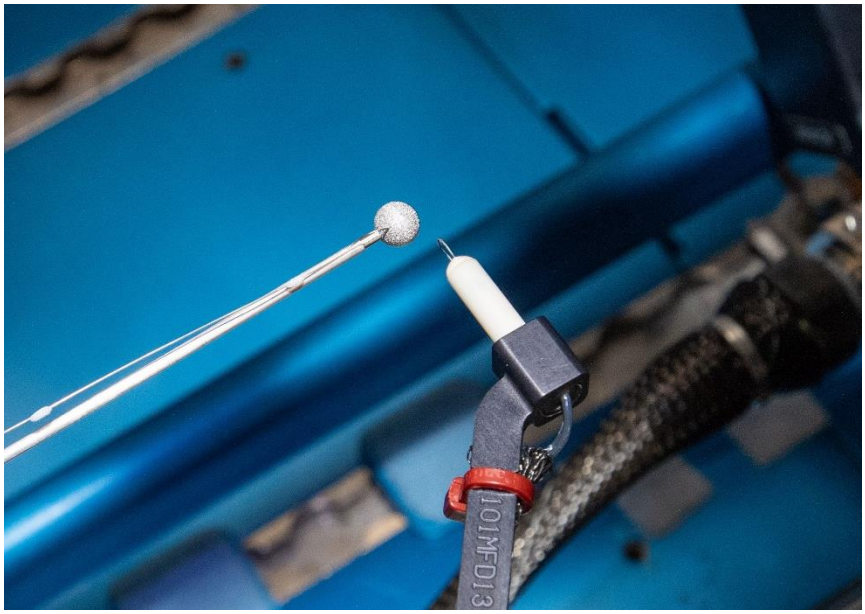

Fig. B.4. The porous spherical burner with the hot wire retractable igniter in place.

Fig. B.5. Closeup of the porous spherical burner and burner surface thermocouple prior to launch to the ISS.

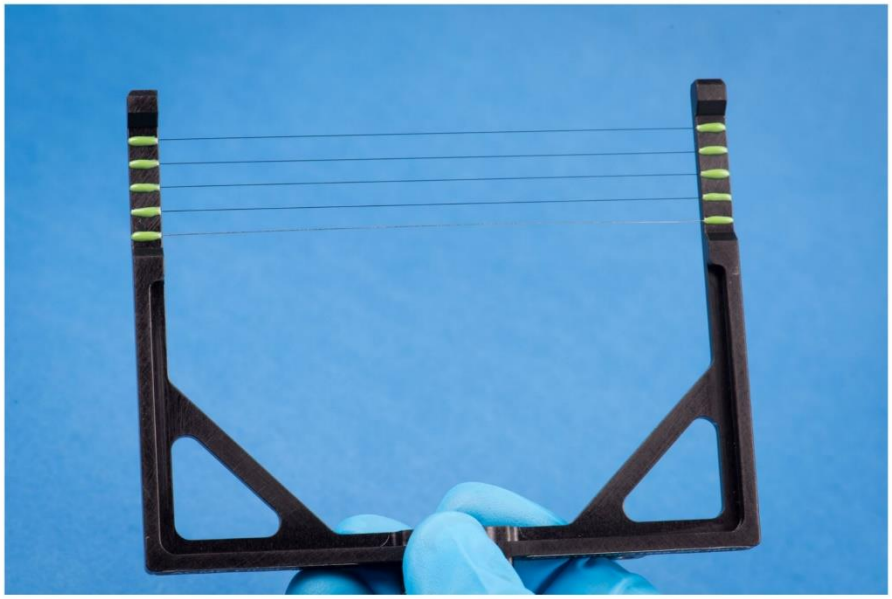

Fig. B.6. Closeup of the thin-filament fiber arm prior to launch to the ISS.

B.2 Images/videos from Flame Design

Below are some images and videos taken during the Flame Design experimental campaign. All videos were compiled and edited by Logan Tan.

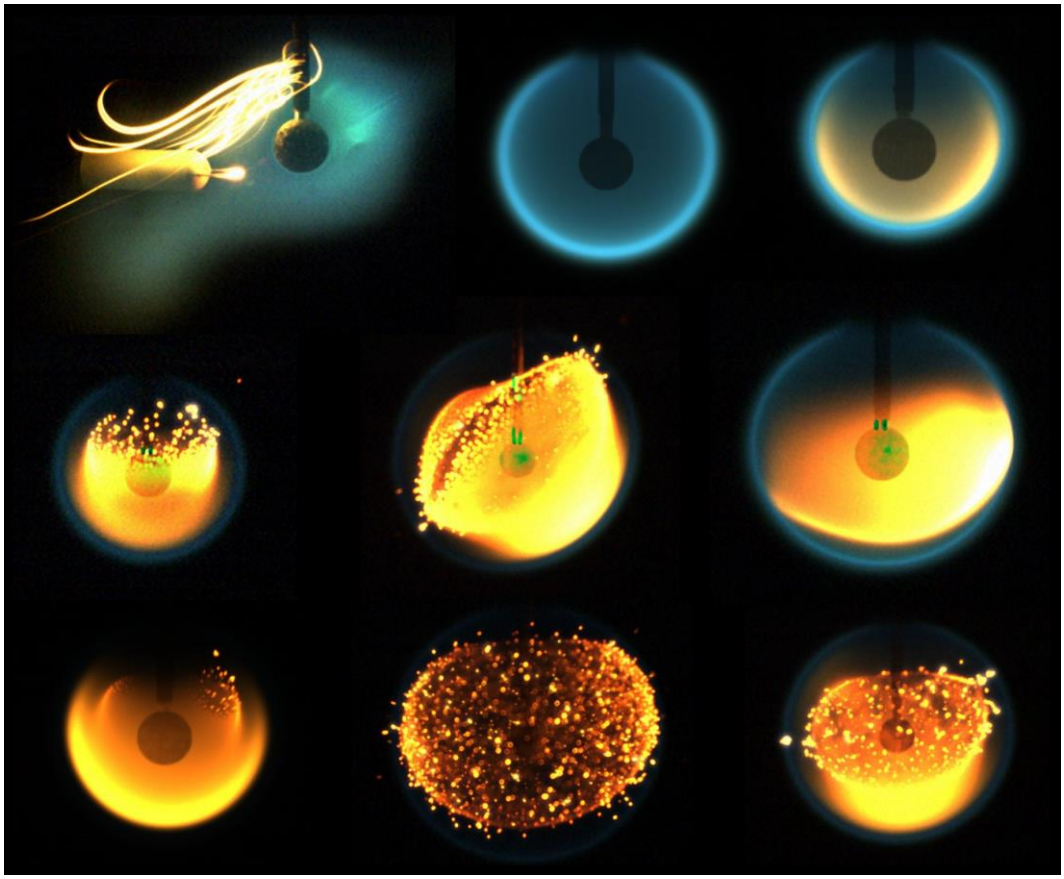

Fig. B.7. Normal flame images taken during Flame Design.

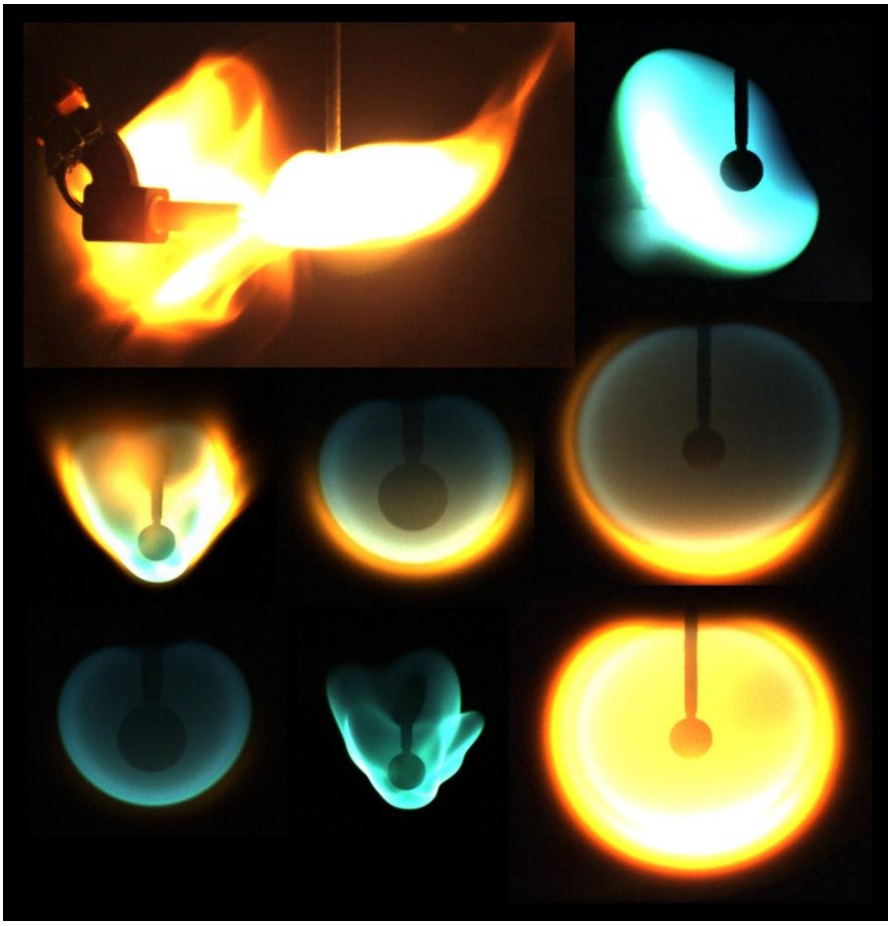

Fig. B.8. Inverse flame images taken during Flame Design.

Table B.1
Interesting Flame Design videos.

Normal flames
19150G2
19156C3
19171D1
19196D1
19200A7
Inverse flames
21349M3
21349M6
21349N3
21361M3

Appendix C: FLAMe reactor images

Below are images of the FLAMe reactor including the burner, nozzle, and vacuum chamber, as described in Chapter 8.

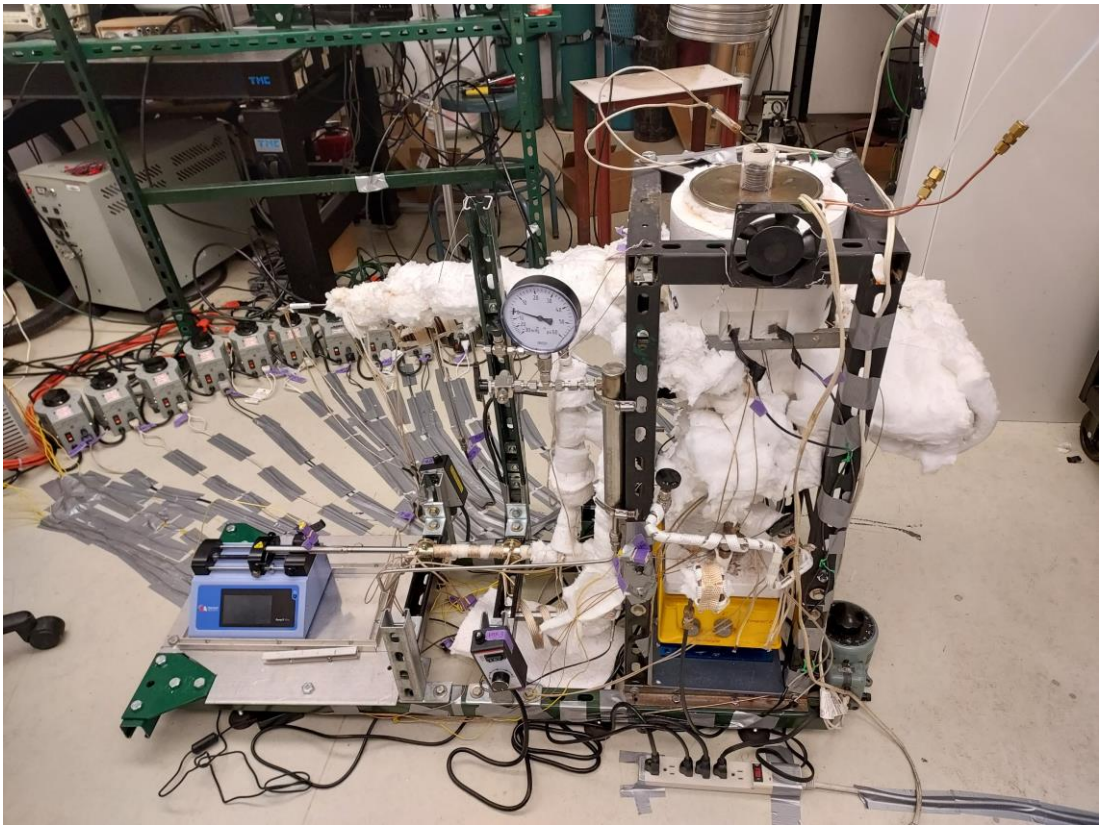

Fig. C.1. Front view of the FLAMe reactor without the nozzle and vacuum chamber.

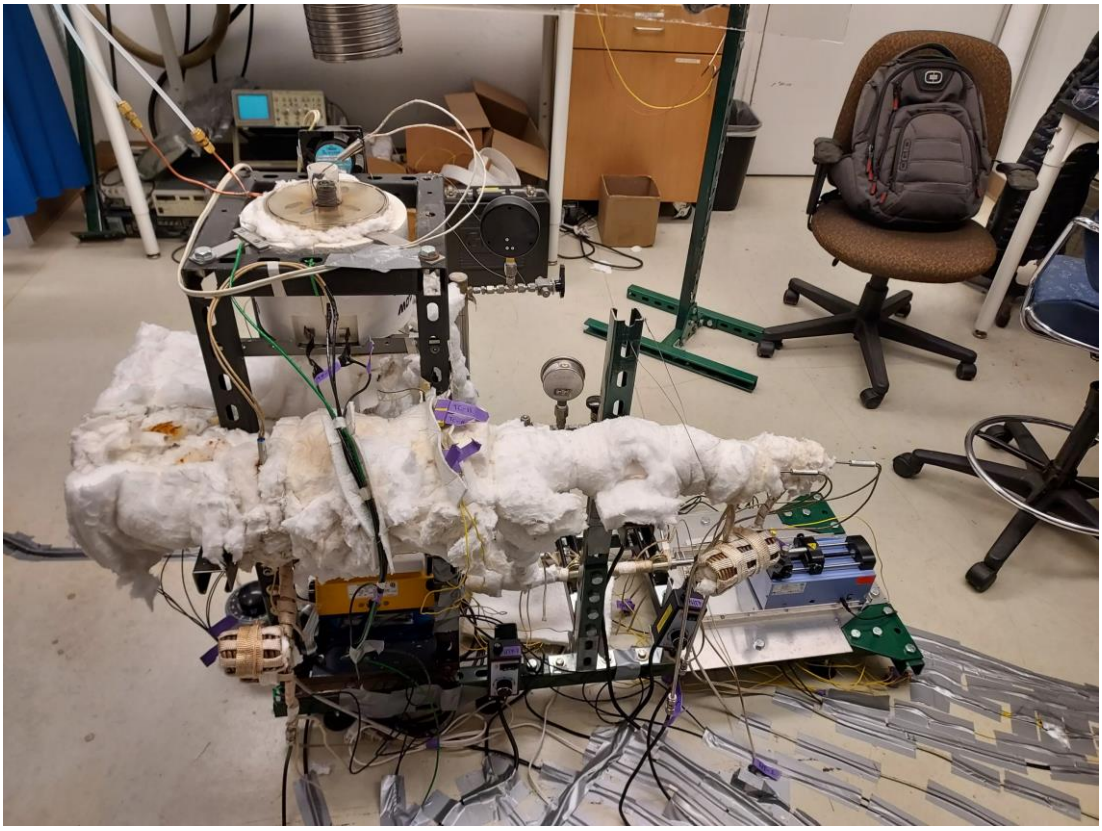

Fig. C.2. Rear view of the FLAMe reactor without the nozzle and vacuum chamber.

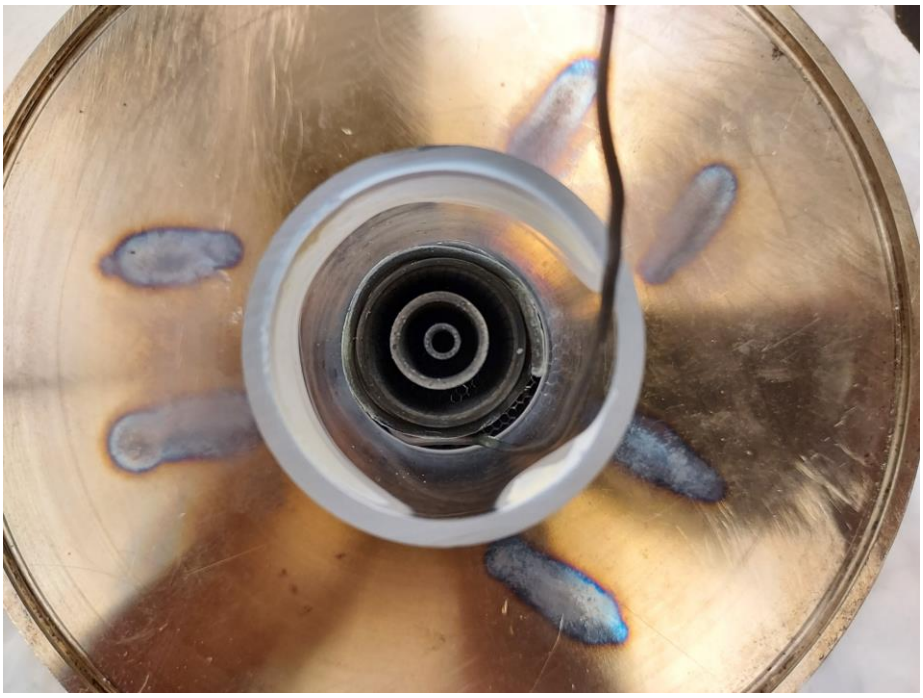

Fig. C.3. Top view of the FLAMe burner without the nozzle and vacuum chamber.

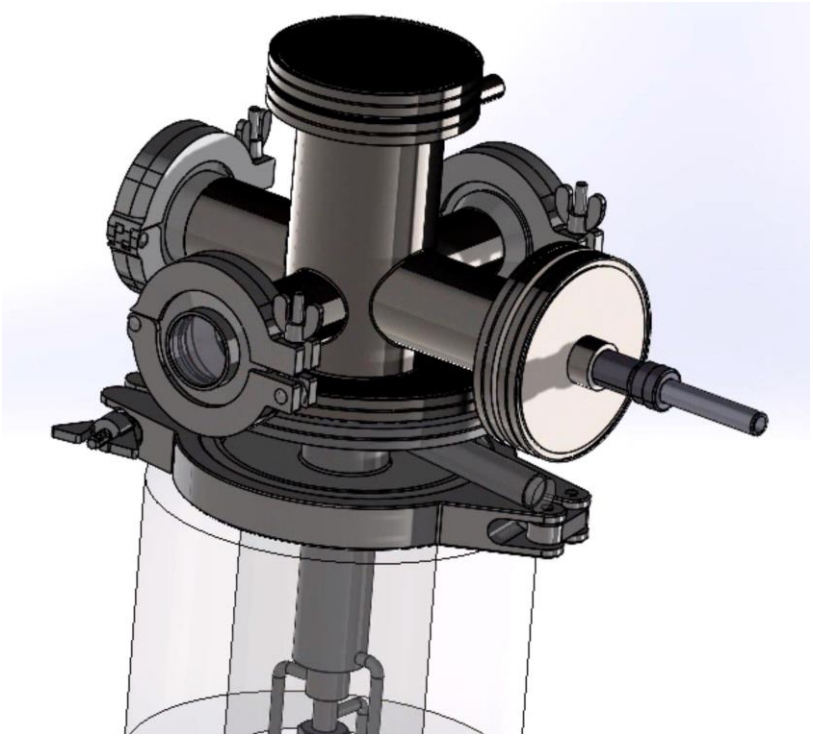

Fig. C.4. 3D model of the FLAMe burner with nozzle section and vacuum chamber.

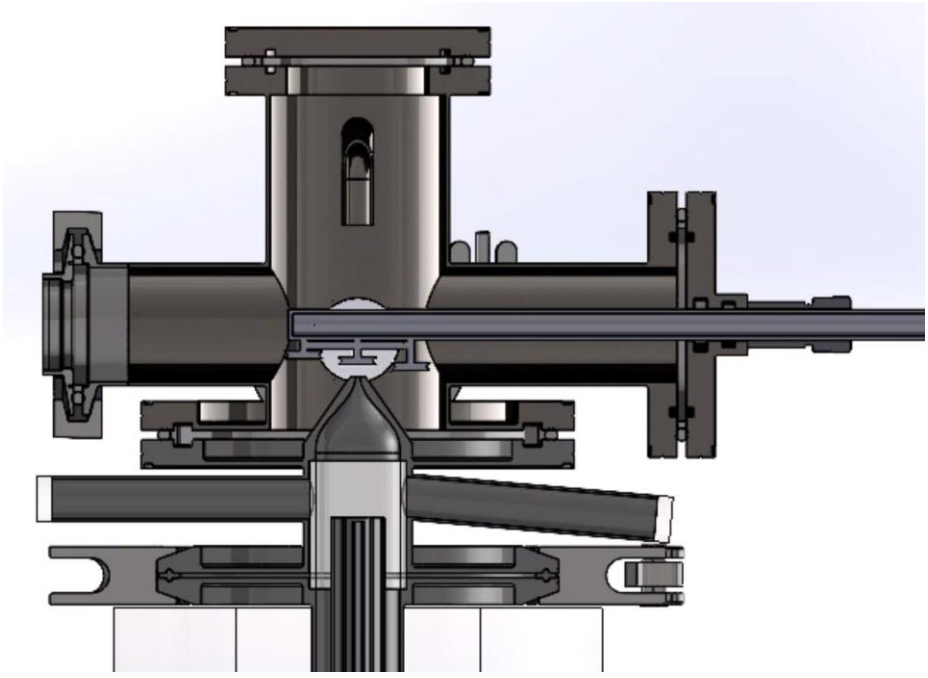

Fig. C.5. 3D model cross section of the FLAMe system with nozzle section and vacuum chamber.

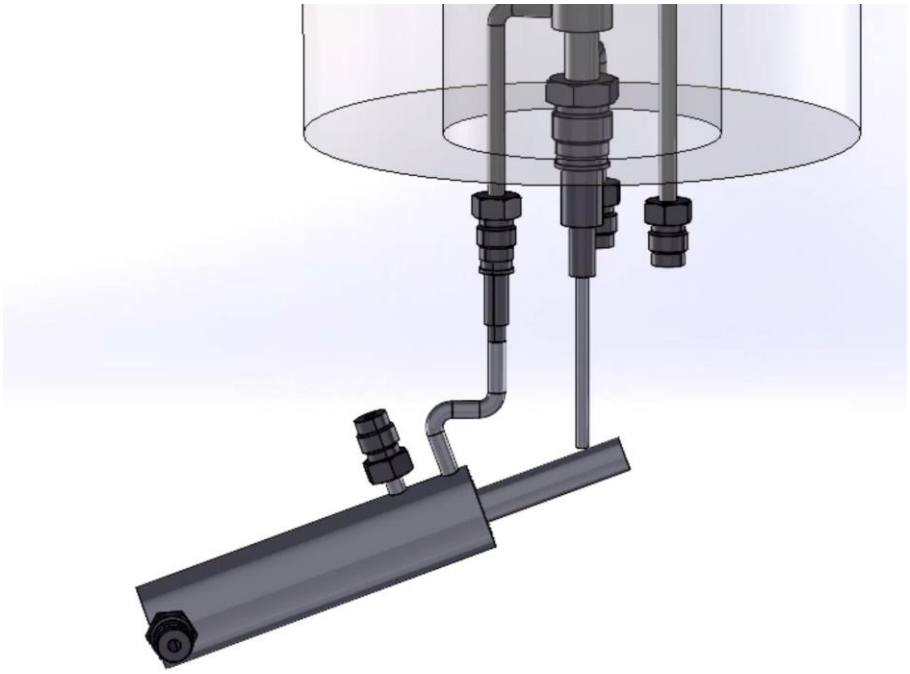

Fig. C.6. 3D model view of the sodium vaporizer.

Fig. C.7. Image of a $TiCl_4$/Na/Ar flame.

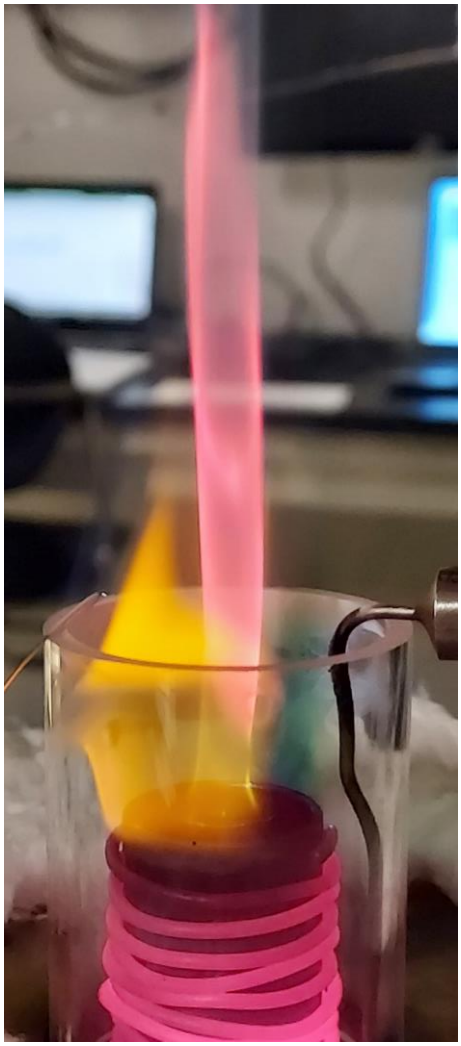

Fig. C.8. Image of a $TiCl_4$/Na/Ar flame.